Acoustic and flow measurements of porous plate designs for aerodynamic noise mitigation

by

John R. Kershner

A Dissertation
Presented to the Graduate and Research Committee
of Lehigh University
in Candidacy for the Degree of
Doctor of Philosophy
in
Mechanical Engineering

Lehigh University
August 2024

Approved and recommended for acceptance as a dissertation in partial fulfillment of the requirements for the degree of Doctor of Philosophy.

John R. Kershner

Acoustic and flow measurements of porous plate designs for aerodynamic noise mitigation

Defense Date

Dissertation Director

Approved Date

Committee Members:

Arindam Banerjee, Committee Chair

Hannah Dailey

Alparslan Oztekin

Michael Krane

Justin W. Jaworski

Acknowledgments

Thank you first and foremost to my advisor Professor Justin Jaworski for your excellent mentorship and support during my Ph.D. I am very grateful for our many insightful conversations through which you shared your great knowledge of acoustics with me. I am also exceptionally grateful for your support and connections with national and international researchers which have allowed me to see many parts of the world during my studies.

I would also like to thank Dr. Thomas Geyer at The German Aerospace Center and the Brandenburg University of Technology. Thank you for sharing your facilities and being an excellent mentor during and after my Fulbright year. Thanks for always being at the ready to answer my questions at any time of the day due to the time difference, and I will fondly remember our time spent at many conferences across the world.

I also thank Dr. Michael Krane of the Applied Research Laboratory at Penn State University. Your mentorship, especially during the early years of my Ph.D., was incredibly important for developing my experimental research skills.

In addition, the remote-controlled glider work would not have been completed were it not for the great effort of STEM-SI students Michael Dominguez, Emily Schmidt, Sai Meh, Ryan Burke, and Rafa Bermudez.

This work was supported by NSF CAREER award 1846852, the NSF INTERN Program, the German-American Fulbright Program/Germanistic Society of America, Lehigh University's STEM-SI program, and the J. David A Walker and M. Elizabeth Walker Endowed Fellowship at Lehigh University. Thank you also to my other committee members for your continued support.

Special thanks to MJ for always keeping the science car running. Thank you to all my friends, roommates, labmates and extended family for the fun times we spent together during my Ph.D. I considered listing names, but realized this would lead to way too much fighting! Lastly, to my parents and sister, *whooo* would I be without you? Thank you for your support and for always believing in me while I pursued this degree. I truly could not have done it without you.

Table of Contents

List of Tables

List of Figures

Abstract

An experimental study investigates parametrically the effects of porosity on the acoustic and aerodynamic fields about lifting- and non-lifting surfaces at two separate aeroacoustic facilities using microphone arrays and hot-wire anemometry. A single dimensionless porosity parameter characterizes the flow noise generated by a turbulent boundary layer and informs the design of the porous edge test specimens, including perforated flat plates and flat-plate extensions with a blunt or sharp trailing edge.

The strong tonal peak due to vortex shedding from blunt trailing-edges diminishes in magnitude as the porosity parameter increases, and high-porosity plates eliminate this tone from the acoustic spectra. Single-microphone measurements indicate further that the porous plates examined can reduce low-frequency noise and increase high-frequency excess noise levels by up to 10 dB. DAMAS beamforming of the porous plates with sharpened edges reveal similar results on the acoustic spectra and identify that the principal effect of edge porosity on the acoustic source regions is a reduction in low-frequency noise and an increase in high-frequency noise across the entire plate. Noise generated by porous edges in the low-frequency range by the trailing- and leading-edge regions can be reduced by up to 20 dB, and porous edges increase high-frequency noise by up to 20 dB. Plates with the same dimensionless porosity perform similarly, where plates with circular holes perform slightly better (2 dB) than their counterparts with square holes at reducing low-frequency noise the most and increasing high-frequency noise the least in wind tunnel testing.

Hot-wire anemometry of the flow field about blunt porous trailing edges reveals a downward shift of the bluntness-induced vortex-shedding peak in the spectra of turbulent velocity

fluctuations, which are not seen in the acoustic spectra. In addition, flow field measurements for both the blunt-edged and sharp-edge plates indicate significant increases in turbulence intensity at the plate surface which are believed to be caused by the presence of holes and related to the increase in noise seen at high frequencies.

The wing of a remote-controlled glider is modified with porous plates near the trailing edge to demonstrate reductions in surface pressure level fluctuations on a flying vehicle at the owl scale. Measurements of these fluctuations on the wing and fuselage indicate the capacity of porous plates to modestly reduce surface pressure levels in select frequency ranges and settings of aerial vehicles.

Chapter 1

Introduction

1.1 Background and related work

Aerodynamic lifting surfaces possess several routes to self-noise that contribute to their flow-generated acoustic signature. This dissertation focuses on the disruption of flow noise generated at the trailing edge by two established mechanisms: turbulent boundary layer (TBL) trailing-edge (TE) noise due to the interaction broadband disturbances in the boundary layer with the trailing edge [1] and bluntness noise in the form of tonal noise produced by vortex shedding from a blunt TE [2]. These types of flow noise sources contribute to noise pollution in many different aero- and hydrodynamic environments that include, but are not limited to wind turbine blades, engine-fan rotors, submarines, and airplane wings [2–6]. An ever-growing presence of these devices and the potential negative impact on public health due to sound [7] have led to increasingly stringent noise pollution requirements [8]. In order to meet these requirements, scientists and engineers have looked to nature to identify innovative ways to reduce TE noise levels. Among several avian adaptations, many owl species possess the ability to fly in near-silence [9], which could be in part due to their porous wings. This dissertation experimentally investigates the effects of the presence of edge porosity, inspired by quiet owl flight, on the acoustic and flow fields of perforated flat plates, where the porosity is characterized by a single dimensionless parameter. Relevant flow noise generation mechanisms and noise control methods are discussed in this chapter, and unresolved research areas and research goals for this dissertation are outlined.

1.1.1 Flow noise generation mechanisms

There exist five main noise-generating mechanisms on a lifting surface (e.g. a wing, airfoil, or control surface) in a low-turbulence flow at low Mach numbers [2]: turbulent boundary layer trailing-edge noise (interaction of the boundary layer with the trailing edge), separation-stall noise (noise generated by separated flow), laminar boundary layer trailing-edge noise (vortex shedding at the trailing edge due to a laminar boundary layer), tip-vortex formation noise (interaction of the boundary layer with the tip of the surface), and bluntness vortex shedding noise (vortex shedding noise generated by the interaction of the boundary layer with a blunt trailing edge). Figure 1.1 depicts TBL TE noise and bluntness noise, whose mitigation is the focus of this dissertation. Details on these noise sources are now discussed further.

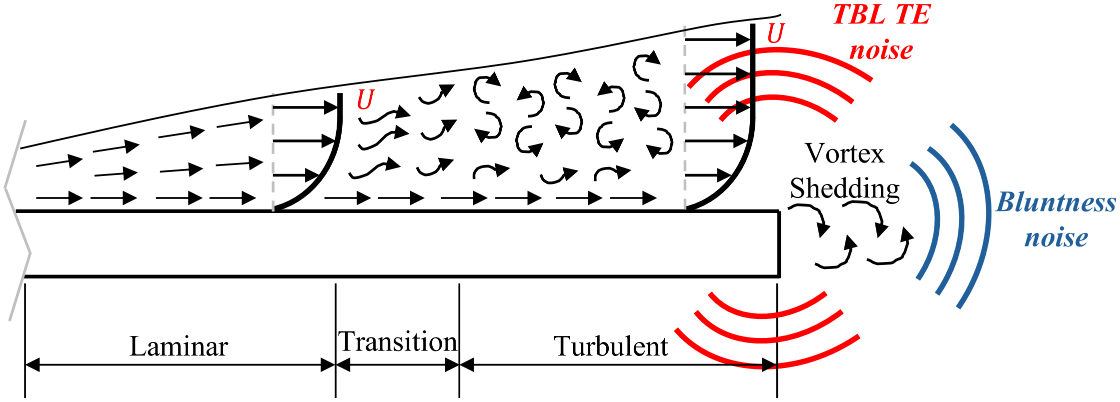

Figure 1.1: Boundary layer growth over a flat place with depictions of turbulent boundary-layer trailing-edge noise and bluntness noise.

Turbulent boundary layer trailing-edge noise is a scattering phenomenon in which the interaction of a high-wavenumber disturbance with an edge results in a propagating acoustic wave [1]. Powell [10] was the first to recognize the ability of an edge to convert turbulent sources into dipole radiators. Later predictive analyses for noise scattered by edges [11] or fully-porous surfaces [12] support the well-known dependence of radiated noise intensity on the freestream velocity as U^5. Several analytical theories on turbulent boundary layer trailing-edge noise were reviewed by Howe [13], who concluded that the models were nearly the same and lead to the same velocity dependence of U^5 [13] and incorporated the effects of the Kutta condition and Doppler amplification into a unified theory of trailing edge noise. The acoustic power scaling of the radiated sound on flow speed, U^γ, varies between $5 \leq \gamma \leq 6$ for porous edges and acoustically non-compact airfoils [12, 14], which is to be compared against the $\gamma = 5$ result for impermeable edges [11]. In Chen et al. [15], a time-domain Green's function approach solves the acoustic scattering problem inspired by Kambe et al. [16] of a vortex ring passing over a semi-infinite porous plate to predict the acoustic power scaling, directivity patterns, and acoustic pressure waveforms. Their theoretical model uses a dimensionless porosity parameter, composed of physical details of the porous/perforated medium and the acoustic field,

$$\delta = \frac{2\alpha_h c}{\pi^2 f R}, \tag{1.1}$$

which was identified by Ffowcs Williams [17] in his analysis of infinite porous surfaces. In (1.1), α_h is the open-area fraction, c is the speed of sound, f is the frequency, and R is the pore radius. Jaworski and Peake [12] extended the seminal analysis of Crighton and Leppington [18] to show that the acoustic scaling of porous edge noise on flight speed becomes U^6 for large values of δ (referred to as μ/k in Jaworski and Peake [12] and Chen et al. [15]), which results in an effective decrease of noise in low-Mach-number flows. The dependence of the velocity scaling exponent γ on the dimensionless porosity parameter δ is shown in figure 1.2. The change in acoustic power scaling is accompanied by a notable change in sound directivity, from a cardioid shape at U^5 to a dipole shape at U^6 [15].

In contrast to TBL TE noise, bluntness noise is tonal in nature and originates from vortex shedding at the TE. This kind of noise is highly dependent on edge geometry and Reynolds number (Re), and it typically occurs typically at

$$\frac{2\pi f z_{\text{wake}}}{U} \simeq 1, \tag{1.2}$$

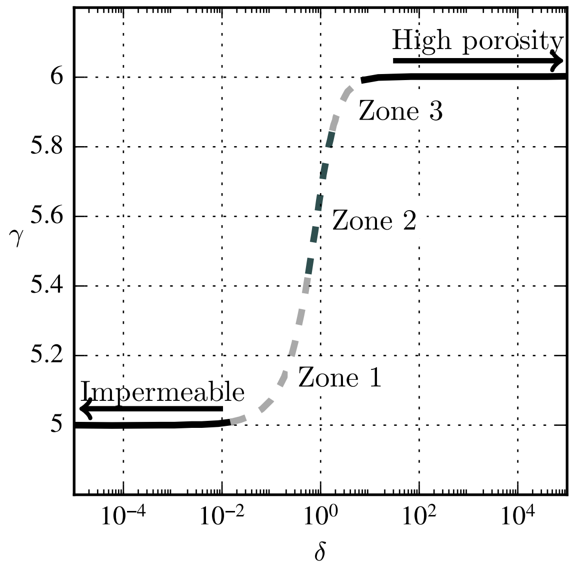

Figure 1.2: Theoretical predictions for the acoustic power scaling on flow speed γ as a function of the dimensionless porosity parameter δ. Adapted with permission from Chen et al. [15].

where z_{wake} is the wake scale, when the ratio of the bluntness thickness (w) to the boundary-layer displacement thickness is $w/\delta^* > 0.3$ (see table 5.3 in [1]). For the case of NACA 0012 airfoils and flat plates, bluntness vortex shedding is prevalent between chord-based Strouhal numbers of $St = 0.12$ and $St = 0.22$ [19, 20].

1.1.2 Porosity as a bio-inspired flow noise control mechanism

Owls are nature's quiet flier. There are many species that are able to suppress flight noise below the human level of hearing in the 1.6 kHz to 10 kHz range [4, 12]. The recent reexamination of quiet owl flight by the aeroacoustics community has led several researchers to explore how material or geometric aspects of avian wings could enable passive aerodynamic noise reduction in low-speed flows [4]. First identified by Graham in 1934, there are three unique features of owl wings believed to enable their quiet flight: a leading-edge (LE) comb, a compliant trailing-edge fringe, and a downy upper-wing surface [21]. The leading-edge comb has been adapted in engineering applications to reduce leading-edge aeroacoustic noise using serrations, and many works have successfully demonstrated the ability of serrations to significantly reduce the turbulence induced leading-edge noise [22–25]. The downy wing surface has also been investigated for its ability to reduce roughness-induced flow noise [26]. Lastly, the adaptations of owl-inspired edges to reduce trailing-edge noise has come in many forms. Among many design approaches, serrations [27–31], TE brushes [32, 33], and finlets [34] have successfully demonstrated TBL TE noise reductions.

The presence of wing porosity is another potential method to reduce turbulence scattering at the trailing edge of wings and other aerodynamic edges. The "compliant" trailing edge of owls was first interpreted as being porous by Kroeger et al. [35] and Neuhaus et al. [36]. During the wing upstroke, the feathers separate allowing air to flow in between [37, 38], and Bachmann et al. [39] compared the morphology of owl wings to pigeon wings and found that the detailed feather structure of owls could help minimize the aerodynamic resistance of the wing during the upstroke phase of flapping flight. In addition, measurements of the air flow resistance of a set of owl wings against the wings of noisier birds confirm the higher permeability of the plumage of owls [40]. Within the aeroacoustics community, Hayden et al. [41] carried out some of the first experimental research on the application of porous treatments to trailing edges using various physical designs to effect acoustic impedance flap treatments. However, in later experiments, observed achievements in the reduction of trailing-edge noise were often met with diminished aerodynamic performance [14, 42–44].

The early theoretical and numerical work of Howe [45] on porous plate acoustics modeled a point vortex passing over a trailing edge to show that the presence of perforations could reduce trailing-edge noise significantly. Computational simulations by Khorrami and Choudhary [46] indicated that the presence of porosity on a flat plate can reduce sound by reducing the strength of acoustic scattering at the edge by modifying the hydrodynamic noise source itself.

Further experiments investigated the acoustic and aerodynamic effects of fully- and partially-porous airfoils in an aeroacoustic wind tunnel with a microphone array and a force balance setup to measure changes in lift and drag [14, 42]. These experiments used porous SD 7003 airfoils composed of various foams, where the presence of porosity reduced aerodynamic noise by up to 10 dB for frequencies less than 10 kHz. The reductions in noise depended strongly on the flow resistivity of the porous medium, and these porous airfoils generated excess noise at frequencies above 10 kHz. Later theoretical works modeled chordwise-varying porosity inspired by the flow resistivity of owl wings in aerodynamic [47, 48] and acoustic [49] contexts, where the latter study found that varying the pore distribution of perforated surfaces can lead to greater noise reductions than in the case of uniform porosity. These studies also showed changes in directivity due to porosity and overall noise level reductions.

In addition to other works categorizing permeable materials by porosity, flow resistivity [50] (which is directly connected to permeability), and tortuosity [51, 52], more recent studies have characterized porous designs by their acoustic impedance. In the study by Jiang [44], porous material characteristics such as hole size and spacings were selected according to the characteristic acoustic impedance and the absorption coefficient, as measured by an impedance tube using the transfer function method of Chung and Blaser [53, 54]. Their study showed that porous edge extensions, compared to a nonporous airfoil, reduce low-frequency noise but increase noise at higher frequencies, except when paired with serrations, which are known to reduce high-frequency noise successfully [31]. The increase in noise at high frequencies has been observed and attributed in many other studies as being due to a surface roughness effect [14, 42–44, 55]. Other flow noise experiments on porous-coated cylinders found similar increases by the porous treatments at high-frequency ranges [56, 57]. In addition, recent numerical simulations have shown this excess noise to be caused by an acoustic dipole arising from interactions of edge-induced flow separation with the suction-side surface of a NACA 0012 airfoil [58]. While increases of noise by porous edge-treatments at high frequencies are well-documented in the research literature [14, 42–44], there is more work that can be done to experimentally investigate the mechanisms leading to this excess noise, and the use of porosity to reduce noise in other frequency ranges should not be discounted.

Porous designs may also be tailored to reduce bluntness noise. Showkat Ali et al. [59] investigated experimentally the use of porous treatments to reduce bluntness noise occurring at $St \approx 0.2$. In their best case, they found that highly-permeable materials could reduce the maximum tonal noise by 35 dB [59], but this level of noise reduction depended strongly on the permeability and volumetric porosity of porous materials. They also found that the use of porous edges helped to reduce the flow velocity and acceleration about the edge, which is thought to weaken vortex-shedding events at that location. In addition to porous metal foams, structured porous edges have also demonstrated the ability to reduce bluntness noise in experimental studies [60, 61]. Multiple computational studies have demonstrated the ability of porosity to reduce TE bluntness noise on flat plates. For example, in a large eddy simulation (LES) numerical campaign, Bae et al. [62] found that porous TE treatments can reduce the vortex shedding frequency by 13 dB, and Koh et al. [20] used an LES/computation aeroacoustics (CAA) method simulation that found the overall sound pressure level generated by a finite-edge flat plate can be reduced by up to 12 dB through the use of edge porosity.

1.2 Unresolved issues and research questions

While these prior studies demonstrated that porosity can successfully reduce overall broadband noise and bluntness tonal noise, the question remains how porosity and its realization as a geometric design affect the acoustic power scaling on flow speed for bodies in a flow. Also, the effects of porosity in the form of holes (or perforations) on bluntness noise have yet to be investigated from a combined acoustical and hydrodynamical perspective. These technical challenges are addressed in the present work through the lens of theoretical guidance from the dimensionless porosity parameter that governs the problem to discern if and when geometrical effects of porosity designs have an impact on flow noise from porous edges.

Experiments at the Applied Research Laboratory at the Pennsylvania State University were the first to experimentally investigate this porosity parameter δ to describe how edge permeability affects the scattered sound field. Preliminary results from a vortex-ring setup in a quiescent fluid show the U^5 sound power exponents can be achieved with the use of robust-primary component analysis for a nonporous edge [63] and favorable changes in sound power and directivity are achieved at different values of δ [64, 65]. However, a companion experiment to confirm these results using a turbulent boundary layer to generate the trailing-edge noise is currently lacking.

The studies discussed here and in previous sections lead to the following unresolved issues:

- Lack of assessment of aeroacoustic tunnel data in terms of the dimensionless porosity parameter, and identification of this parameter's limitation to describe real flow effects
- Unconfirmed cause of high-frequency noise increases by the presence of surface porosity
- Lack of demonstration of edge porosity as a noise control method applied to a real-world setting

These unresolved issues motivate the following research questions, which are investigated in the comprehensive experimental campaign detailed in this dissertation.

- How do surface perforations affect the acoustic far field and the local hydrodynamic flow field of flat plates?
- Can the dimensionless porosity parameter identified in acoustic scatter problems in a quiescent fluid be extended to anticipate changes in noise generated by a turbulent boundary layer over a porous edge?
- Do changes to pore shape or their distribution over a surface lead to measurable changes in the acoustic or hydrodynamic field when the porosity parameter is fixed?
- Can effective passive noise control based on edge porosity be realized on a flying vehicle?

1.3 Dissertation overview

The purpose of this dissertation is to examine experimentally, for the first time, the sound field and source regions of porous flat plates with blunt and sharp TEs. The porosity is characterized by a dimensionless porosity parameter, in a fluid flow over a range values. Chapter 2 details the various experimental setups, measurement techniques, and data analysis methods used in this dissertation. Chapter 3 presents various results on the effect of porosity on the acoustic field. This effort is carried out using microphone arrays within two anechoic wind tunnels. Changes in sound pressure level and directivity are measured in complement to the central focus on the reduction of noise engendered by porous edges. Next, hot-wire anemometry measures the turbulent velocity field for a nonporous and select porous plates; these results are presented in §4 and establish connections between the acoustic and flow fields. In §5, a remote-controlled aircraft is modified with a porous trailing edge and on-board surface pressure level measurements are taken to compare the effect of a nonporous and porous edge. The effects of pore shape and distribution on the resulting acoustic and hydrodynamic fields are also analyzed for all measurements. Lastly, concluding remarks are made in §6. Figure 1.3 illustrates the inspiration and flow of the

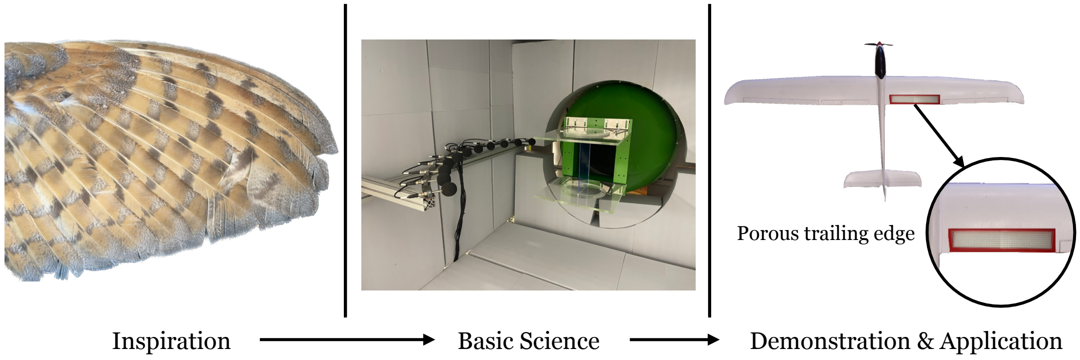

Figure 1.3: A biologically-informed engineer's approach to reduce noise using porosity. The porous planform of the owl wing (left) and the analyses it inspired leads to focused wind tunnel tests with porous plates for validation of the physical mechanisms (middle), which are then adapted for small-scale aircraft with porous trailing edges to assess real flow and aerodynamic effects (right). Reproduced wtih permission from *Springer Nature* [66].

research presented in this dissertation, where biology inspires designs that are tested in a controlled anechoic wind tunnel environment and then applied to a real-world test case of a remote-controlled glider.

Chapter 2

Experimental methods

The flow noise experiments reported in this dissertation took place at several testing locations and on various platforms and test specimens. Wind Tunnel Campaign 1 (WTC-1) consists of acoustic and flow measurements made in the aeroacoustic wind tunnel at Brandenburg University of Technology on a set of porous flat plates with blunt or sharp trailing edges. Wind Tunnel Campaign 2 (WTC-2) investigates the effects of spanwise-varying porosity on bluntness noise in the anechoic wind tunnel at the University of New South Wales. Lastly, a remote-controlled airplane was outfitted with porous trailing edges to measure pressure fluctuation aboard the vehicle during a glide phase. These measurements are reported in the Remote-Controlled Glider Campaign (RCGC) and were carried out at Lehigh University. This chapter comprises the design methodology of the porous plates and presentation of assorted experimental setups in detail.

2.1 Design of porous plates and edges for flow noise measurements

This section describes the design of the porous plates and edges for the campaigns WTC-1, WTC-2, and RCGC.

2.1.1 Porous plates for Wind Tunnel Campaign 1 (WTC-1)

The experimental apparatus involves 0.17 m (chord length) × 0.30 m (span width) × 0.003 m (thickness) acrylic plates that are designed with various hole shapes and spacings to cover a range of values of δ. The desired parametric range of δ is determined from the theoretical analysis of Chen et al. [15]. Subsequently, three groupings of plates, with low (L), medium (M), and high (H) permeability (or porosity) are designed and presented in table 2.1 and figure 2.1 to span from the effectively-impermeable, to the transitional, to the highly-porous behaviors of porous edge noise. In contrast to its adaption for a vortex ring in Chen et al. [15] using the vortex ring speed as the velocity scale, the dimensionless porosity parameter δ is here set by (1.1) and depends inversely on frequency f, which is any selected frequency within the acoustic spectrum of the flow noise generated by the plate. Specifically, the plates are designed for noise measurements within the 500 Hz to 4 kHz range, where each group (L, M, H) has a similar theoretical δ at the same frequency. The lower bound of this range, 500 Hz, is set by the lowest frequency that can be accurately measured due to the signal-to-noise ratio of the aeroacoustic wind tunnel facility with background noise. The upper bound of this range, 4 kHz, is chosen due to the manufacturing limitations of the plates. In order to maximize δ at higher frequencies (see (1.1)), the smallest hole radius, R, was chosen that could be reliably manufactured.

Circular and square holes with both aligned and offset hole patterns (with respect to the flow direction) are investigated to examine how changes in hole geometry might affect local flow and its generated noise and associated directivity. These different hole spacings are depicted in figure 2.1. The holes are manufactured by a 75-W Universal Laser Systems model PLS6 150D laser cutter. Half of the hydraulic diameter is taken for R for the square holes. The low-parameter plates, labeled starting with L (see table 2.1), enable δ in Zone 1 in figure 1.2; the medium parameter plates, labeled starting with M, enable δ in Zone 2, and the high parameter plates, labeled starting with H, enable δ in Zone 3. Also, an impermeable plate is included for reference comparison. Circular and square holes are chosen to test the effect of different hole shapes, as geometrical effects (besides the hole

Table 2.1: WTC-1 test plate information

Name	Hole type	R, mm	s, mm	α_h, %	δf, Hz
L1	Circular aligned	0.9	12.5	1.6	1.24×10^3
L2	Circular unaligned	0.9	12.5	1.6	1.24×10^3
L3	Square aligned	0.9	19.5	0.86	0.664×10^3
L4	Square unaligned	0.9	19.5	0.86	0.664×10^3
M1	Circular aligned	0.9	5.0	10	7.72×10^3
M2	Circular unaligned	0.9	5.0	10	7.72×10^3
M3	Square aligned	0.9	8.0	5.1	3.94×10^3
M4	Square unaligned	0.9	8.0	5.1	3.94×10^3
H1	Circular aligned	0.9	4.0	16	12.4×10^3
H2	Circular unaligned	0.9	4.0	16	12.4×10^3
H3	Square aligned	0.9	4.9	13	10.1×10^3
H4	Square unaligned	0.9	4.9	13	10.1×10^3

size) and their associated real flow effects are not captured by δ and are therefore unknown.

All plates were equipped with approximately 12-mm wide strips of anti-slip tape on both sides at a chordwise location of $x/c_l = 0.10$ to force transition and thus ensure the presence of a turbulent boundary layer at the trailing edge. In addition to the main goal of investigating the acoustic and flow fields of the fully porous plates, i.e., hole distribution spanning the entire plate, select porous plates were modified in-situ to allow for only 25%, 50%, and 75% of the chord to be porous. This allowed for comparing the effects of a partially-porous chord. The plates were manufactured originally with blunt trailing edges, and the same set of plates was then sharpened to have a trailing edge that is 0.5 mm thick. Lastly, the H1 porous plate was remade using resin 3D printing where every hole on the plate was filleted in an attempt to investigate the effect of the rim sharpness of the through-holes. Three fillet radii are tested: 0.5 mm, 1 mm, and 1.5 mm, and the corresponding plates are named H1a, H1b, and H1c respectively. Versions of the H1 plate with a blunt TE, sharp TE, and sharp TE with filleted through-holes are depicted in figure 2.2.

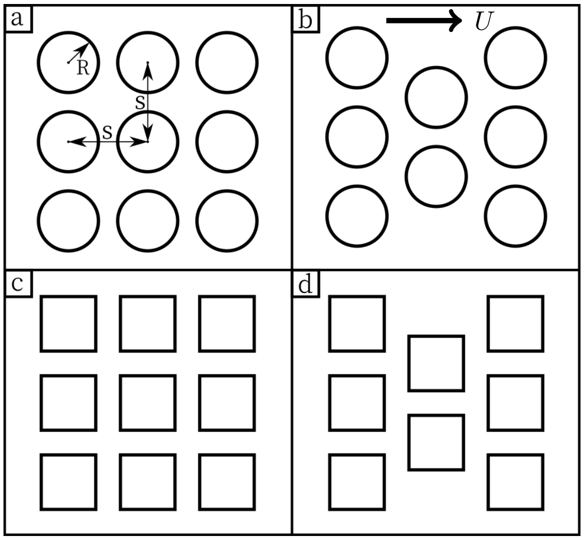

Figure 2.1: Layout for (a) circular aligned, (b) circular unaligned, (c) square aligned, and (d) square unaligned holes. Flow direction is from left to right.

2.1.2 Porous plates for Wind Tunnel Campaign 2 (WTC-2)

2.1.2.1 Trailing-edge extensions with spanwise-varying hole spacings

Select flat-plate trailing edge extensions are chosen from a set of plates used by Ayton et al. [67] to test the effect of spanwise-varying porosity on bluntness noise reduction as spanwise coherence structures may lead to increases in generated noise [50]. The three series of plates used are labeled a, b, c, which are the same plates as the 10-Series, 50-Series, and 60-Series, in Ayton et al. [67] respectively, and are simply renamed here. These plates were designed for leading-edge inflow turbulence noise reduction and have different hole geometry and spacings. A nonporous plate is also tested in this study for reference. The geometry for each of the different series of porous plates is shown in table 2.2. Within each series, three different plates with different spanwise hole spacings are tested: plates a|1, b|1, and c|1 have uniform hole spacings, plates a|2, b|2, and c|2 have hole spacings in the spanwise direction that are optimized for leading-edge noise reduction, and plates a|3, b|3, and c|3 have a randomized spanwise hole spacing. Plates of the same hole spacing type X|1, X|2, and X|3 are denoted in the results sections. Figure 2.3a shows a depiction of the uniform spacing, while figure 2.3b shows a sample optimized spacing, and figure 2.3c

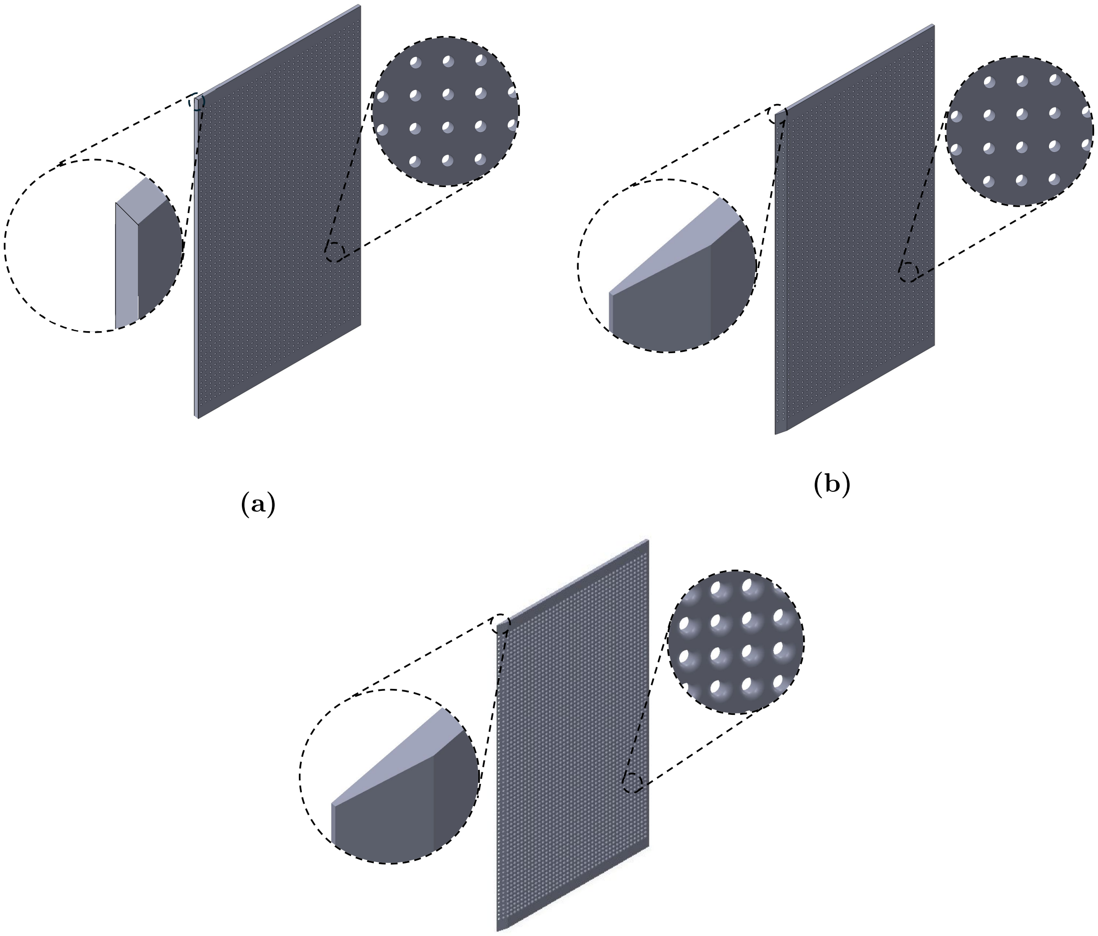

(a)

(b)

(c)

Figure 2.2: Closeup of plates used in WTC-1 with (a) blunt TE, (b) sharp TE, and (c) sharp TE with filleted through-holes. Close-up is on the TE. Orientation is such that the microphone arc-array is on the left side of the plate and the planar array is to the right side.

shows a depiction of randomized hole spacing in the spanwise direction. The plates with an optimized and random hole spacings are characterized by λ, which is the period over which the holes are varyingly spaced in the spanwise direction and is depicted in figure 2.3b. Each plate in each series has the same hole size and spacing in the chordwise direction. We anticipate, in the same way that theoretical models predict similar effects with leading- and trailing-edge serrations [22, 68, 69], that these optimized porosity inserts applied to the trailing edge could enhance TE noise reduction versus the non-optimized porosity inserts.

However, tonal and roughness noise effects are not modeled in the optimized theoretical model in Ayton et al. [67], and it is therefore unknown how these effect may be influenced by the optimized and random spacings.

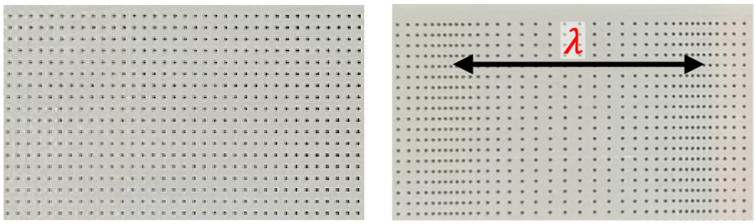

(a) Uniform spacing **(b)** Optimized spacing

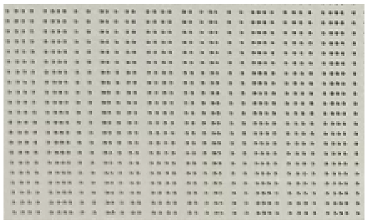

(c) Random spacing

Figure 2.3: Closeups of the hole spacing for the plates with spanwise-varying holes tested in WTC-2. The spanwise direction of the edge is from left to right, and the flow direction is from top to bottom.

Table 2.2: Definition of the baseline porosity for WTC-2 plates

Name	Spacing	R, mm	s, mm	α_h, %	holes/λ	λ, mm	δf, Hz
a|1	Uniform	0.5	2	19.6	-	-	27.2×10^3
a|2	Optimized	0.5	2	19.6	18	36	27.2×10^3
a|3	Random	0.5	2	19.6	18	36	27.2×10^3
b|1	Uniform	0.4	2	12.6	-	-	22.0×10^3
b|2	Optimized	0.4	2	12.6	24	48	22.0×10^3
b|3	Random	0.4	2	12.6	24	48	22.0×10^3
c|1	Uniform	0.4	1.6	19.6	-	-	34.1×10^3
c|2	Optimized	0.4	1.6	19.6	30	48	34.1×10^3
c|3	Random	0.4	1.6	19.6	30	48	34.1×10^3

Because δ depends on frequency and thus must be evaluated at discrete frequencies, it is helpful to characterize the plates by their δf values. Using (1.1), the frequency based dimensionless porosity parameter for each series of plates can be determined. An assumption is made in the calculation of δf for plates with random and varying spaced spanwise holes,

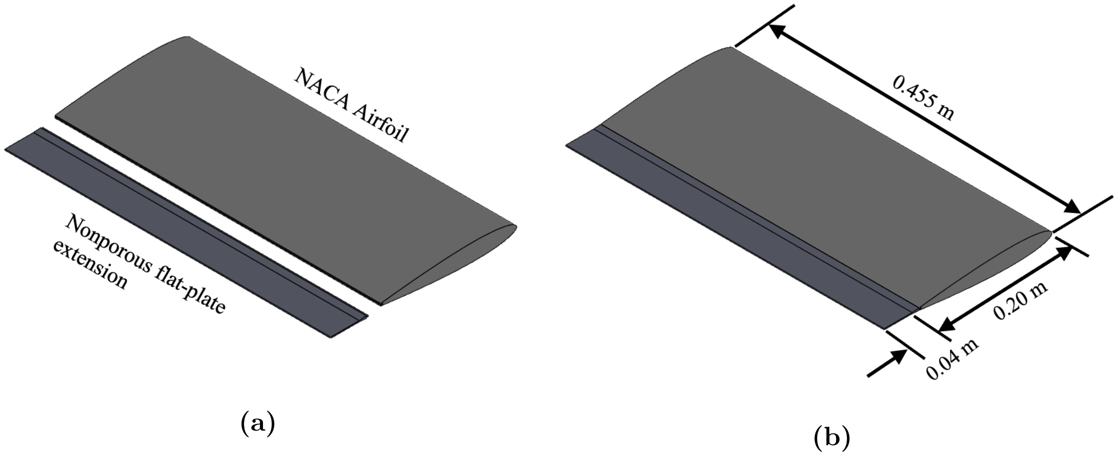

(a)

(b)

Figure 2.4: Airfoil model from WTC-2 at UNSW: (a) before and (b) after assembly.

namely, that the open-area fraction, α_h, is averaged over the entire length of the edge and thus is equal to the α_h for the uniformly-spaced holes in each respective series. This approach yields the following estimates of δf for the a, b, and c-series plates, respectively: 27.2×10^3 Hz, 22.0×10^3 Hz, and 34.1×10^3 Hz. From these values we can estimate that the c-series plates provide the best possibility for noise reduction, with the likelihood for noise reduction at frequencies of 3.4 kHz and below, or where $\delta \gtrsim 10$.

These flat-plate extensions were added to the end of a truncated NACA 0012 airfoil of span 0.455 m and chord length 0.20 m. The chord length of the flat-plate extensions adds 0.04 m to the chord length, making the total chord 0.24 m. This setup is illustrated in figure 2.4.

2.1.3 Porous edges for the Remote-Controlled Glider Campaign (RCGC)

Porous edges for the Remote-Controlled Glider Campaign (RCGC) are designed to reach the high-porosity limit of the porosity parameter δ. Three different edges are tested, each with a different type of hole geometry. The circular, square, and slit-shaped pore spacings are depicted in figure 2.5, and the following hole sizes and spacings are chosen such that each plate has a similar effective δf (see table 2.3). The circular hole radius $R = 2.25$ mm with an equal spacing that produces an open area fraction $\alpha_h = 0.44$. The squares are of side length $S = 6$ mm are are evenly spaced such that $\alpha_h = 0.25$, and the slits are 3-mm

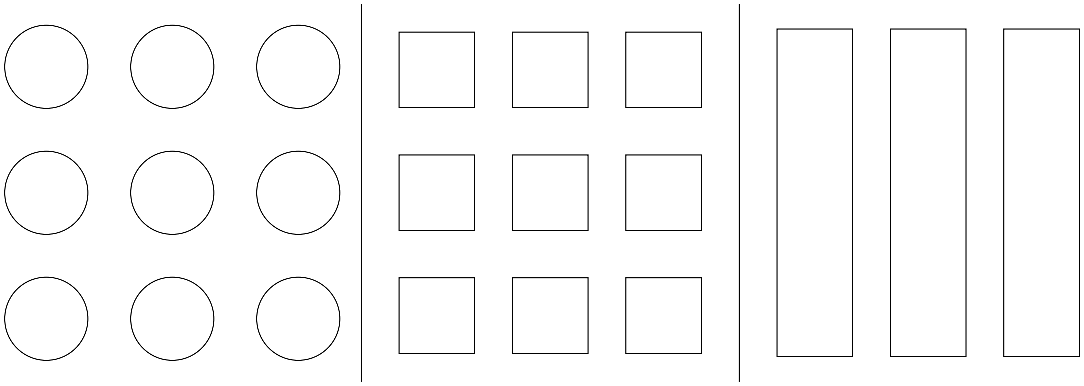

Figure 2.5: Schematic of circular (left), square (middle), and slit (right) hole spacing for RCGC. Flow direction from top to bottom. Holes and spacings are not to scale.

Table 2.3: Definition of baseline porosity for RCGC edges

Name	Hole type	Hole sizing	α_h, %	δf, Hz
P1	Circular aligned	$R = 2.25$ mm	44	13.6×10^3
P2	Square aligned	$S = 5$ mm	25	14.0×10^3
P3	Slits	3 mm × 60 mm	30	14.6×10^3

wide and 60-mm long with an $\alpha_h = 0.30$.

2.2 Measurement facilities and pieces of apparatus

This section describes the measurement facilities for the campaigns WTC-1, WTC-2, and RCGC located at the Brandenburg University of Technology, University of New South Wales, and Lehigh University respectively.

2.2.1 Brandenburg University of Technology aeroacoustic wind tunnel (WTC-1)

The experimental measurements were conducted in the small open jet aeroacoustic wind tunnel at the Brandenburg University of Technology (BTU) in Cottbus, Germany [70], as shown in figure 2.6. The nozzle in the experiments has a rectangular exit area with dimensions of 0.23 m × 0.28 m and a maximum flow speed of approximately 50 m/s. The flow speeds range from 9 m/s $< U <$ 40 m/s, which yield an estimated chord-based Reynolds number range of $1.03 \times 10^5 < Re < 4.48 \times 10^5$.

Rectangular sideplates made of acrylic glass are attached to the upper and lower edge of the nozzle. Similar to the setup described by Geyer at al. [71], circular rotatable discs are set into the sideplates. The flat plates under examination are mounted at both ends to these circular discs to allow for the adjustment of the geometric angle of attack. However, with the exception of experimental results presented in §3.3.1.3, all measurements are carried out at zero angle of attack.

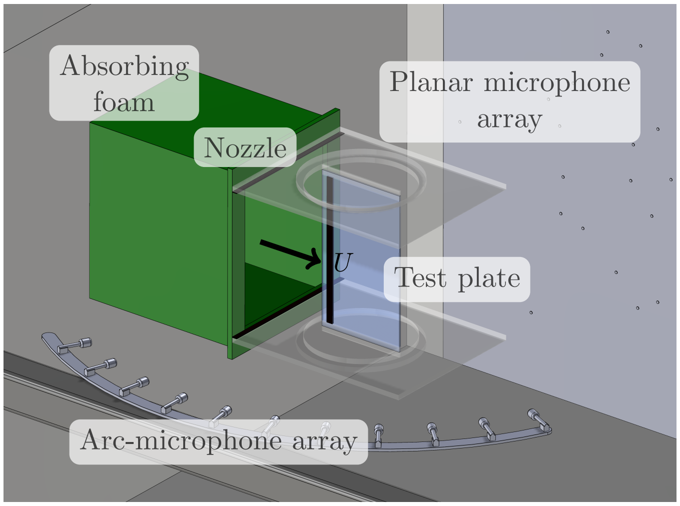

(a)

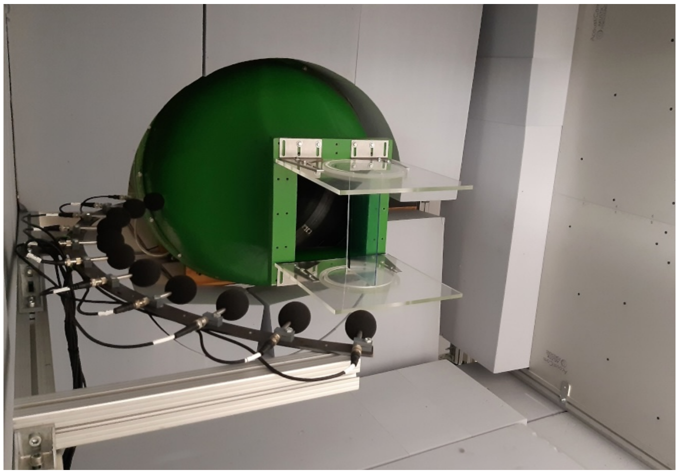

(b)

Figure 2.6: Labeled schematic (a) and photograph (b) of the experimental acoustic setup inside the aeroacoustic wind tunnel.

2.2.1.1 Microphone arrays

The acoustic measurements were performed with 11 1/4-inch free-field microphones located on an arc at one side of the test section, and with a planar microphone array located at the opposite side along one wall of the test section. The planar array consists of 56 1/4-inch Panasonic WM-61A microphones flush-mounted on a 1.5 m × 1.5 m aluminum plate. The data were synchronously recorded with a sampling frequency of 51.2 kHz and a duration of 40 s and stored on a RAID system. Post-processing was performed using the open source Python package *Acoular* [72]. For the measurements with single microphones, the temporal data were converted to the frequency domain using a Fast Fourier Transform (FFT) according to Welch's theorem [73], which was done on Hanning-windowed blocks with a size of 8,192 samples and with an overlap of 50 %, yielding a frequency resolution of 6.25 Hz. The results were then converted to sound pressure levels (SPLs) with a reference value $p_{\mathrm{ref}} = 20\,\mu\mathrm{Pa}$. The SPL (in dB) is calculated using

$$\mathrm{SPL} = 10\log_{10}\left(\frac{p^2}{p_{\mathrm{ref}}^2}\right), \tag{2.1}$$

where p^2 is the autospectrum of the microphone signal. The same FFT settings were used for the measurements with the planar microphone array, and various beamforming algorithms are applied on the resulting cross-spectral matrix using *Acoular* to extract the noise source locations and magnitudes. A 6 dB level is subtracted from the beamforming result to account for the reflection at the rigid array, thus leading to results that correspond to the value a single microphone would measure at the center of the array. Details on acoustic beamforming can be found in § 2.3.

To test if reflections from the planar array affected measurements from the radially-spaced microphones, comparison measurements were made with the planar array uncovered and covered by an acoustically absorbent material. Acoustic spectra measured from the radially-spaced microphones showed no noticeable difference between the two cases (see §A.2).

2.2.1.2 Hot-wire anemometry setup

Hot-wire anemometry measurements were performed using a DANTEC Dynamics hot-wire system and a 55P15 boundary-layer probe. The data were recorded with a sampling frequency of 25.6 kHz and a duration of 10 s. The measured velocity profile is taken as $\overline{U}/U$, where $\overline{U}$ is the average velocity at each measurement point, and U is the freestream velocity. $\overline{U}$ is calculated from N samples as

$$\overline{U} = \frac{1}{N}\sum_{i=1}^{N} U_i. \tag{2.2}$$

In addition, the intensity of the turbulent velocity fluctuations is calculated as

$$Tu = \frac{U_{\mathrm{rms}}}{\overline{U}}, \tag{2.3}$$

where the root-mean-square of the turbulent velocity fluctuations collected over N time samples is

$$U_{\mathrm{rms}} = \sqrt{\frac{1}{N}\sum_{i=1}^{N}(U_i')^2}, \tag{2.4}$$

and the turbulent velocity fluctuations are

$$U_i' = U_i - \overline{U}. \tag{2.5}$$

Hot-wire anemometry measurements were performed in the near wake and upstream boundary layer of selected plates to analyze the flow field and how it is affected by the presence of a porous boundary. These temporal data of the turbulent velocity fluctuations were transferred to the frequency domain using the same functions described above for the acoustic signals to obtain the spectra of the turbulent velocity fluctuations, Φ, with a frequency resolution of 3.125 Hz.

To better understand the influence of porous plates on the boundary layer, the boundary-layer thickness, displacement thickness, momentum thickness, and shape factor are calcu-

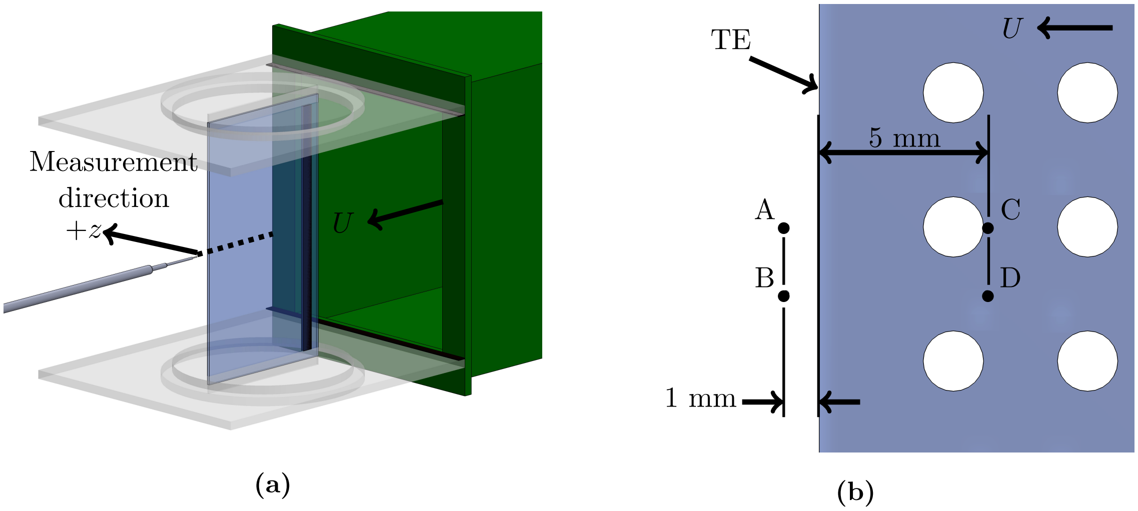

Figure 2.7: (a) hot-wire anemometry setup schematic and (b) closeup on porous TE with labeled spanwise and chordwise positions for the near-wake (A and B) and upstream (C and D) measurements.

lated from the hot-wire data. The boundary-layer thickness, h, from experimental measurements is taken as the height where the mean velocity reaches 99% of the freestream velocity. The boundary-layer displacement thickness, δ^*, and the momentum thickness, θ, are calculated in the standard manner [74]:

$$\delta^* = \int_0^\infty \left(1 - \frac{\overline{U}(z)}{U}\right) dz, \tag{2.6}$$

$$\theta = \int_0^\infty \left(1 - \frac{\overline{U}(z)}{U}\right) \left(\frac{\overline{U}(z)}{U}\right) dz, \tag{2.7}$$

where z is measured normal to the solid boundary, positive into the flow. The shape factor,

$$H = \frac{\delta^*}{\theta}, \tag{2.8}$$

follows as the ratio of the displacement thickness and momentum thickness. The measurement setup is detailed in figure 2.7a, and figure 2.7b illustrates the streamwise (x) and spanwise (y) locations of the measurements. The hot-wire anemometry measurements were taken in two regions of the plate: 1 mm behind the TE in the near-wake region and 5 mm upstream from the TE. The measurement locations for the near wake are labeled as points (A) and (B), and the upstream measurement locations are labeled as points (C) and (D) in figure 2.7b. The spanwise location of points (A) and (C) is aligned with the center of a pore and the spanwise location of points (B) and (D) are aligned with the gap between two pores. The near-wake measurements sweep from one side of the plate to the other in the vertical direction, and the upstream measurements begin at a z distance of 2.5 mm from the plate surface to ensure that the probe does not accidentally come in contact with the test plate.

2.2.1.3 Tunnel characteristics

Initial flow measurements were taken at center span at a distance of 0.09 m from the nozzle exit to analyze the flow field in the absence of an installed test plate. This distance corresponds to the leading edge location of the plates. A potentially significant source of flow noise is leading-edge turbulence-interaction (LE TI) noise, which is produced by the interaction of free-field turbulence with the LE. As LE TI noise is not of focus in this study, it is crucial that the inflow turbulence is low to minimize its impact on the acoustic field. The measured velocity profile at the LE location is essentially uniform and has a very low turbulence intensity, Tu, of approximately 0.24% at the center point (see figure 2.8).

In addition to low inflow turbulence, it is crucial that the background noise of the tunnel is quieter than the noise generated at the TE. To ensure low background noise, the test apparatus is contained within a cabin that is covered in acoustically absorbent walls, except for the planar microphone array (see figure 2.6). Despite the planar microphone being fully reflective, no noticeable effects were observed in comparison measurements made with the microphone array either covered and uncovered by acoustically absorbent material. Figure 2.9 depicts the overall sound pressure level (OSPL) of the empty tunnel as a function of freestream velocity, calculated from 300 Hz to 10 kHz using:

$$\mathrm{OSPL} = 10\log_{10}\left(\sum_i 10^{\mathrm{SPL}_i/10\ \mathrm{dB}}\right)\mathrm{dB}, \tag{2.9}$$

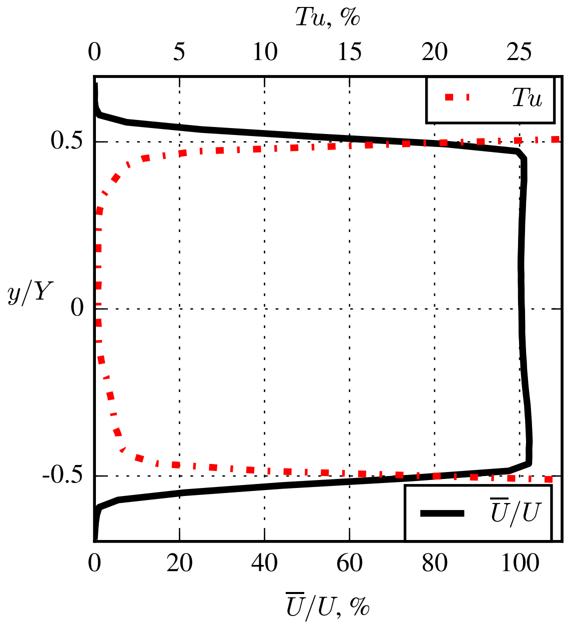

Figure 2.8: Flow conditions for empty tunnel at the location of the leading edge of the plates ($\overline{U}/U$ and Tu for $U =$ 30 m/s).

where SPL_i is the individual SPL at each frequency band, in dB. The tunnel has very low background noise, below 60 dB at the highest tested velocity.

2.2.2 University of New South Wales aeroacoustic wind tunnel (WTC-2)

Acoustic measurements were performed in the UNSW Anechoic Wind Tunnel (UAT), an open-jet wind tunnel with a 0.455 m × 0.455 m test section housed within a 3 m × 3.2 m

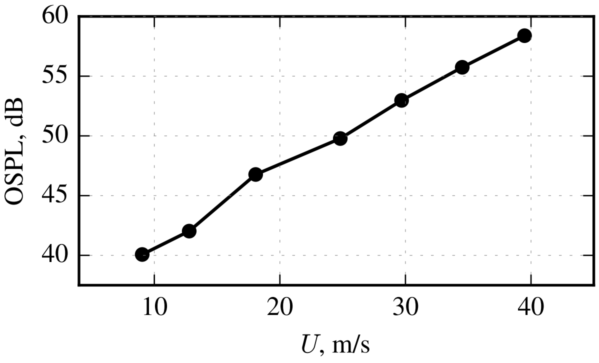

Figure 2.9: OSPL vs. U for empty BTU tunnel.

× 3.15 m anechoic chamber [44]. Figure 2.10a illustrates the setup and labels its key points. This wind tunnel can provide uniform flow speeds across the entire exit area from approximately 10 m/s to 50 m/s, where the flow speeds tested for this work are 17.8 m/s $< U <$ 45.0 m/s, which result in an effective chord-based Reynolds number of $2.94 \times 10^5 < Re < 7.44 \times 10^5$.

The model used for testing is a NACA 0012 aluminum airfoil with chord length $c_l =$ 0.20 m. Porosity is added to the trailing edge in the form of 1.6 mm thick, 0.04 m long flat plate extensions of full span, which is illustrated in figure 2.10b. These extensions fit flush into a slot at the TE of the NACA 0012 airfoil, providing a final c_l of 0.24 m. See figure 2.4 for a graphic of the airfoil/flat-plate extension assembly.

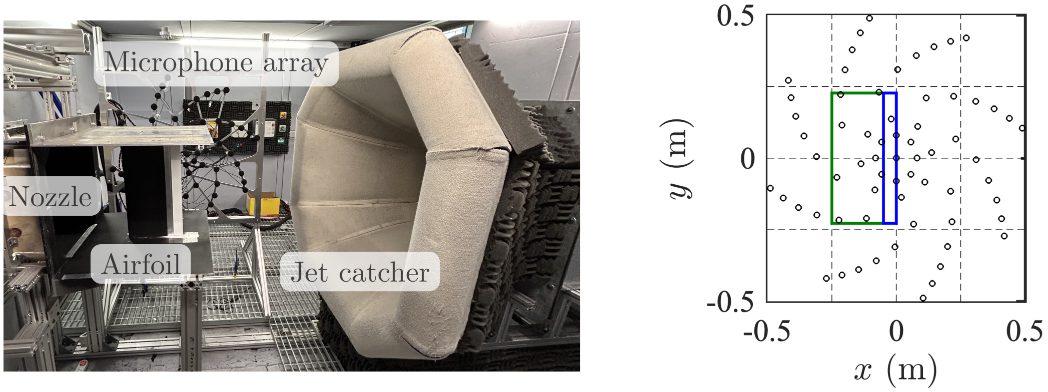

(a) **(b)**

Figure 2.10: University of New South Wales Anechoic Wind Tunnel and acoustic array. (a) Photograph of the experimental setup and (b) schematic of the airfoil (—) with porous trailing edge extension (—) and array microphones (o). Flow direction from left to right.

2.2.2.1 Microphone array

A 65-microphone array, centered at the mid-span of the TE, captures acoustic data at 65,536 Hz for 32 s for each test scenario. Time-domain data are converted to the frequency domain using a Fast Fourier Transform (FFT) according to Welch's method [73], which was done using Hanning-window blocks with a size of 4096 samples with an overlap of 50%. The same FFT settings are used in the generation of the cross-spectral-matrix (CSM), needed for beamforming calculations. CLEAN-SC, a deconvolution beamforming algorithm [75], is utilized to generate soundmaps using the microphone array with a resolution of 0.01 m using UNSW in-house beamforming code.

2.2.2.2 Tunnel characteristics

The UNSW Anechoic Wind Tunnel has very low background noise and a very low turbulence intensity along the jet core center of approximately 0.22% to 0.62% [44]. Further detailed analysis of the tunnel characteristics can be found in Jiang [44, § 3.3.1].

2.2.3 Remote-Controlled Glider Campaign testbed (RCGC)

The experiments for the Remote-Controlled Glider Campaign (RCGC) were conducted using the *Volantex 759-3 Phoenix 2400* remote-controlled aircraft. This aircraft was modified to investigate the effects of porosity on surface pressure levels using a modified edge which allowed for the changing of porosity, in addition to on-board data acquisition to capture real-time velocity and acoustic data.

The glider had a 2.40 m span and a maximum chord length of approximately 0.300 m. The wing shape is an estimated NACA 0012 airfoil. The aircraft was chosen as it is very stable in flight, can carry a large payload, and has a similar chord length to the barn owl, one of the most common owl species that demonstrates the silent flight behavior [4]. The glider is controlled with a *Taranix Q X7* digital telemetry radio system. The right-side flap of the glider aircraft was modified with an interchangeable porous trailing edge as detailed in figure 2.11. The flap was removed, and a hollow-frame of the edge was 3D-printed. Various flat porous plates, detailed in figure 2.11b and discussed in §2.1.3 were placed on the top and bottom surfaces of the frame to create the porous edge. Note that the location of the fuselage microphone, shown in figure 2.11a but not depicted in figure 2.11b is on the fuselage approximately 5 cm upstream from the TE. The space between the bottom and top surface was left hollow. The following section describes the data acquisition process.

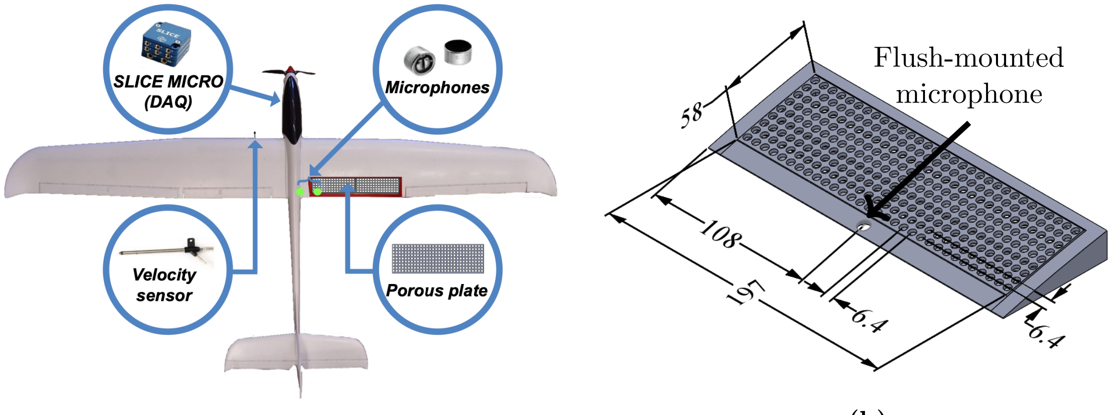

(a) (b)

Figure 2.11: (a) Schematic of aircraft test bed setup DAQ, sensors, and sample P1 porous plate; (b) closeup on porous TE. Key dimensions labeled in millimeters.

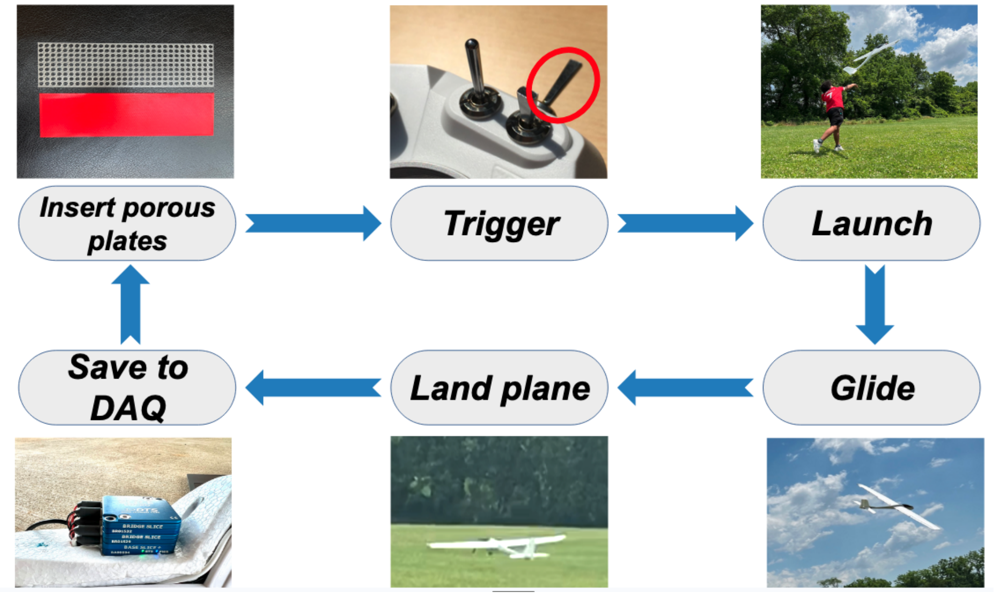

Figure 2.12: Aircraft testbed setup with DAQ, sensors, and porous plate.

2.2.3.1 Glider data acquisition methodology

A DTS SLICE Micro data acquisition system (DAQ) synchronously captured on-board acoustic and velocity data. A customized circuit was designed to wait for a manual switch to be flipped on the controller, which then triggers the recording on the SLICE Micro. This protocol is illustrated in figure 2.12. The microphones are electret Panasonic WM-61A, and the pitot tube, used to measure flight speed, is model ASPD-7002 from Matek Systems. The microphones were calibrated against a 94 dB, 1 kHz tone using a REED R8090 sound level calibrator. The pitot tube was calibrated using a 0.46 m × 0.46 m closed-loop subsonic wind tunnel at Lehigh University. The data were sampled during takeoff, flight, and landing for a total of 25 s at 25 kHz. The pitot tube quasi-steady temporal pressure data were converted to velocities using the steady Bernoulli equation, and the temporal acoustic data were transferred into the frequency domain using an FFT with the same settings as described in §2.2.1.1. Before processing the acoustic data, the velocity data were analyzed to find periods of flight at near-constant flight speeds so that the effect of changing the porous edges could be compared across different flights. The pitot tube signal was observed in ground testing to be heavily affected by the spinning propeller, as the wake generated by the spinning propeller blades affected the pressure measured by the pitot tube; however, after switching the propeller off, during the steady flight, this noise in the pitot tube signal went away. This helped solve the problem of knowing when to analyze data from steady flight; as there is no accelerometer on board, the period after the noisy take-off is taken as the steady flight. Once these time periods were determined, acoustic data from multiple runs with the same porous treatment were averaged at similar flight speeds ranging from $7 \text{ m/s} < U < 12 \text{ m/s}$.

To analyze the relationships between microphone signals measured on the wing and fuselage of the aircraft, the magnitude-squared coherence of the signals frequency dependent and calculated using

$$\gamma_{ab}^2 = \frac{|G_{ab}|^2}{G_{aa}\, G_{bb}} \tag{2.10}$$

where G_{ab} is the cross-spectral density and G_{aa} and G_{bb} are the power spectral densities of the microphone signals [76]. Note that the magnitude-squared coherence γ_{ab}^2 is not related to the velocity scaling exponent referred to as γ.

2.3 Acoustic beamforming calculations

Acoustic beamforming is a broad term for a phased-microphone array processing technique that enables the generation of soundmaps and acoustic spectra of a noise-generating test specimen. The microphone array works like an acoustic concave mirror, where the focus point of the array is steered to each point in a region of potential noise sources, and the noise contributed by this point is measured [77]. This measurement technique seeks to solve two main goals: determining the location and strength of the noise sources.

Beamforming is used in the analysis of data from WTC-1 and WTC-2 in the BTU and UNSW wind tunnels respectively, where the layouts of the arrays have been designed for optimal beamforming measurements. The design of the corresponding arrays is not discussed in detail in this dissertation. However, the reader is referred to Sarradj et al. [70] for more information about the design of the array and wind tunnel at BTU and Wills et al. [78] for more information about the design of the array at UNSW.

Acoustic beamforming creates integrated soundmaps for the experiments in WTC-1 with sharp-edged plates only. For the experiments with blunt-edged plates, where bluntness noise dominates, the focus is on reduction of bluntness noise by the presence of porosity, and this assessment is accomplished by the use of hot-wire measurements, soundmaps, and acoustic spectra from *single* microphones. A deeper investigation into the various noise sources of the porous plates is conducted on the plates with sharp-edges using beamforming integration methods.

2.3.1 Definition of beamforming sectors for WTC-1

Acoustic beamforming is performed using a 0.507 m × 0.510 m grid centered upon the test plate. For beamforming calculations, the grid increment is 0.010 m for all types of beamforming except for DAMAS, where the grid size is 0.020 m in order to save computational time and space and due to the extremely large file size of DAMAS beamforming. Figure 2.13 detailed the wind tunnel setup, test plate, and sideplates with the various integration sectors: TE, LE, middle, top, and bottom of the sideplates. Figure 2.14 compares the spectra integrated from the various sectors for the nonporous plate with a sharp TE using three different beamformers: Orthogonal, CLEAN-SC, and DAMAS. These integrated spectra are compared to the averaged microphone autospectra of each microphone in the array, normalized to the distance to the center of the planar array (the location to which the beamforming results are normalized).

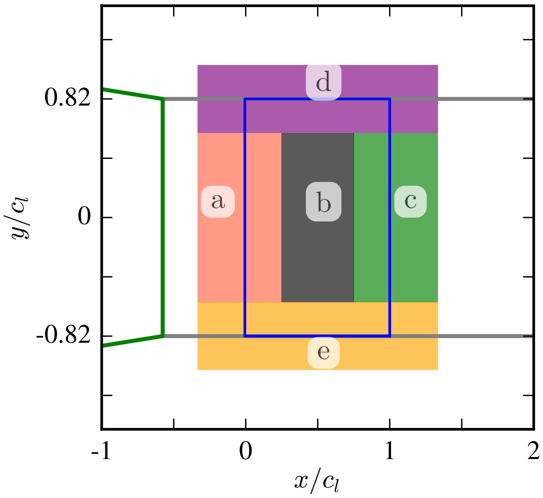

Figure 2.13: BTU wind tunnel test section with nozzle (—), test plate (—), and integration sectors: (a) LE, (b) middle, (c) TE, (d) top sideplate, and (e) bottom sideplate.

2.3.2 Comparison of beamforming algorithms for WTC-1

Various beamforming algorithms, including deconvolutions methods, are investigated for their use in analyzing acoustic data. The estimation of the location and strength of sound sources using conventional delay-and-sum (DAS) beamforming is estimated using

$$S_{XX}(p_{\mathrm{s}}(x,y)) = h^H(x,y)\,G\,h(x,y), \tag{2.11}$$

where $S_{XX}(p_{\mathrm{s}}(x,y))$ is the autopower spectrum of the point spread function at each grid point, h is the steering vector, and G is the cross spectra matrix of the microphone array estimated by the methods described in § 2.2.2.1. The superscript ^{H} denotes the complex conjugate. A drawback of this method is that the performance of the delay-and-sum beamformer is influenced by the source locations and microphone array characteristics such as layout [77].

Deconvolution methods seek to get around some of these challenges by imposing an initially unknown source distribution $q(x_\mathrm{s}, y_\mathrm{s}) p_\mathrm{s}(x, y|x_\mathrm{s}, y_\mathrm{s})$ and using an array-specific point spread function (PSF) in the following equation

$$S_{XX}(x, y) = \sum_{(x_\mathrm{s}, y_\mathrm{s})} q(x_\mathrm{s}, y_\mathrm{s})\, p_\mathrm{s}(x, y|x_\mathrm{s}, y_\mathrm{s}), \tag{2.12}$$

where $S_{XX}(x, y)$ is the beamforming map at the observer location, and $q(x_\mathrm{s}, y_\mathrm{s})$ is the source distribution, and $p_\mathrm{s}(x, y|x_\mathrm{s}, y_\mathrm{s})$ is the point spread function relating the positions of the observer and source. The goal is to find a source distribution that satisfies this equation given the constraint that the source is greater than zero [79]. Geyer [77] describes this process of the generation of the beamforming map in the following manner:

> "...[the process involves] adding several layers of sub–images, one layer for each noise source M, to obtain the image $S_{XX}(x, y)$, which is done for every point in the grid to receive the final image S_{XX}. Each sub–image is determined by the multiplication of the source positioned at $(x_\mathrm{s}, y_\mathrm{s})$ (the source distribution) with a transfer function that describes the influence of a monopole sound source, located at $(x_\mathrm{s}, y_\mathrm{s})$, on the grid point (x, y). Thus, the point spread function can be described as the response of the microphone array to a point source. The process of solving for each grid point involves adding a layer at each point for each noise source."

The point spread function (PSF) influences the results, and, thus, the goal of deconvolution beamformers such as CLEAN-SC and DAMAS is to reduce the effect of the PSF on the result. The following section describes and compares additional beamforming algorithms for use in this dissertation.

- **Functional beamforming**

Functional beamforming is a beamforming method introduced by Dougherty [80]. This method uses the functions of matrices in the algorithm, namely by raising the cross spectra matrix to the power of a reciprocal of a parameter [79]. Appropriate use of the parameter allows for attenuation of the side-lobes, which leads to an improved spatial resolution [79]. This method can provide up to a 30 times better dynamic range and 6 times better spatial resolution with respect to conventional delay-and-sum (DAS) beamforming [81, 82], without an increase in computation time; however, significant sidelobes are still present.

- **Orthogonal beamforming**

  Orthogonal beamforming was first proposed by Sarradj et al. [83], who realized that noise is often generated by sources independent of one another i.e., TE noise, nozzle noise, and junction noise. Thus, those temporally and spatially uncorrelated sources can be considered orthogonal and represented by the summation of these orthogonal components [79]. An eigenvalue decomposition of the cross spectra matrix of the microphone signals is performed to create a matrix containing the positive real-valued eigenvalues and a matrix containing the corresponding eigenvectors [77]. Orthogonal beamforming estimates the absolute source level, where each source is represented by a corresponding eigenvalue, and the peak in the eigenvector matrix is used to assign the location of the source. The main diagonal can also be removed, as is often done, to remove uncorrelated noise [84]. This deconvolution method is relatively fast and has the benefit that the integrated spectral levels are bounded by and will not exceed those of the individual microphone.

- **CLEAN-SC beamforming**

  CLEAN-SC beamforming is a deconvolution algorithm first introduced by Sijtsma [75]. CLEAN-SC is based on source coherence (SC) and begins by imposing an assumed PSF which acts as the focusing beam. It then iteratively searches for the peak location calculated using the conventional delay-and-sum. After this location is found, the coherent sources are removed from the PSF, thus, "cleaning" the beam [77, 79]. This action relies on the fact that the side-lobes are coherent with the main sources. This removal of the part of the map that is spatially coherent with the main source leads to an enhancement in dynamic range and spatial resolution [79], thus revealing the acoustic sources. This method is estimated to take only twice the time of conventional DAS beamforming [75].

- **DAMAS beamforming**

  Proposed by Brooks and Humphreys [85], the Deconvolution Approach for the Mapping of Acoustic Sources (DAMAS) is one of the most prolific deconvolution beamforming methods. It seeks to solve an exact solution of (2.12) by use of an iterative Gauss-Seidel-Technique to remove the convolution of the image of the sound sources within the point spread function [85]. The solving of the systems of equations governed by (2.12) becomes very complex, as there are as many equations as there are grid points, leading to even more numerical iterations. DAMAS is therefore extremely computationally intensive; however, it has the benefits of being very accurate at low frequencies [86].

To investigate the viability of beamforming, figure 2.14 compares spectra integrated from each sector of the plate using Orthogonal, CLEAN-SC, and DAMAS beamforming to the microphone autospectra average. The resulting SPL from beamforming calculations is calculated for an observer at the center of the array. Because of this, the integrated SPLs are compared to the average autospectra of each microphone, normalized to the distance of the center of the array. Figures 2.14a and 2.14b show that Orthogonal and CLEAN-SC provided integrated SPLs for the TE, LE, and middle plate section that are near zero at many low frequencies. Those data points likely follow from the fact that many beamforming methods inherently perform poorly at lower frequencies [86]. The near-zero values at low frequences ($f < 2$ kHz) in the TE spectra for Orthogonal and CLEAN-SC are not physical as TE noise is expected at this frequency. DAMAS beamforming, shown in figure 2.14c, is the only method that produces spectra free of unexpected and physically-inaccurate zeros at low frequencies. Because of the heavy computational demand of DAMAS calculations, its grid resolution is relatively course at 2 cm, compared to 1 cm for all other methods shown. Before choosing to move forward with the use of DAMAS and to investigate the effect of a smaller grid size, the beamforming calculation was re-run for a single test case using DAMAS with a grid resolution of 1 cm not shown in this dissertation. A difference of approximately ±1 dB was found between the levels integrated from the fine and coarse maps. Thus, DAMAS with the coarse grid resolution of 2 cm was used for all future beamforming integration of sound pressure levels in §3.3.

Figures 2.15 and 2.16 compare soundmaps created by the different beamformers: DAS, Functional, Orthogonal, CLEAN-SC, and DAMAS. The effect of side-lobes are clearly seen in DAS and Functional beamforming soundmaps whose source regions are much wider and spread-out compared to those found in Orthogonal and CLEAN-SC soundmaps using the same grid size. For the soundmaps of the nonporous plate shown in figure 2.15, all the methods locate mid- and high-frequency noise at the TE and junctions of the test plate with sideplates. For the soundmap of the H1 porous plate shown in figure 2.16, the poor dynamic range of DAS and Functional beamforming result in the soundmaps failing to uncover TE noise, as other noise sources dominate.

The CLEAN-SC method is chosen to produce the beamforming figures in this dissertation unless otherwise noted as it provides soundmaps with a good dynamic range that identify the many sources across the plate and has a low computation time. DAMAS is not used in future soundmaps as the coarse grid, while sufficient for integrating SPLs, yields soundmaps that are challenging to interpret for physical insight. The dynamic range of the soundmaps in figure 2.15 is 20 dB for the Orthogonal, CLEAN-SC, and DAMAS soundmaps, while the dynamic range for the DAS and Functional soundmaps is 5 dB. This range must be kept small due to the influence of the side-lobes on the soundmaps.

Lastly, figure 2.17 is included for direct comparison of the SPL calculated over the entire beamforming area compared to the average, normalized microphone autospectra. It can be seen that the three beamformers create spectra that are very similar in amplitude

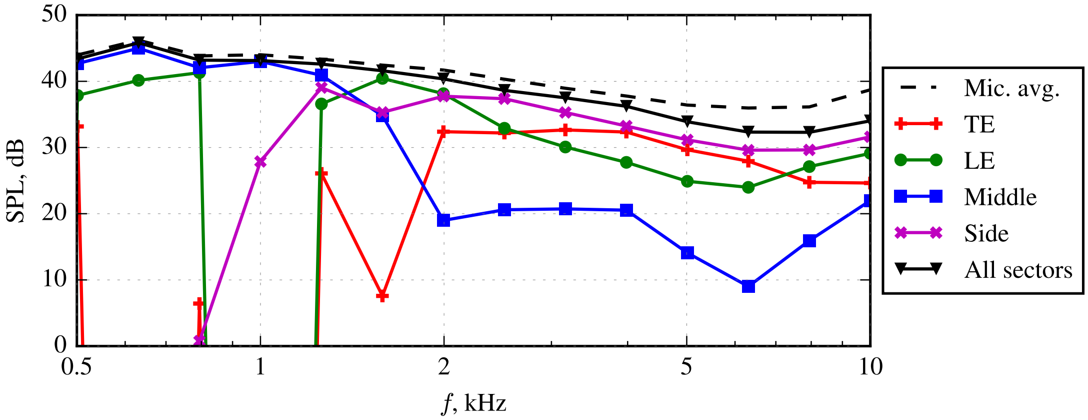

(a) Orthogonal

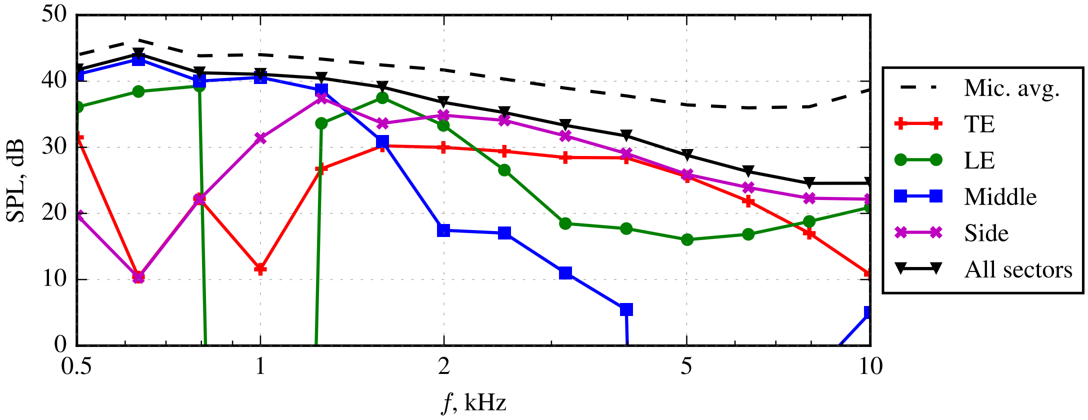

(b) CLEAN-SC

(c) DAMAS

Figure 2.14: Comparison of beamforming approaches and regions to microphone autospectra to determine effectiveness of different beamformers to generate integrated SPLs. Data presented for the nonporous plate with a sharp TE tested at $U = 30$ m/s.

to the microphone average, where Orthogonal beamforming creates spectra closest to that of the microphone average, then DAMAS, and CLEAN-SC. The result using DAMAS has a maximum difference from the microphone autospectra of 6 dB, similar to findings from Geyer [77], which is deemed sufficient for our analysis.

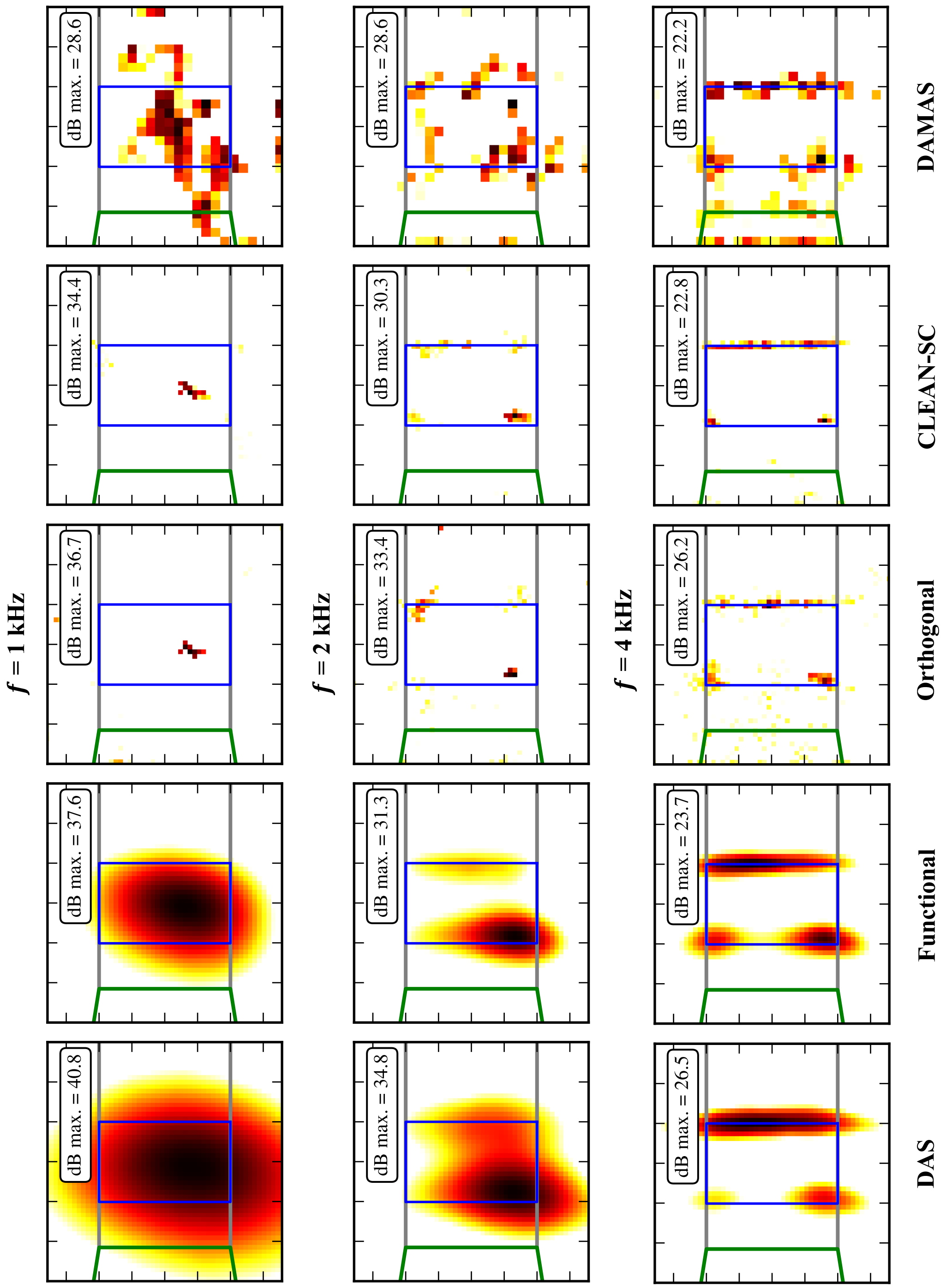

Figure 2.15: Comparison of soundmaps generated by DAS, Functional, Orthogonal, CLEAN-SC, and DAMAS beamforming at $f = 1$ kHz, $f = 2$ kHz, and $f = 4$ kHz for the sharp-edged nonporous plate at $U = 30$ m/s.

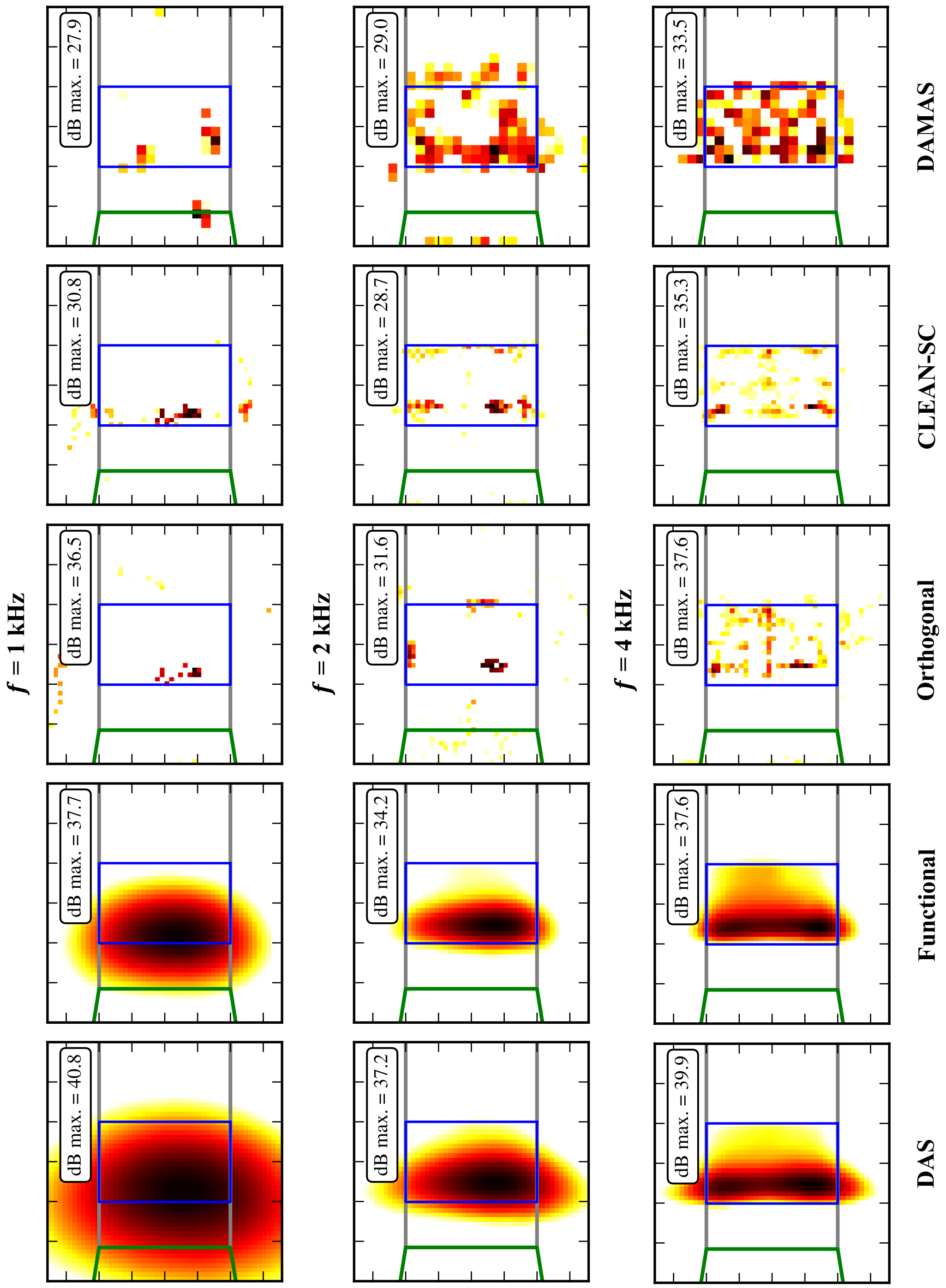

Figure 2.16: Comparison of soundmaps generated by DAS, Functional, Orthogonal, CLEAN-SC, and DAMAS beamforming at $f = 1$ kHz, $f = 2$ kHz, and $f = 4$ kHz for the sharp-edged H1 plate at $U = 30$ m/s.

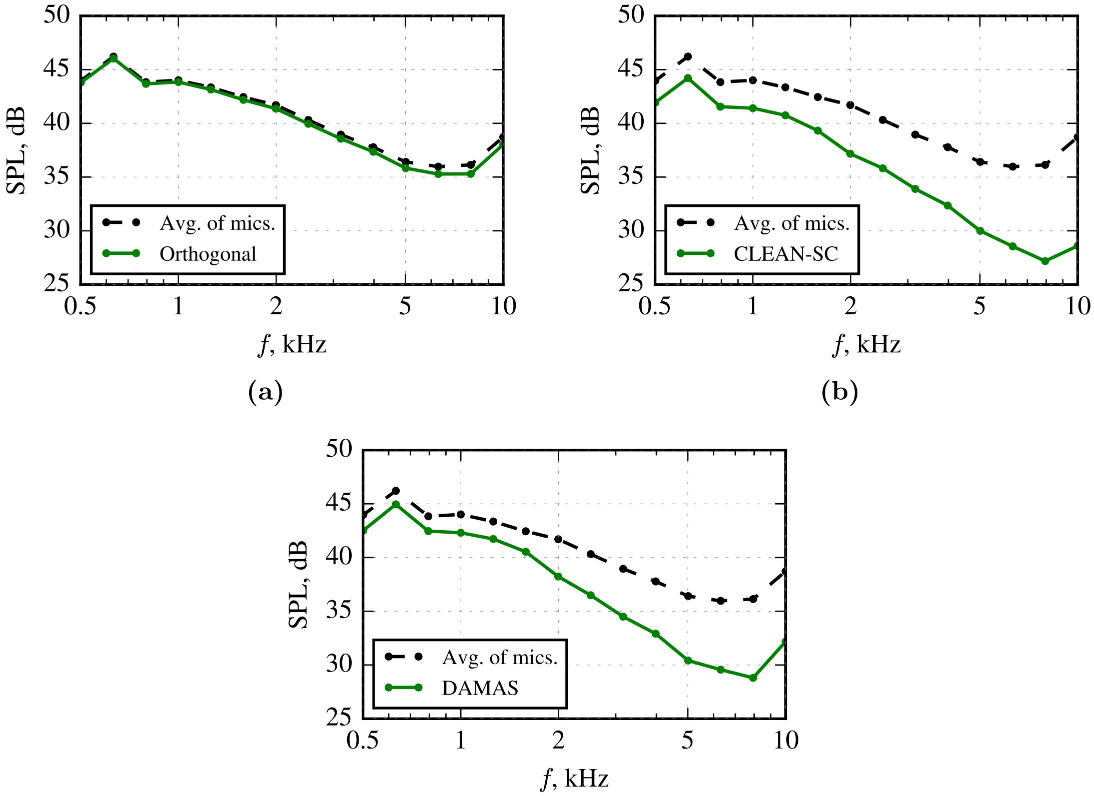

(a) **(b)** **(c)**

Figure 2.17: Spectra integrated by various beamformers for different sectors of the sharp-edged nonporous plate at $U = 30$ m/s.

2.4 Acoustic scaling on flow speed calculations

The acoustic scaling on flow speed of the OSPL and SPL at individual frequencies is investigated. First, the OSPL or SPL is calculated using (2.9) or (2.1) respectively. From these values, the corresponding p^2 sound pressure level is determined using the reference pressure p_{ref}. The slope of the best fit line of the $\log_{10} p^2$ against $\log_{10} U$ is taken as γ, the acoustic scaling exponent on the flight speed.

2.5 Uncertainty analysis

2.5.1 Uncertainty equations

The methods of Glegg & Devenport [87, §18] are used to evaluate uncertainty in the microphone and hot-wire measurements presented in this paper. The following uncertainty estimations are given at a confidence level of 95% and derived under the assumption that errors are random and are distributed normally. Instead of using $\delta[\cdot]$ as in Glegg & Devenport [87, §18], $\epsilon[\cdot]$ is used to denote the uncertainty while $E[\cdot]$ denotes the uncertainty relative to the base value.

- Power spectral density (PSD) estimator of G_{aa}

  The power spectral density estimator is used for estimating uncertainty of: microphone spectra, described in § 2.2.1.1 and spectra of turbulent velocity fluctuations, Φ, described in § 2.2.1.2. The uncertainty estimation of those measurements is as follows:

  $$\epsilon[G_{aa}] = \frac{2G_{aa}}{\sqrt{N_{\text{rec}}}}, \tag{2.13}$$

  where G_{aa} is the power spectral density and N_{rec} is the number of independently performed spectra averages. This value is calculated by

  $$N_{\text{rec}} = \text{int}\left[\frac{N/N_{\text{FFT}} - 1}{1-\beta}\right] + 1, \tag{2.14}$$

  where N_{FFT} is the number of samples in each independently performed spectral average, β is the overlap percentage, and the operator "int" refers to the integer value of the proceeding expression. From the uncertainty $\epsilon[G_{aa}]$, the relative uncertainty, $E[G_{aa}]$, is then calculated by

  $$E[G_{aa}] = \frac{\epsilon[G_{aa}]}{G_{aa}} = \frac{2}{\sqrt{N_{\text{rec}}}}. \tag{2.15}$$

  Noted that this quantity depends solely on N_{rec}.

- Cross-spectral density (CSD) estimator of G_{ab}

  The cross-spectral density estimator is used to estimate uncertainty of microphone cross-spectra, G_{ab}, which make up the cross-spectral matrix used for beamforming. The uncertainty estimation of this measurement is as follows:

  $$\epsilon[|G_{ab}|] = \frac{2\sqrt{G_{aa}G_{bb}}}{\sqrt{N_{\text{rec}}}}, \tag{2.16}$$

  where $|G_{ab}|$ is the magnitude of the cross-spectral density between two independent microphone measurements. The relative uncertainty, $E[|G_{ab}|]$ is then calculated by

  $$E[|G_{ab}|] = \frac{\epsilon[|G_{ab}|]}{|G_{ab}|}. \tag{2.17}$$

  Noted that this quantity is frequency-dependent.

- Magnitude-squared coherence estimator of γ_{ab}^2

  The magnitude-squared coherence estimator is used to estimate uncertainty of the γ_{ab}^2 of the two microphones on-board the remote-controlled glider. The uncertainty estimation of this measurement is as follows:

  $$\epsilon[\gamma_{ab}^2] = \frac{2\sqrt{2}\gamma_{ab}}{\sqrt{N_{\text{rec}}}}(1 - \gamma_{ab}^2), \tag{2.18}$$

  where γ_{ab}^2 is calculated using (2.10). The relative uncertainty, $E[\gamma_{ab}^2]$ is then calculated by

  $$E[\gamma_{ab}^2] = \frac{\epsilon[\gamma_{ab}^2]}{\gamma_{ab}^2}. \tag{2.19}$$

  Noted that this quantity is frequency-dependent.

- Mean estimator of $\overline{U}$

  The mean velocity at each individual measurement location is calculated using (2.2).

The uncertainty estimation of that measurement is:

$$\epsilon[\overline{U}] = \frac{2\sqrt{\sum_{i=1}^{N}(U_i - \overline{U})^2}}{N}, \tag{2.20}$$

where U_i is the discrete data measurement at each time step, and N is the total number of samples. The relative uncertainty, $E[\overline{U}]$, is then calculated by

$$E[\overline{U}] = \frac{\epsilon[\overline{U}]}{\overline{U}}. \tag{2.21}$$

- Root-mean-square estimator of U_{rms}

  The root-mean-square of the velocity at each individual measurement location is calculated using (2.4). The uncertainty estimation of that measurement is:

$$\epsilon[U_{\mathrm{rms}}] = \frac{\sqrt{2}\sqrt{U_{\mathrm{rms}}}}{\sqrt{N}}. \tag{2.22}$$

  The relative uncertainty, $E[U_{\mathrm{rms}}]$, is then calculated by

$$E[U_{\mathrm{rms}}] = \frac{\epsilon[U_{\mathrm{rms}}]}{U_{\mathrm{rms}}}. \tag{2.23}$$

2.5.2 Estimation of representative uncertainty values

As detailed in the previous section, the uncertainty percentage for PSD measurements is the same at all analyzed frequencies and depends solely dependent on N_{rec}. For the microphone measurements at BTU and UNSW, the power-spectral-density uncertainty values are low, 8.9% and 6.3%, respectively. The uncertainty of the spectrum of velocity fluctuations measured by the hot-wire setup is significantly higher, at 26%, due to the lower N_{rec}. This high uncertainty is not a practical concern, due to the logarithmic nature in which the spectra are presented. For example, this level of uncertainty leads to a difference of ±1 dB at -30 dB. The same can be said for the uncertainty value of 16% and for the microphone cross-spectral density in WTC-1, which is also approximately ±1 dB at 5 kHz between the center arc microphone and its neighbor during a test of the nonporous plate at $U = 30$ m/s. The uncertainty of the microphone cross-spectral density for WTC-2 is 13% at 1 kHz as measured by two neighboring microphones during the nonporous edge test at $U = 35$ m/s. The uncertainty estimation of the magnitude-squared coherence of the microphones onboard the remote-controlled glider is 14% and measured during the time period presented in figure 5.1b. Lastly, the uncertainty of the mean velocity and velocity RMS are both less than 1%. Further details about these uncertainty quantities from the microphone and hot-wire velocity measurements are presented in table 2.4.

Table 2.4: Sample uncertainties of measured data presented in §§3, 4, and 5

Device	Calculation type	Facility	F_s, Hz	N	N_{rec}	β	Uncertainty, %
Mic.	Noise spectrum (PSD)	BTU	51,200	2,048,000	499	0.5	8.9
Mic.	Noise spectrum (PSD)	UNSW	65,536	2,097,152	1,023	0.5	6.3
Mic.	Cross-spec. matrix (CSM)	BTU	51,200	2,048,000	499	0.5	16
Mic.	Cross-spec. matrix (CSM)	UNSW	65,536	2,097,152	1,023	0.5	13
Hot-wire	Mean velocity (Mean)	BTU	25,600	256,000	-	-	3.8×10^{-3}
Hot-wire	Vel. fluct. (RMS)	BTU	25,600	256,000	-	-	2.8×10^{-1}
Hot-wire	Vel. fluct. spec. (PSD)	BTU	25,600	256,000	61	0.5	26
Mic.	Noise spectrum (PSD)	Glider	25,000	250,000	485	0.75	9.1
Mic.	Mag.-squared coherence	Glider	25,000	250,000	485	0.75	14
Pitot	Mean velocity (Mean)	Glider	25,000	225,000	-	-	4.3×10^{-2}

Chapter 3

Acoustic wind-tunnel measurements of porous and nonporous test plates and edges

This chapter presents and discusses results from acoustic measurements conducted in WTC-1 and WTC-2 in the BTU and UNSW anechoic wind tunnels respectively. First, results from the WTC-1 plates and WTC-2 flat plate extensions with blunt TEs are discussed, where in the latter, spanwise varying pore distributions are investigated for their ability to reduce bluntness noise. Lastly, results from WTC-1 plates with sharp TEs are presented, where effects of changing the percentage of porous chord, angle of attack, and hole fillets are investigated.

3.1 WTC-1: Flat plates with blunt edges

3.1.1 Acoustic spectra and beamforming soundmaps

This section presents and discusses results for the impermeable reference plate and the perforated plates described in table 2.1 and shown in figure 2.1. Figure 3.1 plots the acoustic spectra as a function of dimensionless frequency (Strouhal number), as measured

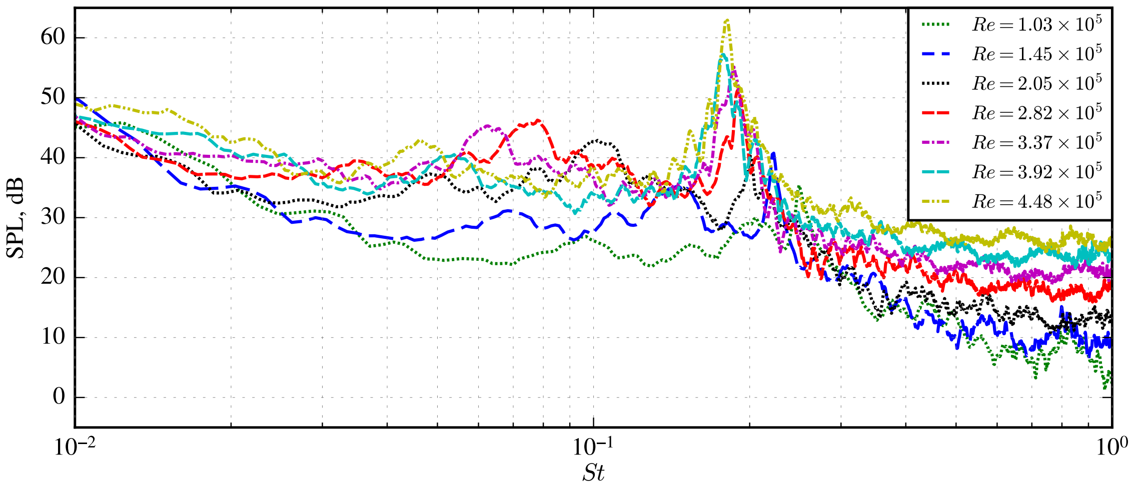

Figure 3.1: Dependence of SPL on the edge-thickness based Strouhal number, St, for the blunt-TE nonporous plate at all tested Reynolds numbers.

from the radially-spaced microphone located 90° to the flow direction (see figure 2.6) for the impermeable plate at all flow speeds. The Strouhal number, St, is calculated using

$$St = \frac{fw}{U}, \tag{3.1}$$

where $w = 3$ mm is the plate thickness.

In general, these sound pressure level (SPL) spectra increase in magnitude with increasing velocity (Reynolds number, Re) and have sharp tonal peaks at the bluntness-induced, vortex-shedding Strouhal number. Looking to figure 3.1, the place where the peaks occur is referred to as St_{b}, or the Strouhal number of bluntness vortex shedding, and these values span $0.18 < St_{\mathrm{b}} < 0.25$. The variation of St_{b} with Re is shown in figure 3.2. With the exception of the lowest Re case, the range of St_{b} is similar to findings from [44, 59] and fall within the range of $0.12 < St < 0.22$ found in Vathylakis et al. [19], which is denoted by the dashed horizontal lines. In addition to this comparison of St_{b} with those found in other experimental works, the bluntness noise peak was also predicted in the same third-octave band using an analytical model [2] not shown here. A small outlier in the data is the St_{b} peak in the spectra recorded at $Re = 2.05 \times 10^5$, where the peak amplitude is slightly lower

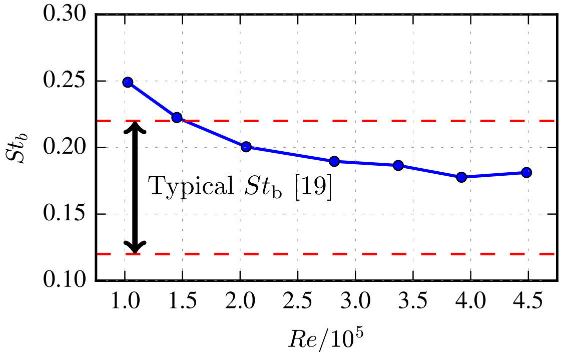

Figure 3.2: Dependence of bluntness-induced vortex shedding Strouhal number, St_b, on Reynolds number (Re) for the nonporous plate.

than expected as it is nearly the same height as that recorded at $Re = 1.45 \times 10^5$. This was seen over multiple test days and it is thought to be the result of an unknown physical mechanism of the tunnel.

To examine how the porous plates affect the acoustic spectra, including the bluntness-induced vortex shedding peak, figure 3.3 plots the sound pressure spectra in third-octave bands recorded by the 90° microphone on the microphone arc as a function of Strouhal number at a selected Reynolds number, $Re = 3.37 \times 10^5$, for the low, medium, and high-porosity groupings of plates, which are compared against the background noise (BG) of the empty tunnel and nonporous plate (NP) for reference. Each grouping of plates has a similar δf value (see table 2.1), and the number of each plate refers to the following hole shapes and spacings: a 1 indicates circular holes aligned in the flow direction, a 2 indicates circular holes staggered in the flow direction, a 3 indicates square holes aligned in the flow direction, and a 4 indicates square holes staggered in the flow direction (see figure 2.1). An increase in the open-area fraction α_h and therefore dimensionless porosity parameter δ leads to greater reductions of the bluntness noise peak. Within these spectra are three main areas of interest: $0.02 < St < St_\mathrm{b}$, where the porous plates reduce broadband noise; at $St = St_\mathrm{b}$ where the porous plates greatly reduce the bluntness-induced vortex shedding tonal noise; and $St > St_\mathrm{b}$, where the porous plates produce excess noise. Within the low Strouhal number range of $0.02 < St < St_\mathrm{b}$, the porous plates can reduce third-octave band

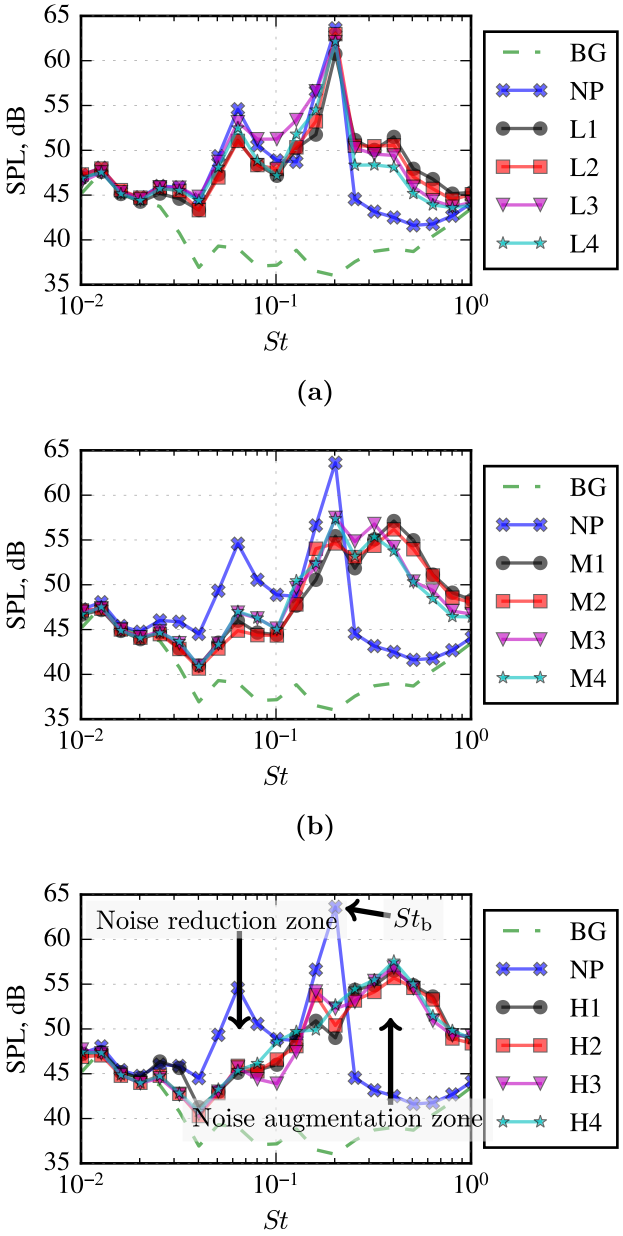

(a)

(b)

(c)

Figure 3.3: Dependence of sound pressure level on Strouhal number at $Re = 3.37 \times 10^5$ for (a) low, (b) medium, and (c) high porosity blunt-edged plates.

SPLs up to 10 dB (see figure 3.3c). In addition, SPL of the third-octave band that contains the St_b can be reduced by up to 16 dB. These reductions come at a cost, as an increase in porosity leads to an increase in excess noise at $St > St_\mathrm{b}$. High-frequency excess noise has been noted in many other experimental investigations of porous edges [14, 42, 60], as well as in simulations of porous [58] and dimpled edges [88]. The ability of the porous plates to attenuate low-frequency and bluntness noise diminishes as the porosity parameter decreases. The low-porosity plates in figure 3.3a have only a modest effect on the low-frequency noise and reduce the bluntness noise peak by approximately 2 dB. The results for the medium-porosity plates in figure 3.3b lie between those of the low- and high-porosity plates. The trend whereby porosity reduces low-frequency noise below the St_{b} but increases high-frequency noise beyond the St_{b} is seen at all flow speeds.

Beamforming results, in tandem with the raw spectra, help to make sense of the acoustic effects of the perforated plates. Figure 3.4 show soundmaps calculated using the delay-and-sum beamforming algorithm at $Re = 3.37 \times 10^5$, the same Re as is presented in figure 3.3, of the nonporous plate (NP) and the highly porous plate (H1) at Strouhal numbers within the three aforementioned areas of interest: low Strouhal number broadband noise reduction, bluntness-induced vortex shedding tonal noise reduction, and excess high Strouhal number noise. Within figure 3.4, the test plate (—), sideplates (—), and nozzle (—) are labeled accordingly, and the flow direction is left to right.

Figure 3.4c illustrates that the source region of the bluntness noise of the nonporous plate is along the trailing edge. The high-porosity plates in figure 3.3c are successful at reducing the low-frequency noise below the frequency of the tonal noise peak (see soundmaps in figure 3.4a and figure 3.4b) and can reduce the magnitude of the peak sound source by up to 10 dB (see soundmaps in figure 3.4c and figure 3.4d). Note that the spatial resolution of DAS is poor at $St = 0.075$ [86]; therefore, the soundmaps in figure 3.4a and figure 3.4b should only be used to compare the magnitudes of the low-frequency noise reduction by the porous plate. Again, these reductions come at the cost of an increase in high-frequency noise at frequencies greater than the bluntness noise peak (see soundmaps in figure 3.4e and figure 3.4f).

Different pore geometries have a noticeable effect on the noise spectra, as well. In general, among the porosity designs considered, the plates with circular perforations are

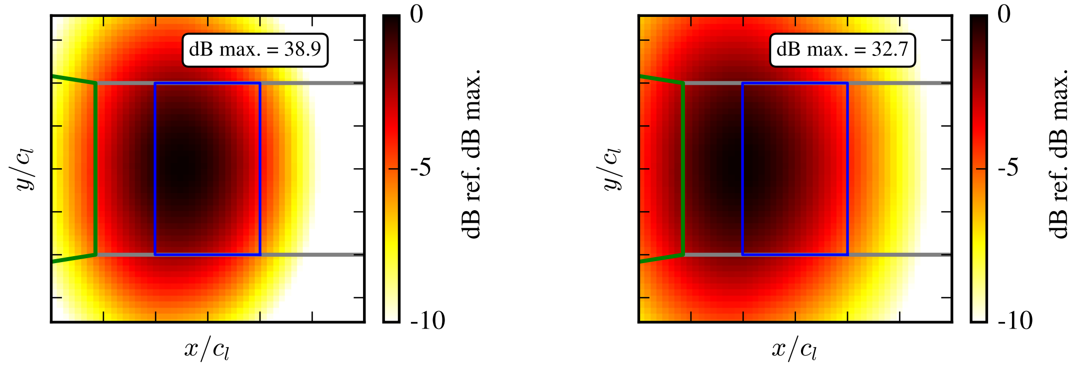

(a) Nonporous, $St = 0.075$ **(b)** H1, $St = 0.075$

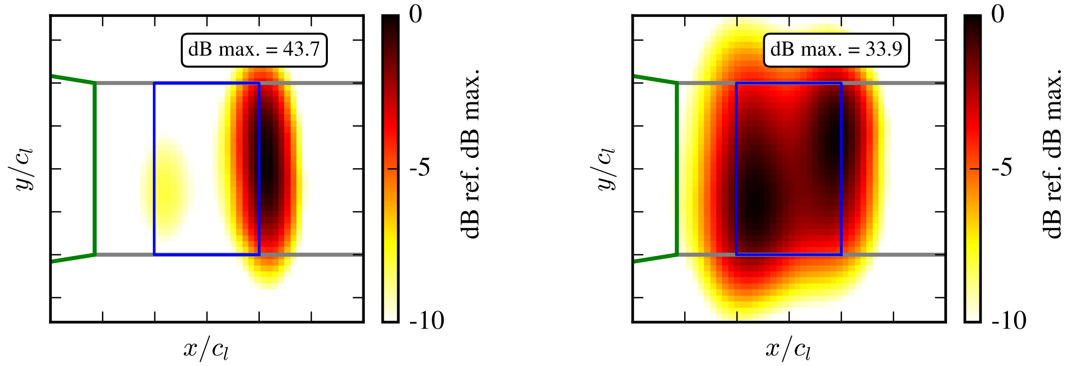

(c) Nonporous, $St = 0.187$ **(d)** H1, $St = 0.187$

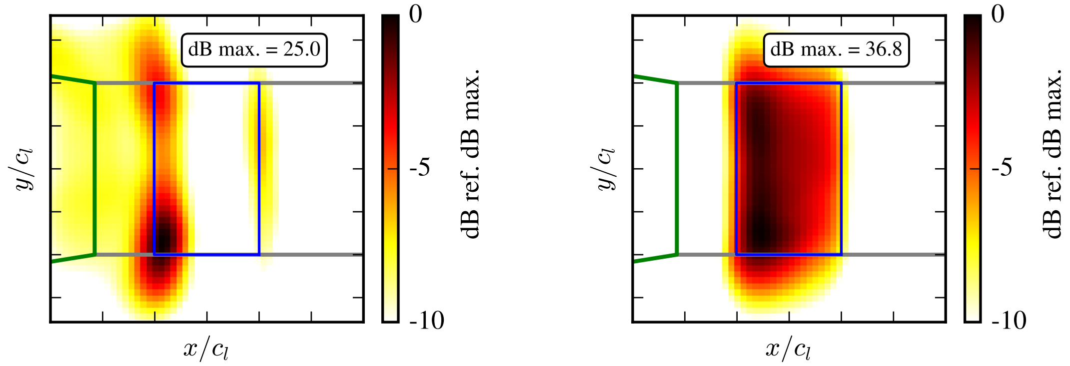

(e) Nonporous, $St = 0.400$ **(f)** H1, $St = 0.400$

Figure 3.4: Beamforming results for nonporous (left) and H1 porous (right) test plates at different third-octave bands centered on multiple Strouhal numbers at $Re = 3.37 \times 10^5$.

more successful at reducing the bluntness noise peak (up to 16 dB). For the high porosity set, the plates with square holes (H3, H4) reduce lower-frequency noise (up to 10 dB) slightly better than those with the circular pores (H1, H2), but this trend is reversed at Strouhal numbers greater than 0.2 (see figure 3.3c). The opposite is true for the medium and low-porosity plates, where the circular pores produce the greatest low-frequency noise reductions but also produce more high-frequency noise (see figures 3.3a and 3.3b). It was hypothesized in this study that offsetting the holes such that there is a greater distance between the holes along the flow direction (plates L2, M2, H2, L4, M4, and H4) may reduce roughness noise due to characteristic streamwise separation length. However, no meaningful differences in the magnitude of the acoustic spectra are found between the plates with either aligned or offset holes with the same value of the porosity parameter δ.

Figures 3.5 and 3.6 summarize how the Strouhal number of the bluntness vortex shedding peak changes as a function of the Reynolds number and design and how the different designs reduce the sound pressure level of the tonal peak. In general, figure 3.5 indicates an inverse trend of the bluntness-peak Strouhal number and Reynolds number for the porous plates considered. While the L1 plate has the highest St_{b} at all velocities and the medium-porosity plates yield a higher St_{b} than that of the nonporous plates, in general, it is challenging to discern a trend that describes the relationship between pore shape and bluntness peak within the same porosity group. Note that in figure 3.5 the highly-porous plates have an St_{b} close to that of the nonporous plate as the bluntness peaks for these cases are virtually eliminated. The significant reduction in bluntness noise at high Reynolds numbers has a positive outlook for the applications of this work, where modern bluntness applications of flow noise reduction technologies, e.g., wind turbines, operate at higher Reynolds numbers [89] and may generate bluntness noise [90] in limited settings.

Figure 3.6 displays the amplitude of the bluntness-induced vortex-shedding peak generated by each plate across all tested Reynolds numbers. In general, an increase in the porosity parameter is accompanied by a reduction of the bluntness noise; the maximum decrease in tonal noise occurs for plate H1 at $Re = 2.82 \times 10^5$ with an attenuation of 17 dB.

Notable deviations in this overall trend occur at $Re = 2.02 \times 10^5$, where some of the low-porosity plates increase the noise at the bluntness peak. This effect may be explained by the relatively low initial amplitude at the St_b peak of the nonporous plate at this Reynolds number, as shown in figure 3.1. For qualitative comparison, figure 3.6 includes the U^5 and U^6 trends of the acoustic intensity scaling on flow speed, in the form of dashed lines, that are expected from the scaling of turbulence sources scattered by either an impermeable [11] or highly-porous edge [12, 15], respectively. The bluntness noise levels do not trend with these theoretical scattering predictions at lower Reynolds numbers. However, these data begin to approach the acoustic scattering trends at higher values of Reynolds number. It is important to note that the creation of tonal noise due to vortex shedding is a different physical mechanism than the trailing-edge scattering mechanism for which these scaling relationships were determined. These observations suggest a focused study that is beyond the scope of the present work to reconcile the possible interaction of the vortex-shedding and acoustics scattering noise mechanisms as a function of the Reynolds number.

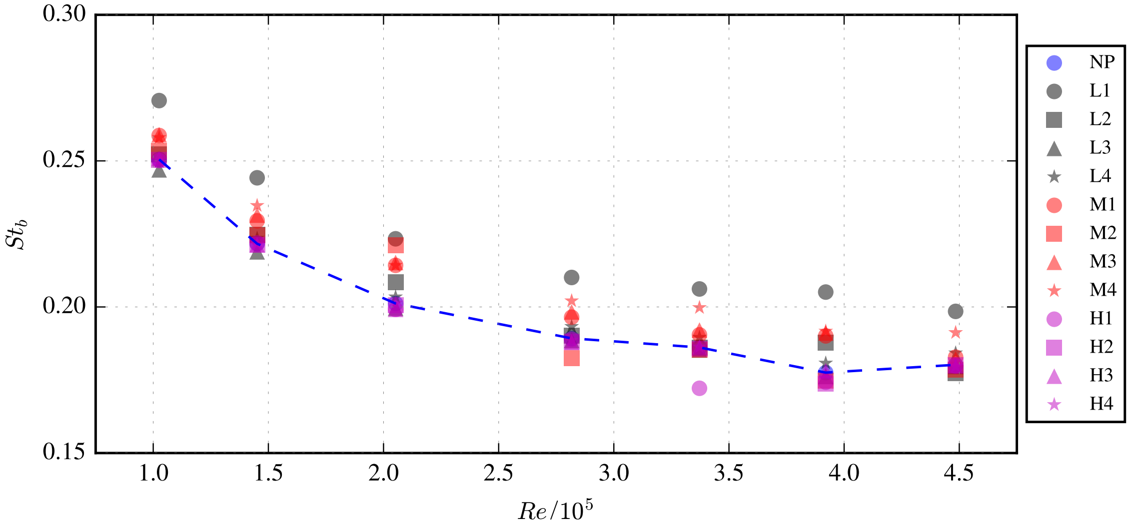

Figure 3.5: Dependence of the bluntness-induced vortex shedding peak Strouhal number, St_b, on Reynolds number, Re, for all plates and flow speeds. Note the nonporous (NP) points are connected by a dashed blue line.

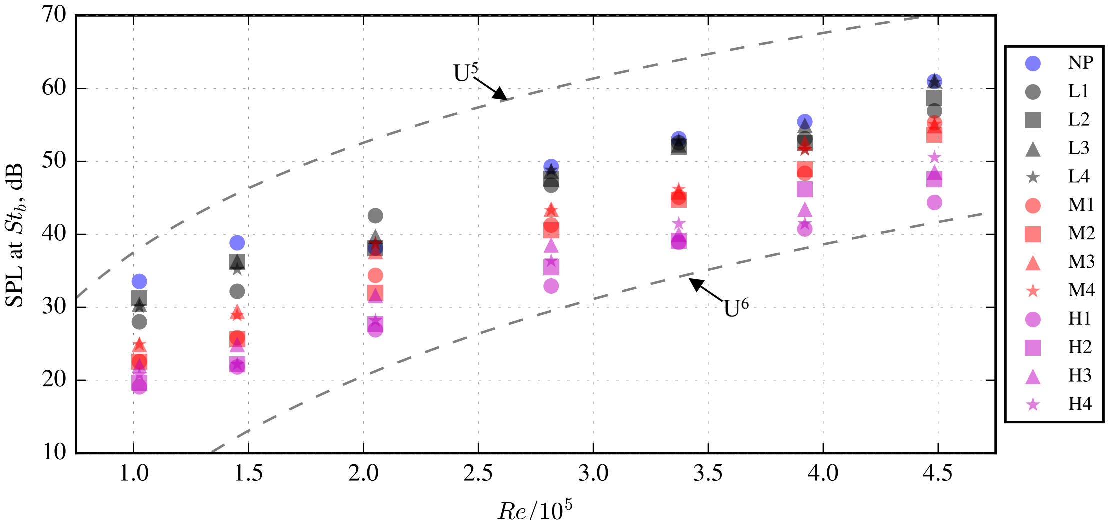

Figure 3.6: SPL at St_b as a function of Re for all plates and flow speeds.

3.1.2 Changes to overall sound pressure levels (OSPLs) and directivity

In addition to the effect of the different porosities on the far-field noise spectra, their effect on the total noise is also analyzed. This analysis is carried out by evaluating the changes to the overall sound pressure level (OSPL) using (2.9). Figure 3.7 plots the OSPL results as a function of Reynolds number Re for each grouping of the porous plates compared to the background noise (BG) of the tunnel and the nonporous plate (NP), as measured by the center microphone. The maximum reduction in OSPL due to porosity is approximately 3 dB for plates H1 and H2. This relatively small reduction in OSPL is due to the porous plate creating excess roughness noise at high frequencies. While plates H1 and H2 (with circular pores) are the most successful of the high-porosity grouping, the overall performance of the plates in the medium- and low-porosity groupings vary greatly with hole geometry and Re, as M4 performed slightly better than M2 at high velocities. However, this ordering is the opposite at lower velocities.

This trend of slight reductions in noise can be further visualized by polar plots of OSPL calculated at all eleven radially-spaced microphone locations. Figure 3.8 shows the OSPL for the reference plate and porous plates L2, M2, and H2 at different Re. These plates are chosen as they slightly perform better at reducing the vortex-shedding peak than the other

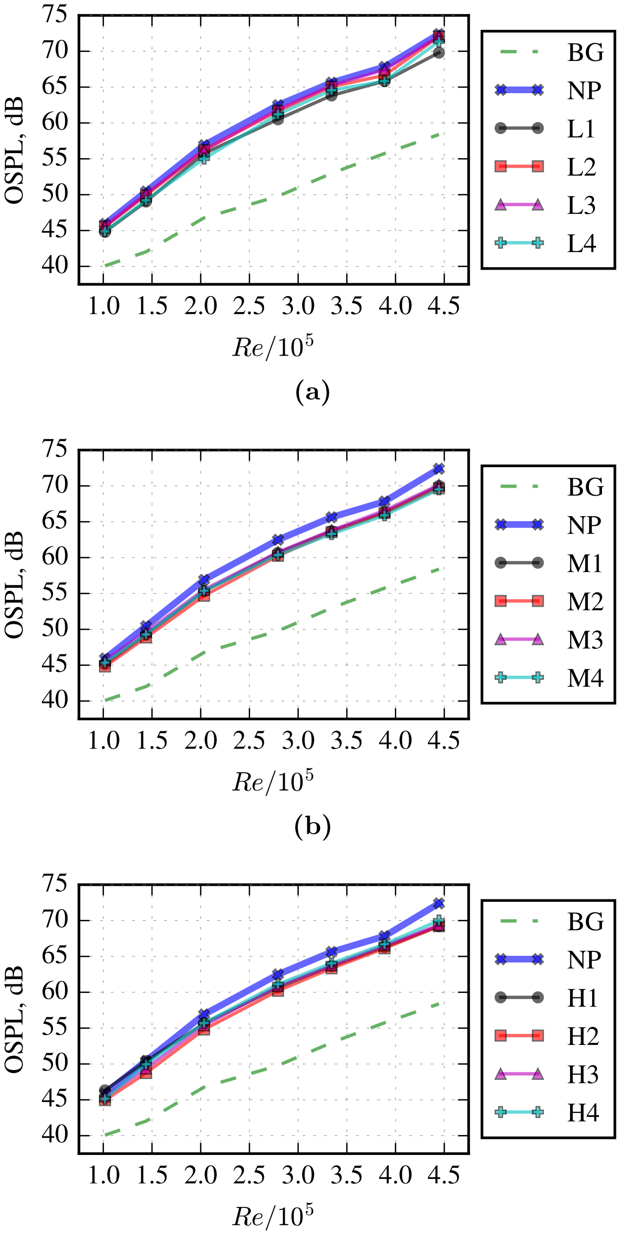

(a)

(b)

(c)

Figure 3.7: Dependence of OSPL on *Re* for (a) low, (b) medium, and (c) high-porosity plates.

plates in their grouping. The porous plates M2 and H2 are able to reduce the OSPL at nearly all measured angles and flow speeds (see figure 3.8). However, the ability of plate L2 to decrease OSPLs depends on the flow speed and microphone number. At $Re = 1.03\times10^5$, the measured OSPLs from each plate were nearly identical. At the remaining higher velocities, the L2 plate was nearly the same level as the impermeable, and the levels of the M2 and H2 plate were nearly identical and just slightly lower than those of the impermeable plate. On average, at $Re = 4.48 \times 10^5$, the M2 and H2 (higher α_h) plates achieved an OSPL reduction of up to 3 dB. A comparison between the acoustic spectra trends in figure 3.3 and the OSPL data in figure 3.7 highlights how low-frequency and bluntness noise reductions within $St \leq St_\mathrm{b}$ are largely offset by the noise in excess noise at $St > St_\mathrm{b}$. Furthermore, a qualitative change in the directivity pattern occurs as the Reynolds number and porosity parameter increase, which is examined next in greater detail in the three Strouhal number regimes. Figure 3.9 displays the directivity of sound generated by the nonporous plate and select porous plates at three key Strouhal numbers for $Re = 3.37 \times 10^5$. Figure 3.9a displays the SPL at each of the arc-microphones for $St = 0.075$, a Strouhal number where all of the plates tested reduce broadband noise. In general, an increase in porosity parameter through an increase in the open-area fraction α_h leads to an increase in noise reduction. Figure 3.9b displays the directivity at the bluntness noise peak, $St = 0.187$, and clearly illustrates how increasing porosity, from plates L2, to M2 and H2, leads to an increased reduction of the bluntness noise peak. At $St = 0.187$, there is a slight trend towards a dipole directivity shaped when compared to the results at $St = 0.0750$. Lastly, figure 3.9c displays the directivity of sound at a relatively high Strouhal number, $St = 0.400$. With an increase in α_h, an increase in noise is seen at each of the microphones. Within the range of $St > St_\mathrm{b}$, the high-frequency excess noise dominates the acoustic spectra of the porous plates.

3.1.3 Summary

An experimental program was carried out to evaluate trailing-edge bluntness noise and its overall reduction using perforated plates. The plates were designed with pore geometries and spacings to fit three groups of a dimensionless porosity parameter δ, and results of the far-field sound pressure level spectra and the overall sound pressure level for various

Reynolds numbers were presented. Bluntness vortex shedding noise is present between $0.17 < St_{\mathrm{b}} < 0.25$, and the highest porosity plates can reduce this noise by up to 16 dB, effectively removing the associated tonal peak from the acoustic spectra. The relationship between hole shape and spatial arrangement with the noise spectra is complex, where the plates with circular holes are slightly more effective at reducing the bluntness noise peak. However, the plates with holes along the flow direction attenuate low-frequency noise slightly better than plates with staggered hole placement at most flow speeds. An increase in open-area fraction α_h (and consequently, the dimensionless porosity parameter δ), regardless of shape or pore alignment with the flow, leads to an increase in high-frequency noise due to the many surface elements (i.e., holes or pores) acting as noise sources. Directivity plots of the sound pressure level at a low Strouhal number where broadband noise is reduced by porosity, the bluntness noise peak Strouhal number, and a high Strouhal number where excess noise is created by porosity show a trend towards the anticipated dipolar shape with increasing porosity parameter.

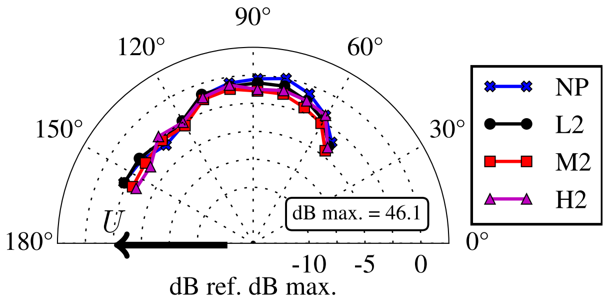

(a) $Re = 1.03 \times 10^5$

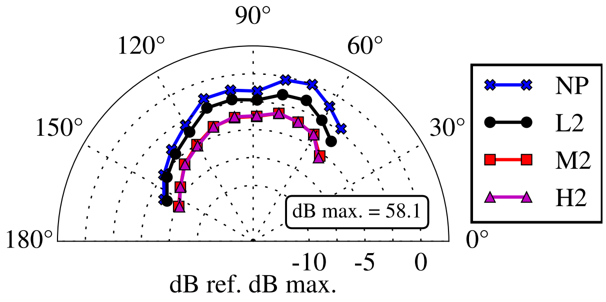

(b) $Re = 2.05 \times 10^5$

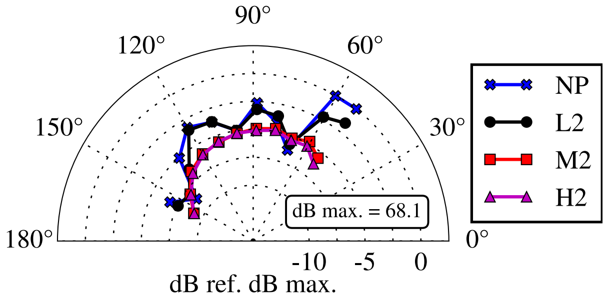

(c) $Re = 3.37 \times 10^5$

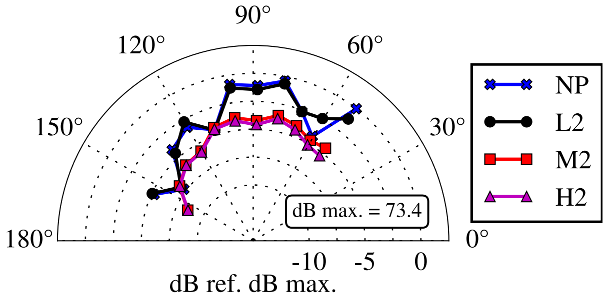

(d) $Re = 4.48 \times 10^5$

Figure 3.8: OSPLs measured at each radially-spaced microphone (see figure 2.6) for various porosity treatments at different Reynolds numbers.

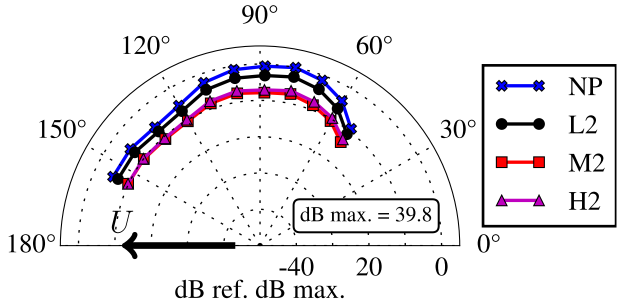

(a) $St < St_\mathrm{b}$

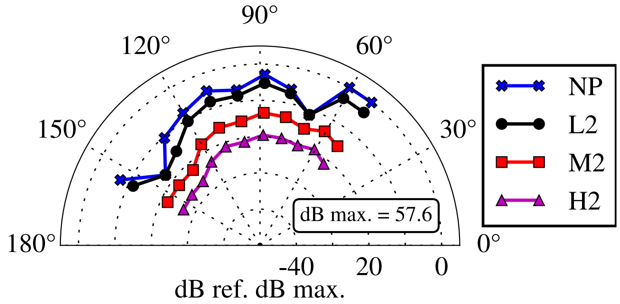

(b) $St = St_\mathrm{b}$

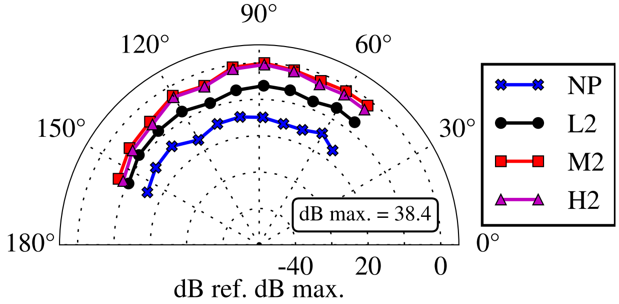

(c) $St > St_\mathrm{b}$

Figure 3.9: Directivity of sound generated by nonporous plates and select porous plates at (a) $St = 0.0750$, (b) $St = St_\mathrm{b} = 0.187$, and (c) $St = 0.400$ at $Re = 3.37 \times 10^5$.

3.2 WTC-2: NACA 0012 airfoil with blunt porous extensions

Porous flat plate TE extensions with spanwise varying pore spacings are investigated for their ability to reduce flow noise. Acoustic spectra of the nonporous and porous plates are calculated using a single microphone at the center of the acoustic array. Results for the sound pressure level (SPL, dB ref. $20\,\mu\text{Pa}$) generated by the nonporous reference edge at all tested velocities are shown in figure 3.10. The acoustic spectra are shown in both the frequency and Strouhal number (St) domain, where St is calculated using (3.1) and $w = 1.6$ mm.

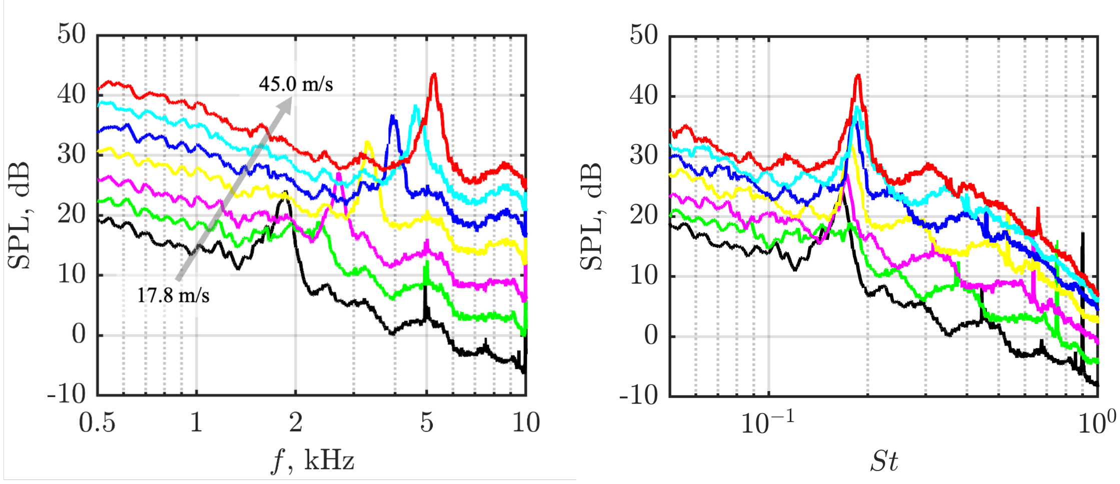

(a) **(b)**

Figure 3.10: Dependence of SPL for the nonporous reference edge on (a) frequency and (b) St for all tested flow velocities: $U = \{17.8, 21.3, 25.1, 30.0, 34.9, 39.9, 45.0\}$ m/s.

These results indicate a general increase in SPL magnitude with an increase in velocity, as expected. Tonal peaks in figure 3.10b indicate vortex shedding noise at the bluntness peak, St_b, of $0.168 < St_\text{b} < 0.187$. This tonal peak increases modestly with flow speed, reaching the maximum value of $St_\text{b} = 0.187$ at $U = 40$ m/s. This behavior is depicted in figure 3.11, where the bounds of the vertical axis are the limits at which bluntness-induced vortex shedding typically occurs [19].

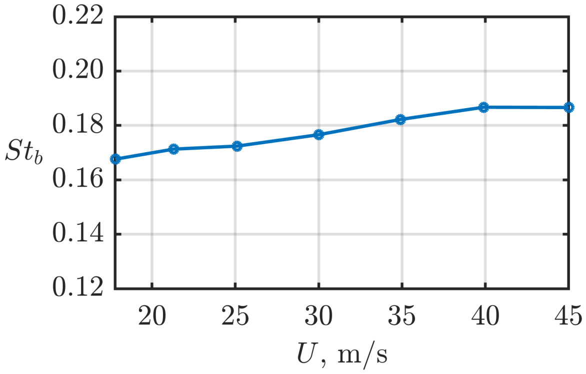

Figure 3.11: Dependence of bluntness shedding peak St_b on flow speed for NACA 0012 airfoil with nonporous edge extension.

3.2.1 Acoustic spectra

Figure 3.12 shows compares sound pressure level spectra as a function of Strouhal number for the three groups of plates at a select velocity, $U = 34.9$ m/s. Results at this velocity are highlighted because the highest reduction of bluntness noise is observed for this condition, and all porous plates (i.e., the a-series, b-series, and c-series) successfully reduce the bluntness noise peak. The c-series plates, which also have the highest δf, reduce this peak the most. Contrary to other experimental investigations with a partially-porous chord [14], not all plates reduce broadband noise by significant levels in the range of $0.05 < St < 0.17$, i.e., Strouhal numbers below the vortex shedding peak. However, at all tested velocities, every porous plate produces a notable level of excess noise at Strouhal numbers higher than the bluntness tonal peak. This result is consistent with findings from Kershner et al. [91, 92], where the tonal peak is the transition frequency beyond which the porous plates created excess noise. This excess noise is seen in the form of tonal humps, and it is hypothesized that these tonal humps may be related to a resonance phenomenon related to the bluntness-induced tonal peaks, which is supported by the beamforming analysis in §3.2.2. The a-series and b-series plates increase the magnitude of the first and second tonal humps the largest (up to 8 dB and 13 dB respectively). The c-series plates increase the noise at the first and second humps the least (up to 4 dB and 12 dB respectively). This could be due to the c-series plates having the highest δ, which suppress the main tonal peak the most and increase the subsequent tonal peaks the least. Therefore, the c-series are the most successful plates.

At this *Re* presented, the tonal humps feature local minima that occur around $St \approx 0.30$ and $St \approx 0.54$. These Strouhal numbers match those associated with wavelengths relative to the size of the porous section. For example, the porous extension is 0.05 m in length, which if taken as the wavelength of a sound wave, would correspond to a frequency of 6.86 kHz or $St = 0.31$. It is therefore suggested that the tonal hump minima occurring after the bluntness peak could be related to a possible destructive interference mechanism caused by the porous edge itself.

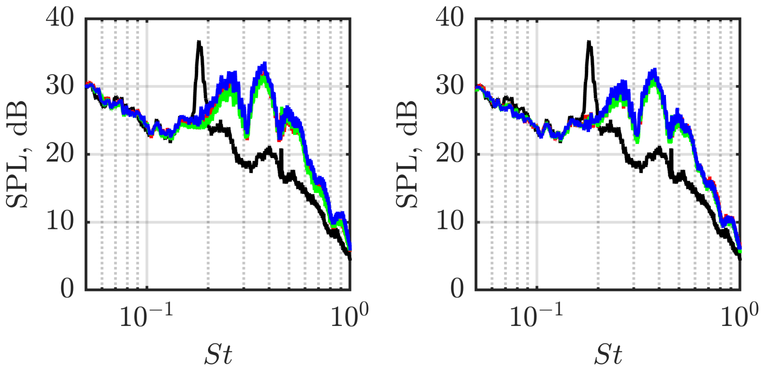

(a) a-series **(b)** b-series

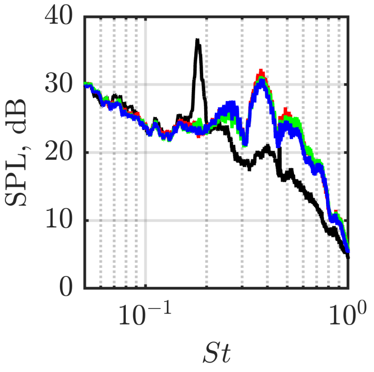

(c) c-series

Figure 3.12: Dependence of SPL on Strouhal number (St) at $U = 34.9$ m/s for each group of edges (Reference —, X|1 —, X|2 —, and X|3 —). Note the red lines are covered by the blut and green lines at most frequencies.

The following figure 3.13 tabulates the maximum reductions of the bluntness peak (a) and maximum increase (b) of high-frequency excess noise created by the porous plates. This difference in sound pressure level, ΔSPL, is calculated by the following equation:

$$\Delta\mathrm{SPL} = \mathrm{SPL}_{\mathrm{P}} - \mathrm{SPL}_{\mathrm{NP}}, \tag{3.2}$$

where $\mathrm{SPL}_{\mathrm{P}}$ is the sound pressure level of the porous edge, and $\mathrm{SPL}_{\mathrm{NP}}$ is the sound pressure level of the nonporous edge. Negative values of ΔSPL indicate a relative noise reduction by the porous edge treatment.

As shown in figure 3.13a, all porous plates are successful at reducing the bluntness-induced vortex shedding peak at all velocities at varying degrees. The b-series plates reduce this tonal noise the least, with the a-series and c-series performing relatively better, in that order. With the exception of results measured at the flow speed $U = 21.3$ m/s, where the reduction is much lower than other flow speeds, the relationship between flow speed and SPL reduction varies from case to case, and there is no clear trend linking the two. Just as there is no clear correlation between the SPL reduction by the porous plates with the flow speed, the same is true for the SPL increase at higher frequencies.

Each series of porous plates also greatly increases high-frequency excess noise, beyond the bluntness-shedding peak and this increase is tabulated in figure 3.13b. In general, the c-series plates increase this noise the least, with the a-series and then b-series following in performance by only modest values of Δ SPL. The uncertainty of the measured sound pressure levels (6.3%, see table 2.4) may help to explain the results in figure 3.13. For example, this uncertainty corresponds to ± 0.3 dB at St_{b} for the nonporous and porous edge extensions; consequently, the uncertainty of the ΔSPL is ± 0.6 dB. The difference in decrease and increases in SPL within each series of plates falls well into this range. Therefore, while the uniformly-spaced edges X|1 and randomly-spaced edges X|3 tend to reduce the bluntness noise peak the most at all tested flow speeds within each series, the difference is small and within the margin of uncertainty. With this uncertainty in mind, the c-series plates still perform marginally better than the a-series, which perform marginally better than the b-series. The following section displays beamforming soundmap results to help visualize these acoustic effects of the porous plates, in comparison to the reference.

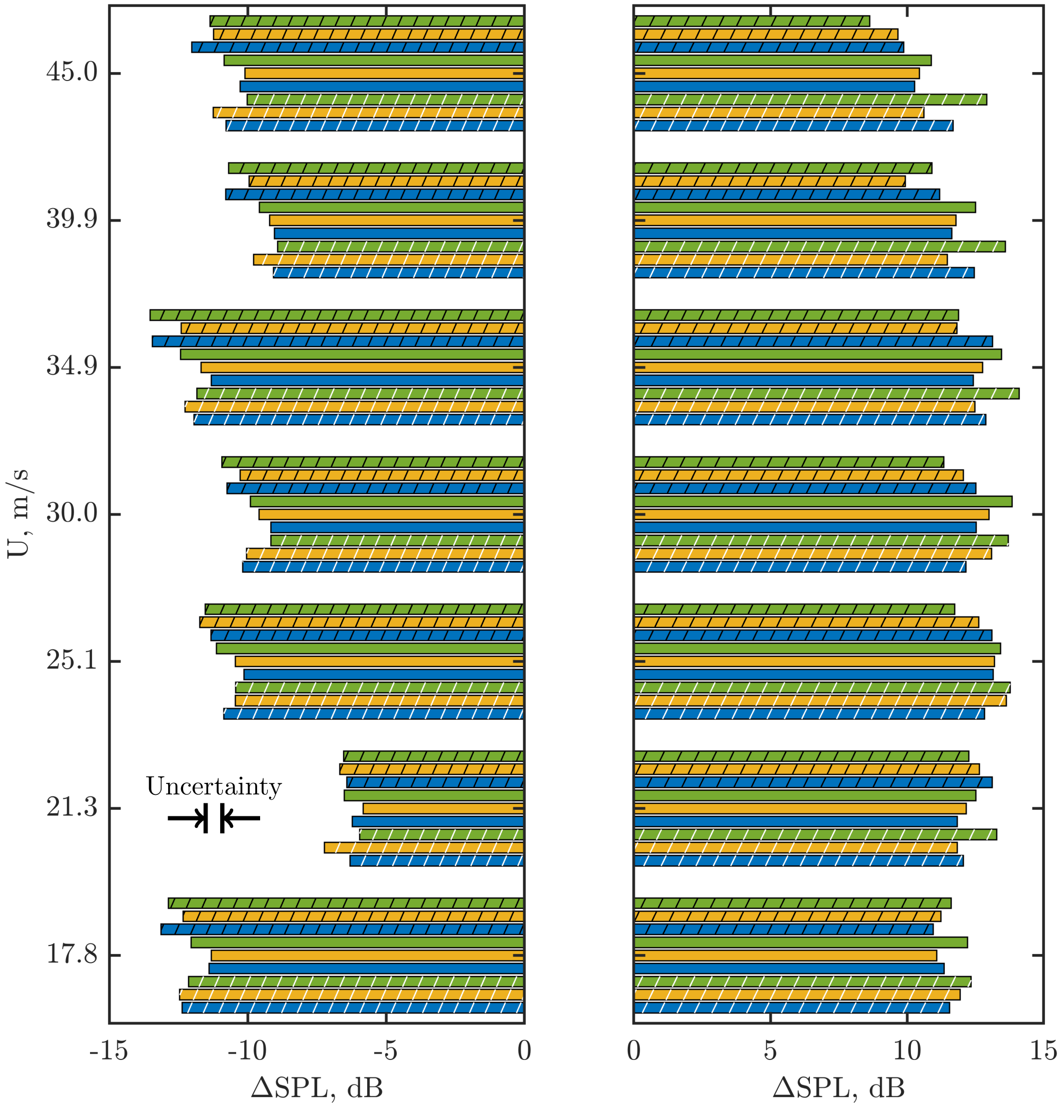

(a) SPL decrease due to porous plate **(b)** SPL increase due to porous plate

Figure 3.13: Maximum (a) decrease of bluntness tonal peak and (b) increase of high-frequency noise (in dB) by all porous plates at all tested velocities. The white cross-hatching signifies the a-series, the bars without hatching the b-series, and the black cross-hatching the b-series. The blue bars represent the X|1 plates, the yellow the X|2 plates, and the green the X|3 plates.

3.2.2 Beamforming soundmaps

Figure 3.14 shows soundmaps at the tonal peak, $St = 0.187$, and two subsequent tonal humps at $St = 0.255$ and $St = 0.380$ for the reference plate and all the best performing porous plates, the c-series, at $U = 34.9$ m/s. Note that the colorbar for each Strouhal number has a different dynamic range. As magnitudes change from one Strouhal number to the next, this change of the dynamic range of the colorbar is to ensure all information for each soundmaps can be effectively displayed. Within each subfigure, a white × designates the location of the highest SPL.

Figure 3.14a shows clearly that the source region of the tonal peak for the reference plate (see figure 3.12) is located along the trailing edge. Figures 3.14b, 3.14c, and 3.14d show that this tone persists when edge porosity is introduced, albeit with a significantly lower amplitude. Figure 3.14e shows that the source of the second tonal hump, at $St = 0.255$, is located also at the trailing edge. The magnitude of this hump, as shown in the spectra in figure 3.12 is 10 dB lower than at the primary vortex shedding tone $St = St_\mathrm{b} = 0.182$. Figures 3.14f, 3.14g, and 3.14h show that the porous plates amplify this noise at their trailing edges, creating high-frequency excess noise in the form of tonal humps. This same trend is seen in the soundmaps comparing the reference plate to the c-series plates at $St = 0.380$ in figures 3.14i, 3.14j, 3.14k, and 3.14l.

In general, the different hole spacings lead to different shapes of the noise generation at the trailing edge as shown in figure 3.14. The soundmaps in figure 3.14a of the reference plate at the fundamental bluntness-induced vortex shedding Strouhal number shows sound sources along the trailing edge clustered in three main lobed regions. The soundmaps of the uniformly spaced plate c|1 show lobed behavior at the two lower Strouhal numbers, while the soundmaps from the optimized plate c|2 show similar lobed behavior but at all Strouhal numbers shown. The soundmaps of plate c|3, which has randomly spaced pores in the spanwise direction, show some lobed behavior at the two lower Strouhal numbers. However, it is not as apparent as in the cases of plates c|1 and c|2. The presence of lobed behavior of maxima for the reference plate and uniformly spaced plate c|1 suggest that bluntness-related noise in this study may have an inherent spanwise correlation. However, when porosity is varied in the spanwise direction, this matter becomes very complicated.

Lastly, the location of highest SPL for the nonporous plate is centered nearly exactly around the mid-span in figure 3.14a. The porous plates change the location of highest SPL, as in indicated by the white ×'s, to above and below mid-span for nearly all porous plates and Strouhal numbers shown.

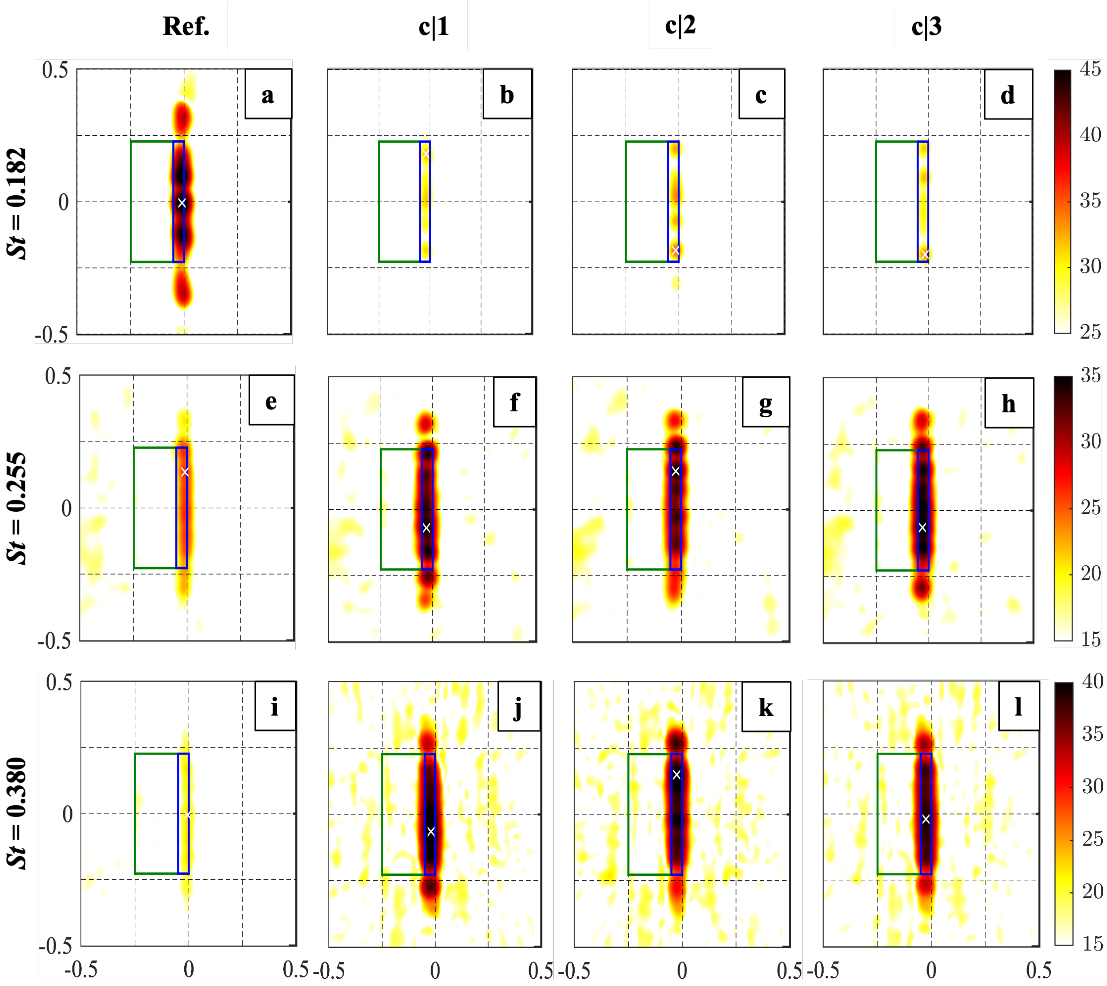

Figure 3.14: Beamforming results at select bluntness-induced vortex shedding Strouhal numbers for reference plate and c-series plates at $U = 34.9$ m/s. All spatial dimensions shown are in meters (m) and colorbar values are in dB ref. 20 μPa. Within each subfigure, a white × marks the spot of highest magnitude. Flow direction from left to right.

3.2.3 Summary

An experimental investigation is conducted into the ability of porous plates with spanwise-varying pore spacings to reduce bluntness-induced vortex-shedding noise. Three series of plates with the follow spacings are tested in an open-jet wind tunnel with a 65 microphone array: uniformly spanwise-spacing, optimized spanwise-spacing, and random spanwise-spacing. Each set of plates is characterized by a nondimensional porosity parameter, δ, multiplied by the frequency of interest, f. SPL comparisons are made between the reference nonporous plate and each porous plate. Each set of plates is successful at eliminating the bluntness-induced vortex-shedding noise, and the plates with the highest δf, the c-series plates reduce the bluntness shedding tonal peak the most (up to 13 dB) and increase the high-frequency excess noise the least. Each set of plates also creates excess noise at higher frequencies, and the c-series plates increase this noise the least. In general, there is no clear correlation between flow speed and SPL changes due to porosity. However, there is a complicated relationship between the hole spacing and noise reduction capabilities. The plates with uniformly- and randomly-spaced holes seem to appear better than those with optimized spanwise spacings. However, the differences are modest and within the uncertainty margins. The resulting acoustic spectra are supported by soundmaps which show the location of the bluntness noise to be located directly at the trailing edge. This fundamental tone is reduced by the porous plates at the trailing edge. However, the high-frequency excess noise is amplified by the porous edges at the trailing edge and the edges with optimized pore spacings created slightly less of this kind of noise. While porosity may be used to target and reduce specific frequencies, it leads to an increase of noise at high frequencies that could lead to higher overall sound pressure levels (OSPLs). These competing effects of bluntness-noise reductions and excess high-frequency noise generation motivate future work to investigate improved porous designs that minimize self-noise.

3.3 WTC-1: Flat plates with sharp edges

3.3.1 Acoustic spectra and beamforming soundmaps

Figure 3.15 presents the noise levels contributed by all beamforming sectors of the nonporous plate, as defined in figure 2.13, at all tested flow speeds compared to the average of the individual microphone SPLs normalized to the center of the array. These set of figures provides a detailed baseline for the acoustics of the nonporous plate, against which the results of the porous plates are compared. The greatest difference between the spectra from the microphone average in figure 3.15a and the spectra integrated from all integration sectors in figure 3.15b exists at velocities $U \leq 25$ m/s at frequencies $f \leq 5$ kHz. This difference results from the fact that noise from the nozzle dominates at these frequencies for the low velocity tests, and the nozzle is not included in the integration sectors. Thus, the resulting integrated spectra using beamforming are lower than that from the microphone average and are a more accurate representation of noise generated from the plate.

3.3.1.1 Fully-porous plate

Figure 3.16 presents the noise levels contributed by all sectors of the porous H1 plate, as defined in figure 2.13, at all tested flow speeds. These data highlight the overall trends of the sample porous plate. In general, as with the blunt-edge plates in §3.1, the SPL increases with an increase in velocity, without the presence of tonal peaks. In addition, the same trends and shape of the spectra are maintained when moving from figure 3.16a, the measurements with the single microphone, to figure 3.16b, the spectra calculated from integrating DAMAS beamforming results across the entire integration area, with the exception of the two lowest tested velocities. The exact cause of these low levels is unknown but might be due to less TBL TE noise due to the low Reynolds number. In addition, figures 3.16c, 3.16d, 3.16e, and 3.16f shows the spectra integrated from the TE, LE, middle, and sideplate regions respectively, as described in figure 2.13. These SPLs recorded from the TE section follow the same trends and have similar shapes to those integrated from the entire integration area, except for at high frequencies at certain low velocities. For $f > 2$ kHz at velocities $U \leq 18.1$, the SPLs drop significantly in value. This outcome could be due to the fact that the boundary layer is less turbulent at the low flow speeds and therefore less TBL TE noise is generated [93]. Also, at the highest tested flow speed ($U = 40$ m/s), the DAMAS beamforming incorrectly locates the source of sound at $f = 500$ Hz to an area outside of the TE. This lack of a $f = 500$ Hz source within the integration area results in the SPL at this frequency being very low and is discussed further in §A.4. In addition, noise from

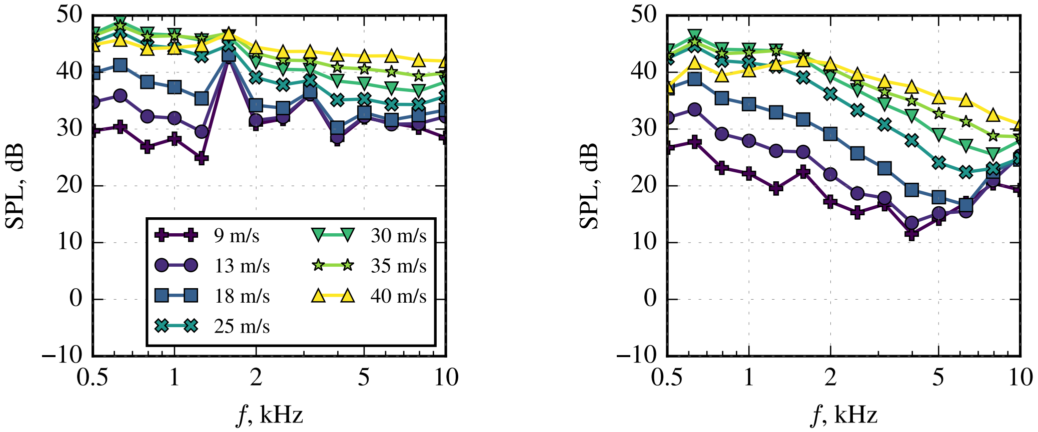

(a) Microphone average

(b) All integration sectors

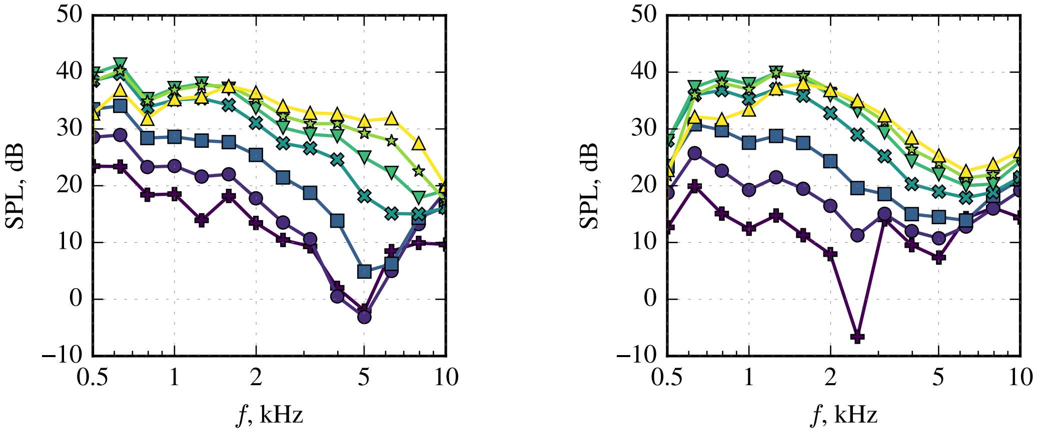

(c) TE integration sector

(d) LE integration sector

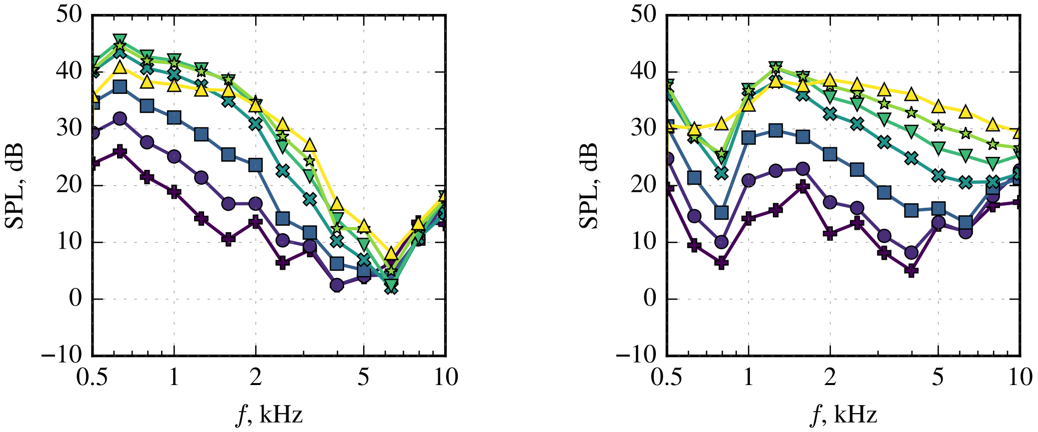

(e) Middle integration sector

(f) Sideplate integration sectors

Figure 3.15: Microphone average SPL compared to SPLs integrated from different regions of the nonporous plate.

the LE, middle part of the plate, and sideplate regions dominate at $f > 2$ kHz at most flow speeds which further supports that idea that beamforming must be used to investigate TE noise as otherwise noise from other sections of the plates can overpower it. The overall good performance of DAMAS for beamforming integration leads to the following sections where noise contributions from different regions of the plates from WTC-1 are analyzed.

Figure 3.17 is the first of a set of figures that illustrates the change in sound pressure levels integrated over the entire area of the porous plates compared to the nonporous plate at all four select flow speeds. The data is presented as ΔSPL against frequency as calculated by (3.2). Figure 3.17 illustrates this change in SPL at the lowest tested flow speed of $U = 9$ m/s. The low-porosity plates, shown in figure 3.17a, reduce noise the least, up to approximately 4 dB at select frequencies. However, they increase noise at most frequencies, up to approximately 6 dB. The medium-porosity plates in figure 3.18b reduce noise up to 10 dB at the lowest frequency, $f = 500$ Hz, but can increase noise up to 14 dB at $f > 2$ kHz. Lastly, the high-porosity plates in figure 3.17c reduce noise up to 15 dB at $f = 500$ Hz and also increase noise up to 16 dB at $f > 2$ kHz. The best overall performing plate at this flow speed, $U = 9$ m/s, is plate H2.

Figure 3.18 illustrates the change in SPL at the flow speed of $U = 18$ m/s. In a similar manner to the results presented for $U = 9$ m/s in figure 3.17, the low-porosity plates do not meaningfully decrease noise in the low-frequency range. The medium- and high-porosity plates reduce low-frequency noise by up to 14 dB and 16 dB respectively; the magnitudes and range across which the decreases occur are larger than at $U = 9$ m/s. On the other hand, compared to the results from $U = 9$ m/s, all sets of porous plates increase high-frequency noise by a larger magnitude at this higher flow speed (up to 18 dB). At this flow speed, all of the L-plates perform similarly to each other; however, plates of the same hole shape within the medium and high porosity groups perform similarly to each other. As in the results presented from $U = 9$ m/s, the best overall performing plate at $U = 18$ m/s for maximizing low-frequency noise reductions and minimizing the high-frequency noise increase is plate H2.

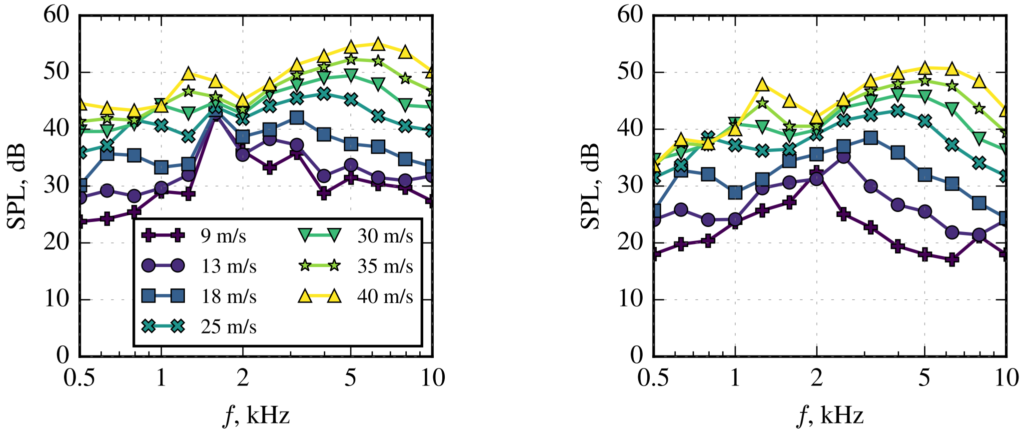

(a) Microphone average **(b)** All integration sectors

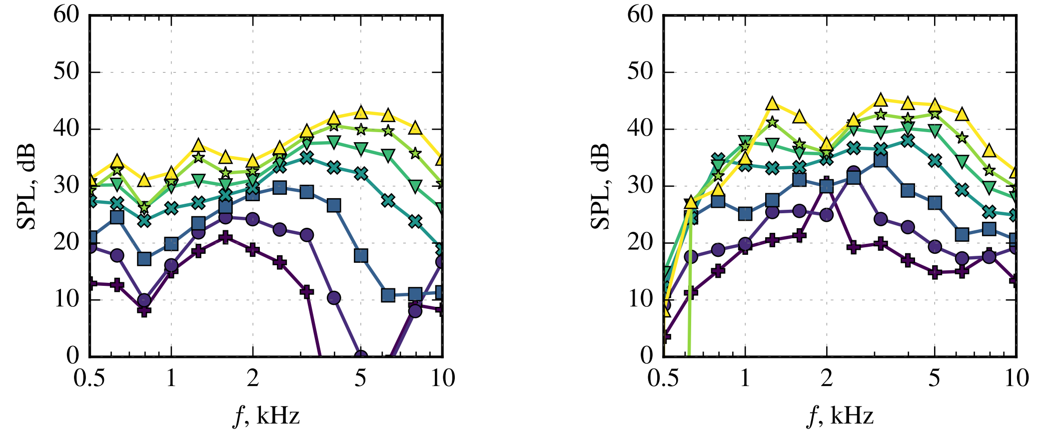

(c) TE integration sector **(d)** LE integration sector

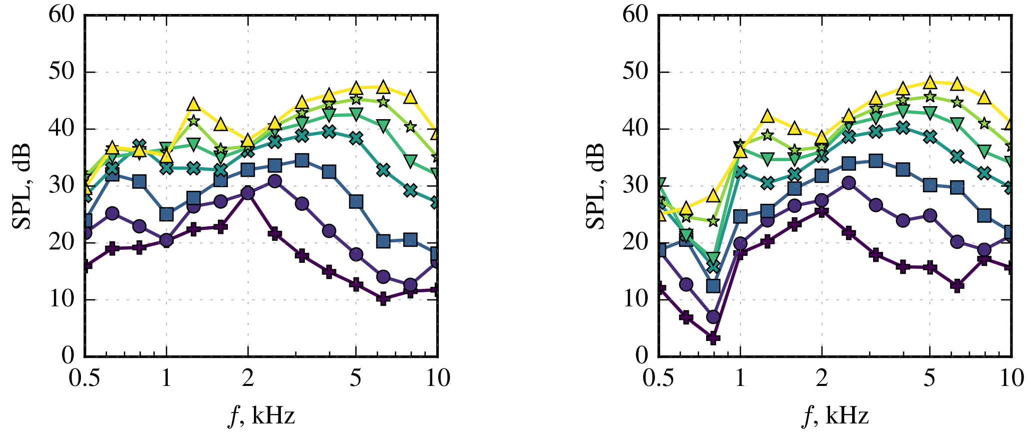

(e) Middle integration sector **(f)** Sideplate integration sector

Figure 3.16: Microphone average SPL compared to SPLs integrated from different regions of the H1 porous plate.

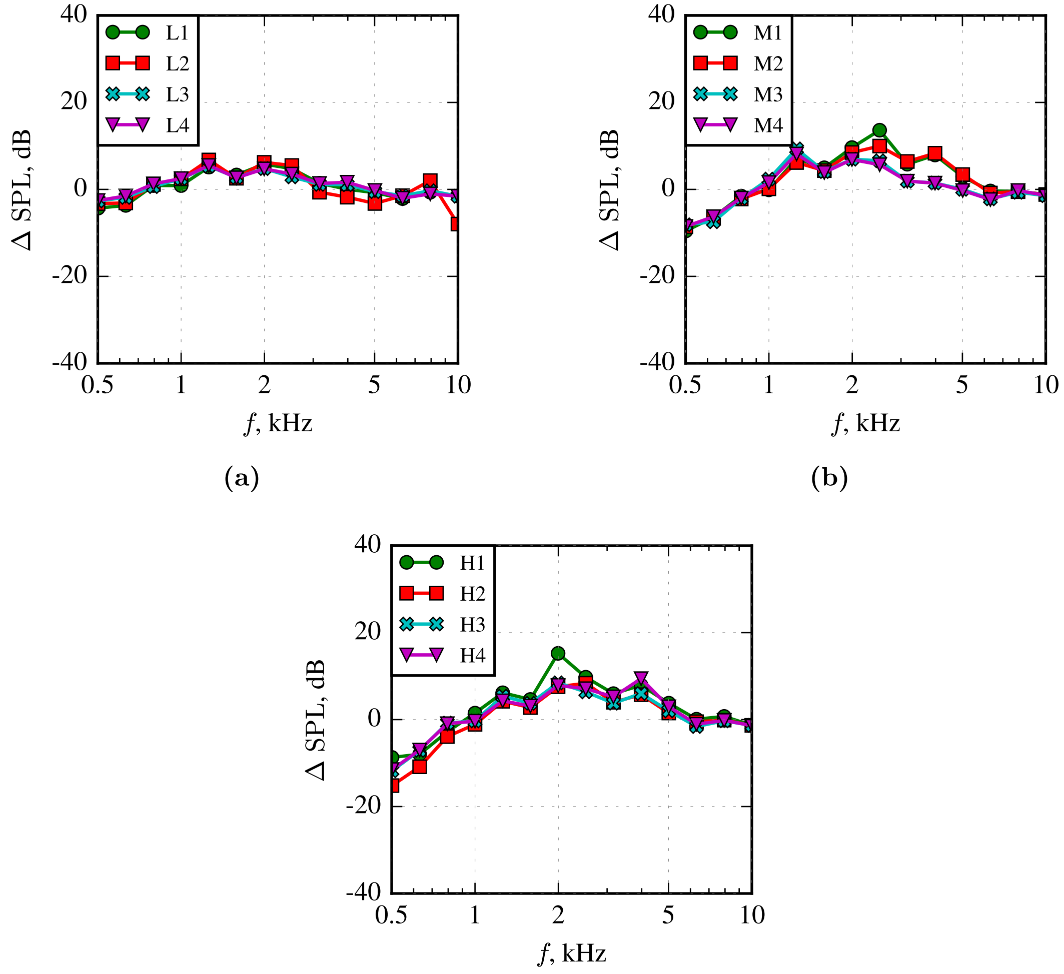

(a) **(b)** **(c)**

Figure 3.17: ΔSPL from the entire integration area of the (a) low-, (b) medium-, and (c) high-porosity plates compared to the nonporous plate at $U = 9$ m/s.

Figure 3.19 illustrates this change in SPL at the next selected flow speed of $U = 30$ m/s. As in the results at the lower flow speeds, the low-porosity plates, shown in figure 3.19a, reduce noise the least– up to approximately 7 dB at select frequencies. The medium-porosity plates in figure 3.19b and the high-porosity plates in figure 3.19c reduce noise up to 10 dB and 12 dB respectively. However, the maximum decrease in SPL is not as large as seen in the results $U = 18$ m/s. Similarly at the two lower flow speeds, with an increase in porosity comes an increase in the high-frequency noise (up to 18 dB for the highly-porous plates), and plates of the same hole shape within each groups perform similarly to each other,

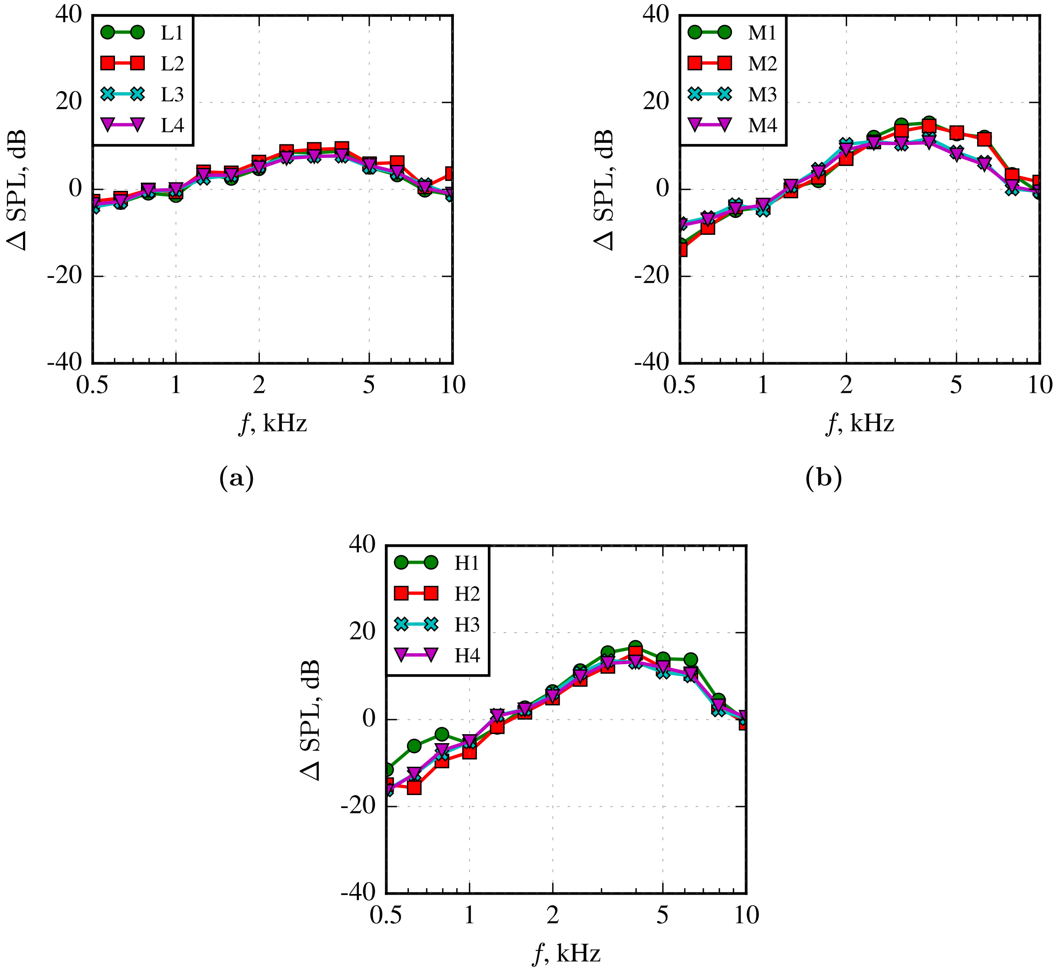

(a)

(b)

(c)

Figure 3.18: ΔSPL from the entire integration area of the (a) low-, (b) medium-, and (c) high-porosity plates compared to the nonporous plate at $U = 18$ m/s.

with the exception of plate H1 which does not decrease noise as much as H2. Compared to the previously presented results at lower flow speeds, each set of plates reduces noise across a broader range of frequencies. Lastly, the porous plate H2 is once again the overall best performer for reducing noise at low frequencies the most and increasing noise at high frequencies the least.

In this last set of figures that presents ΔSPL over the entire integration area, figure 3.20 shows these results from the flow speed of $U = 40$ m/s. Each grouping of plates reduces the low-frequency noise less than at the lower flow speeds. The maximum reduction of

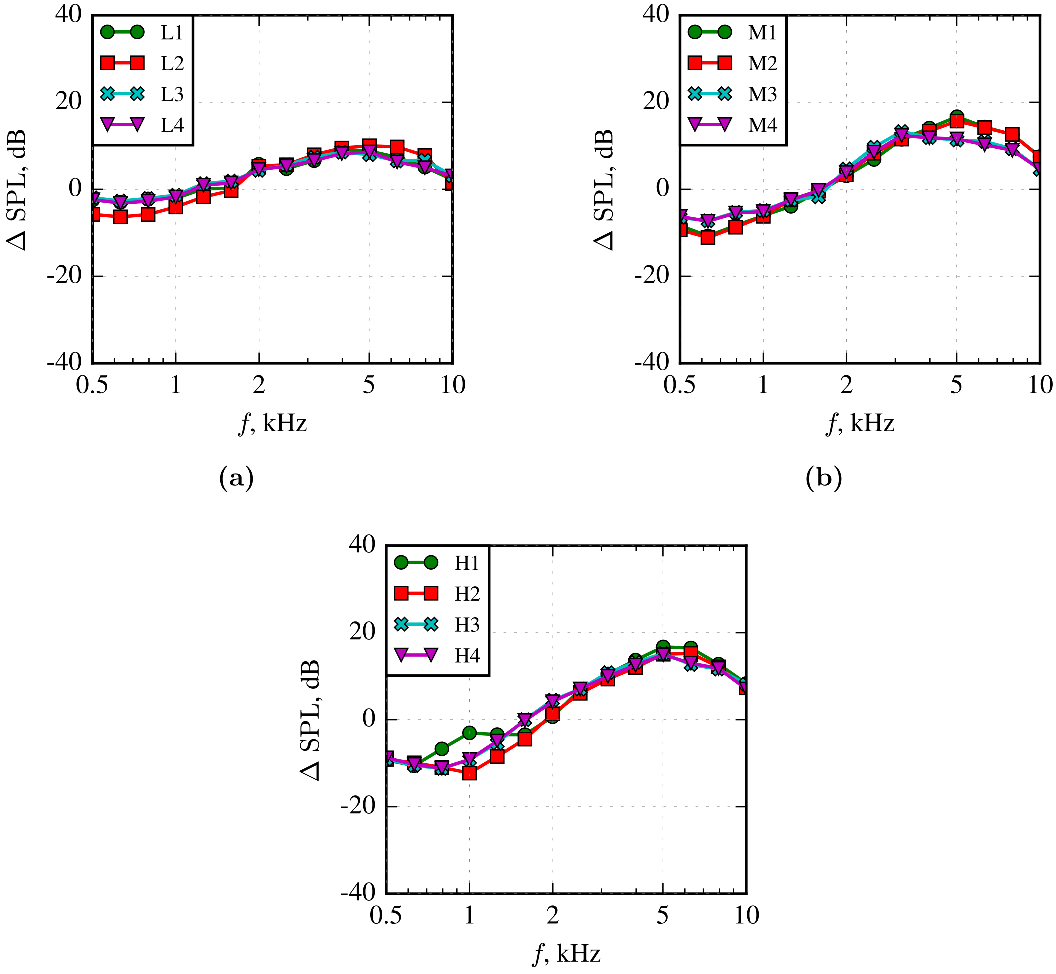

(a) **(b)**

(c)

Figure 3.19: ΔSPL from the entire integration area of the (a) low-, (b) medium-, and (c) high-porosity plates compared to the nonporous plate at $U = 30$ m/s.

low-frequency noise is 10 dB and occurs at $f = 500$ Hz for the H4 plate. Compared to at $U = 30$ m/s, each grouping of plates reduce noise across a smaller frequency range, and the increase in noise at high frequencies is very similar (up 18 dB). Like the results at $U = 30$ m/s and lower flow speeds, plates of the same hole shape within the low, medium, and high porosity groups perform similarly to each other, with the exception of plate H1 which does not decrease noise as much as H2, which is once again the best performer. The decrease in performance of the porous plates with sharp TEs at this highest tested flow speed could be due to increased turbulence in the boundary layer at high flow speeds increasing the amount of self-noise caused by interaction of turbulence with the holes.

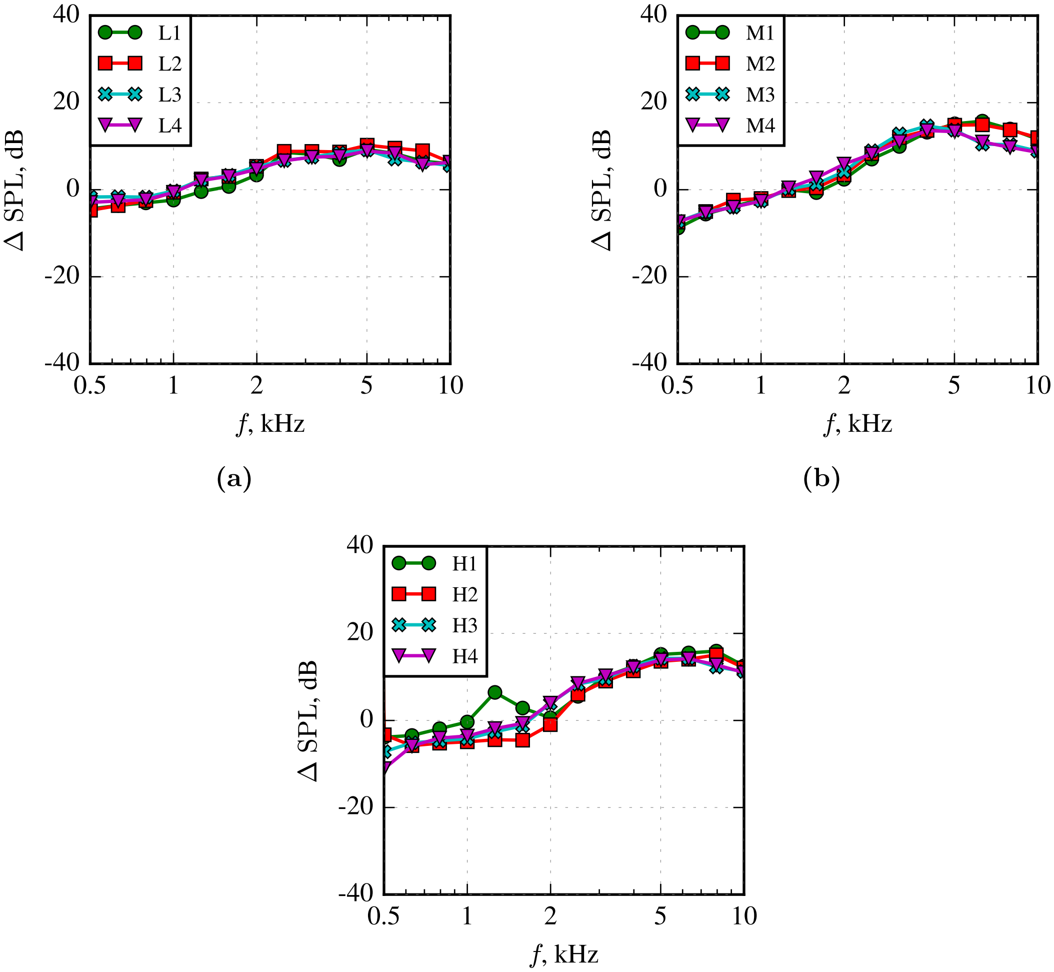

(a) **(b)** **(c)**

Figure 3.20: ΔSPL from the entire integration area of the (a) low-, (b) medium-, and (c) high-porosity plates compared to the nonporous plate at $U = 40$ m/s.

As the high-porosity plates perform the best at reducing noise at low frequencies and increasing high-frequency noise the least, their effect on the noise from the TE, LE, and the middle sector are analyzed to evaluate the effect of porosity on the total noise from the plates. Figure 3.21 plots the ΔSPL, calculated using (3.2), against frequency for noise integrated from the TE sector (see figure 2.13) using DAMAS beamforming at four different flow speeds. At the lowest tested flow speed, $U = 9$ m/s, the highly porous plates can reduce low-frequency noise by up to 18 dB and high-frequency noise by up to 20 dB. This large reduction in noise at high frequencies is only seen at this low flow speed and could be related to a possible lack of a fully-developed turbulent boundary; however, more data is necessary to substantiate this claim. Figure 3.18c shows results at the next flow speed $U = 18$ m/s. Here, the H2 plate can reduce low-frequency noise by up to 20 dB in the range of 500 Hz $< f <$ 1.8 kHz, and noise is increased at $f >$ 1.8 kHz. At $U = 30$ m/s noise is reduced by up to 15 dB in the range of 500 Hz $< f <$ 2 kHz, and noise is increased at $f >$ 2 kHz. Lastly, at the highest flow speed ($U = 40$ m/s) noise is reduced by 5 dB on average in the range of 500 Hz $< f <$ 2.2 kHz, and noise is increased at $f >$ 2.2 kHz by up to 18 dB. The greatest reductions in low-frequency noise are at the medium velocities (approximately $18 < U < 30$ m/s), and the greatest increase in high-frequency noise is at the highest velocities. In general, each of the H plates perform very similarly, with the exception of H1 and H2 at certain frequency ranges and flow speeds where H1 reduces low-frequency noise less and H2 decreases low-frequency noise more than the other H plates.

While the primary focus of this study is to investigate the effect of porosity on trailing edge noise, noise levels from different sectors of the plate are greatly affected by the presence of porosity and are discussed here. Figure 3.22 features the ΔSPL against frequency for noise integrated from the LE sector (see figure 2.13) using DAMAS beamforming at four different flow speeds for the high-porosity plates. At flow speeds $U \leq 18$ m/s, noise at low frequencies can be reduced by up to 22 dB. At medium to high flow speeds $U \geq 30$ m/s, this low-frequency noise can be reduced up to 11 dB. Similar to the effect of porosity on TE noise, the presence of porosity significantly increases noise at $f \gtrsim 2$ kHz at all flow speeds. Figure 3.22a features a tonal increase in high-frequency noise up to 26 dB. At all other flow speeds, the increase in high-frequency noise is broadband in shape and increases with flow speed, up to approximately 20 dB at $U = 40$ m/s. In general, similar trends in plate performance are seen; the H1 plate performs slightly worse at low-frequency noise attenuation, and the H2 plate performs slightly better than the rest of the highly porous plate at decreasing low-frequency noise and increasing high-frequency noise the least.

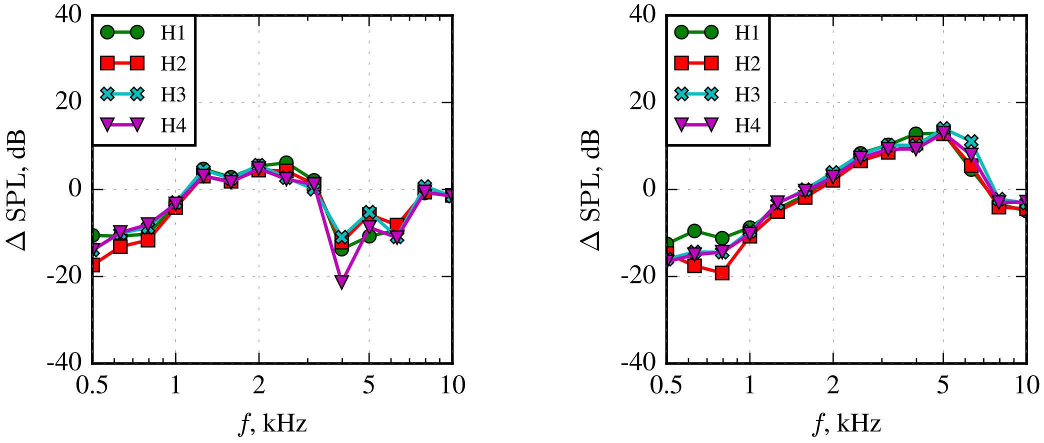

(a) $U = 9$ m/s

(b) $U = 18$ m/s

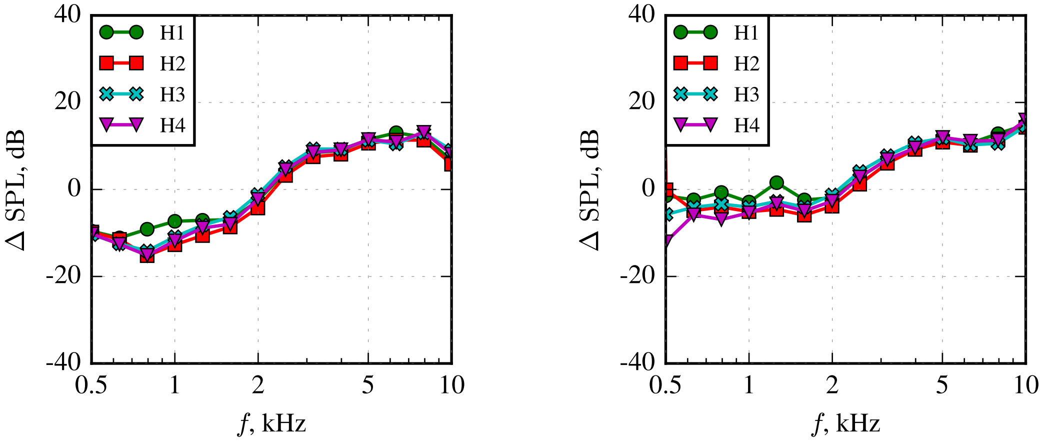

(c) $U = 30$ m/s

(d) $U = 40$ m/s

Figure 3.21: TE sector integrated SPLs for high-porosity plates at 4 different flow speeds.

The last set of figures featuring ΔSPL of specific sectors of the highly porous plate compared to the nonporous plate, figure 3.23 features noise integrated from the middle sector (see figure 2.13) of the plates using DAMAS beamforming. At flow speeds $U \leq 20$ m/s, noise at low frequencies can be reduced by up to 15 dB. At medium to high flow speeds $U \geq 30$ m/s, this low-frequency noise can be reduced up to 10 dB. Similar to the effect of porosity on TE and LE noise, the presence of porosity significantly increases noise at higher velocities at all flow speeds. However, for the middle sector, this increase is seen at frequencies as low as $f = 1$ kHz at the lowest flow speed. The high frequency excess

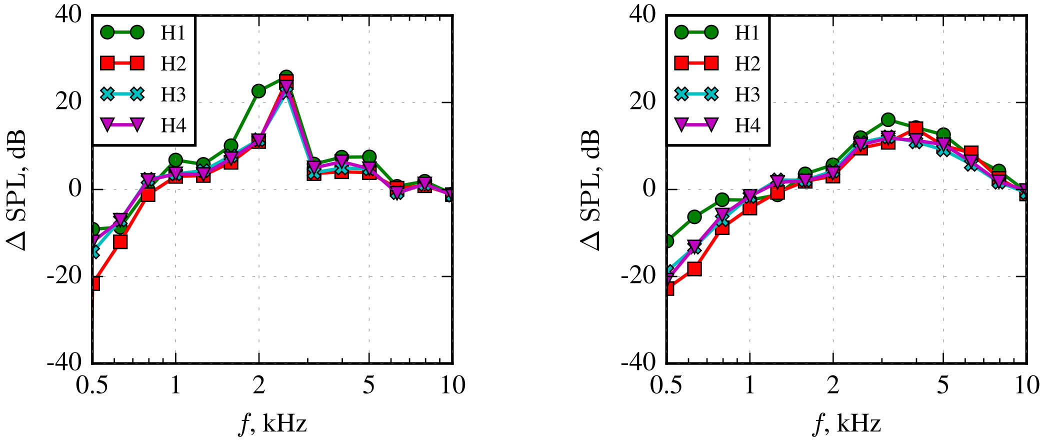

(a) $U = 9$ m/s **(b)** $U = 18$ m/s

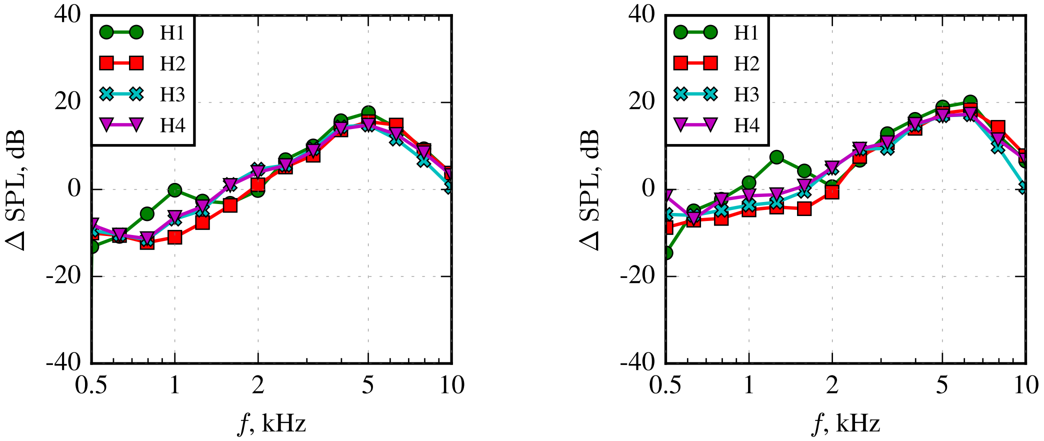

(c) $U = 30$ m/s **(d)** $U = 40$ m/s

Figure 3.22: LE sector integrated SPLs for high-porosity plates at 4 different flow speeds.

noise is broadband in shape and roughly increases with flow speed, up to approximately 18 dB at $U = 40$ m/s. In general, similar trends in plate performance are seen; the H1 plate performs slightly worse and the H2 plate performs slightly better than the rest of the highly porous plate at decreasing low-frequency noise and increasing high-frequency noise the least. Within the middle sector of the plates, the primary noise generation mechanism is the turbulent boundary layer. It is hypothesized that the holes themselves are responsible for the increase in noise at high frequencies, which could explain why the frequency range of the high frequency excess noise is largest in the middle sector compared to the TE and

LE.

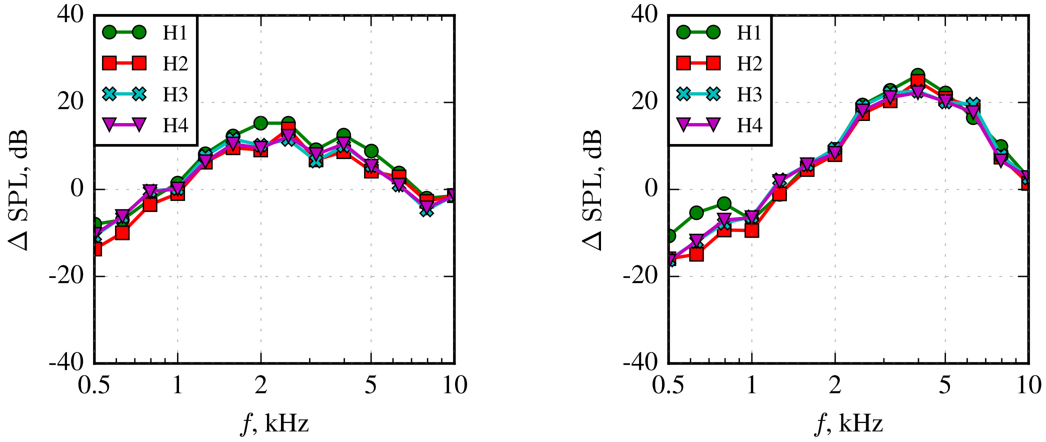

(a) $U = 9$ m/s **(b)** $U = 18$ m/s

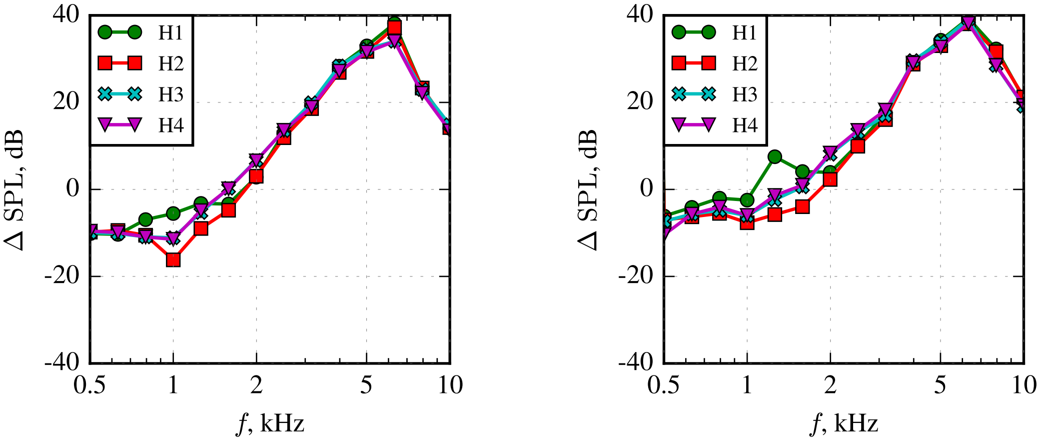

(c) $U = 30$ m/s **(d)** $U = 40$ m/s

Figure 3.23: Middle sector integrated SPLs for high-porosity plates at 4 different flow speeds.

Soundmaps are created using the CLEAN-SC beamforming algorithm [75] with a grid resolution of 1 cm and a dynamic range of 20 dB highlight the source of noise at various frequencies on the nonporous and porous plates. Figure 3.24 presents soundmaps at $f = 2$ kHz, $f = 4$ kHz, and $f = 8$ kHz for the NP, L1, M1, and H1 plates at $U = 30$ m/s. Soundmaps at frequencies below $f = 2$ kHz are not shown as CLEAN-SC does not perform well at these low frequencies, and while DAMAS does, its course grid makes the results difficult to visually interpret. At all frequencies shown, the sources of sound on the nonporous plate are primarily located at the TE and the junctions where the test plates meets the sideplates. In addition, at $f = 8$ kHz, the nozzle is a significant source of noise. Beginning with the low porosity plate L1 and increasing in magnitude with increasing porosity, large noise sources are also present in the middle of the plate for frequencies $f \geq 4$ kHz. The location of sound sources in the middle of the plate supports the idea that the holes themselves create a significant amount of noise at $f > 2$ kHz. Lastly, in addition to increase noise at high frequencies, the L1 and M1 porous plates also increase noise at the lowest presented frequency $f = 2$ kHz, whereas the H1 plate decreases noise at this frequency.

The next set of soundmaps are also created using the CLEAN-SC beamforming algorithm [75] with a grid resolution of 1 cm and a dynamic range of 20 dB to investigate the effect of hole shape and spacings on noise generated by the highly porous plates. Figure 3.25 presents soundmaps at $f = 2$ kHz, $f = 4$ kHz, $f = 8$ kHz for the H1, H2, H3, H4 plates at $U = 30$ m/s. Noise sources are located at the test plate-sideplate junction and TE for all presented frequencies. Significant noise sources are also present at the middle of the plate for frequencies $f \geq 4$ kHz. The difference in maximum amplitude between the soundmaps at the same frequencies is approximately ± 1.5 dB. Common trends are seen in both the maximum amplitude of noise and the spatial location of the noise sources for all of the H plates which supports the use of the dimensionless porosity parameter δ as a unifying parameter to describe the effects of porosity on flow noise.

3.3.1.2 Effect of chordwise extent of porosity on the acoustic field

As the presence of holes on the porous plates are known to increase noise at high frequencies, the next set of experiments investigates the effects of reducing the amount of holes on the porous plates. It is theorized that by covering up some of the holes, the porous plate will be able to reduce noise at low frequencies and increase the high frequency excess noise less compared to a fully porous version of the same plate. The base H1 plate is modified by covering up varying percentages of the chord with an adhesive sheet. Initially, the entire chord length on both sides of the tape are covered with the sheet, and then the sheet material

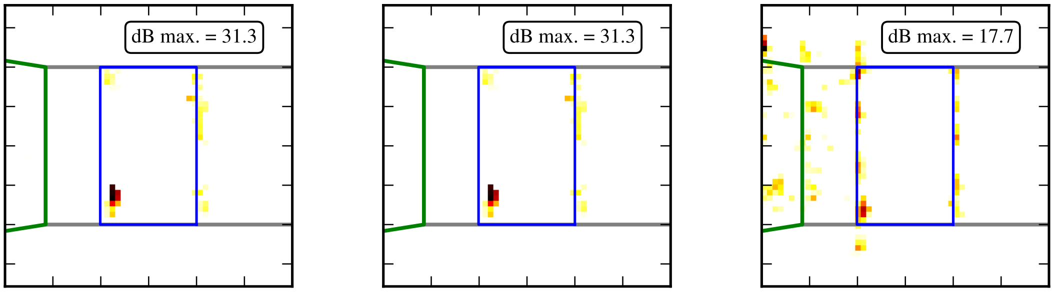

(a) NP, 2 kHz **(b)** NP, 4 kHz **(c)** NP, 8 kHz

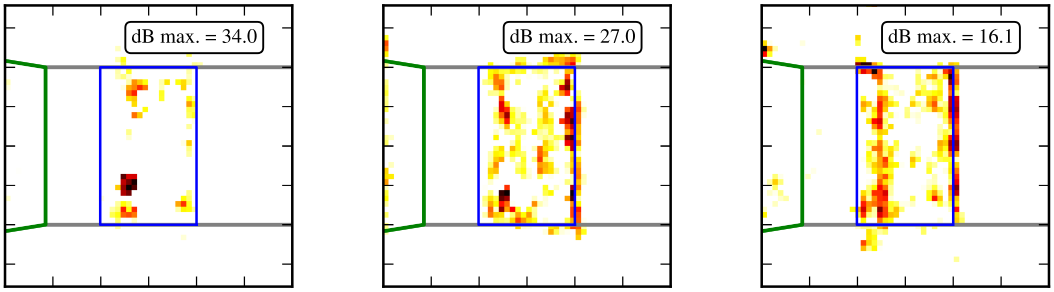

(d) L1, 2 kHz **(e)** L1, 4 kHz **(f)** L1, 8 kHz

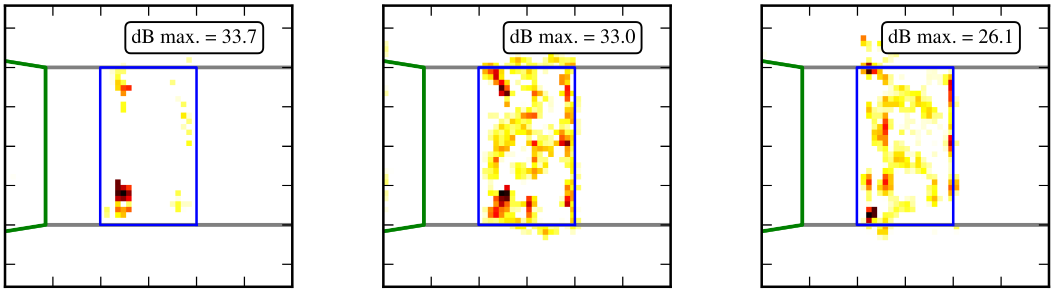

(g) M1 2 kHz **(h)** M1, 4 kHz **(i)** M1, 8 kHz

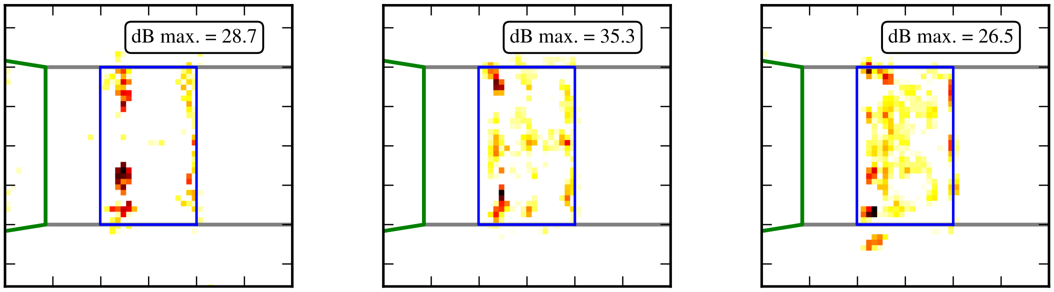

(j) H1, 2 kHz **(k)** H1, 4 kHz **(l)** H1, 8 kHz

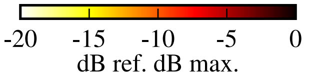

Figure 3.24: Comparing soundmaps at different porosity levels (NP, L1, M1, and H1) at $f = 2$ kHz, $f = 4$ kHz, and $f = 8$ kHz.

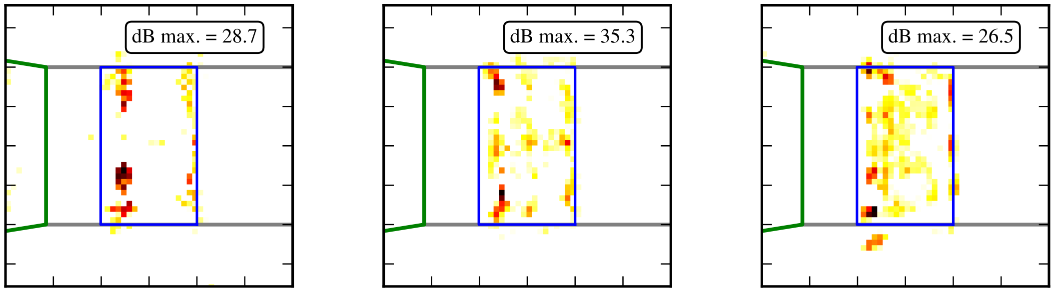

(a) H1, 2 kHz **(b)** H1, 4 kHz **(c)** H1, 8 kHz

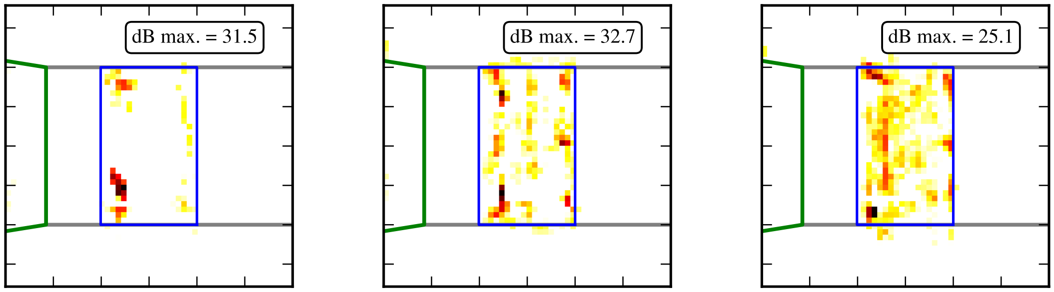

(d) H2, 2 kHz **(e)** H2, 4 kHz **(f)** H2, 8 kHz

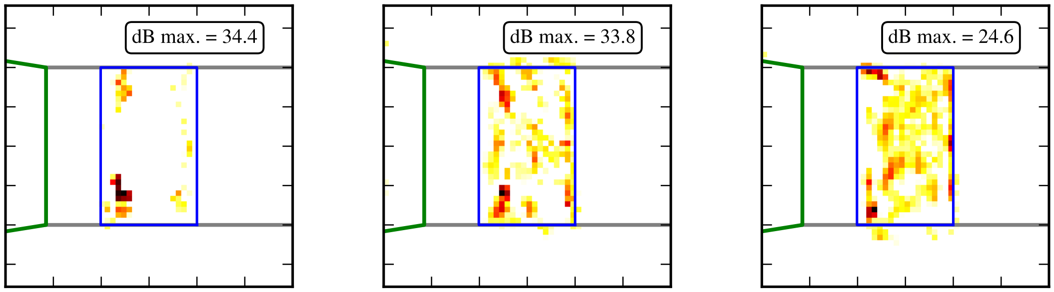

(g) H3, 2 kHz **(h)** H3, 4 kHz **(i)** H3, 8 kHz

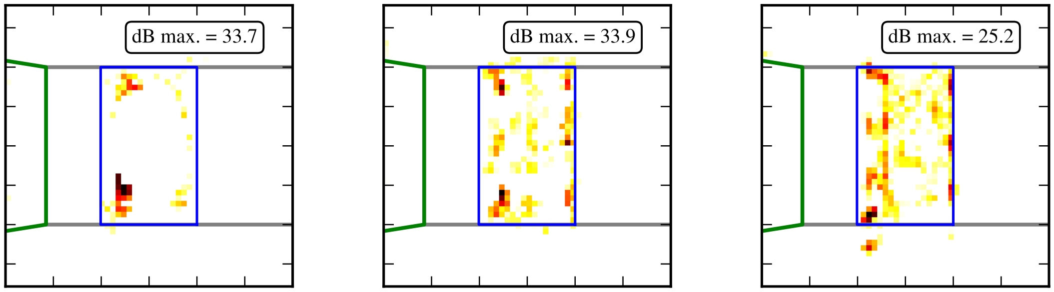

(j) H4, 2 kHz **(k)** H4, 4 kHz **(l)** H4, 8 kHz

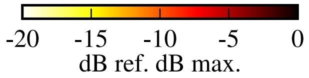

Figure 3.25: Comparing soundmaps from plates of the same δ (H1, H2, H3, and H4) at $f = 2$ kHz, $f = 4$ kHz, and $f = 8$ kHz.

is removed in the direction of the TE to the LE to yield 5%, 10%, 25%, and 50% porous chord. The adhesive sheet is very thin and does not functionally change the thickness of the plate.

Figure 3.26 compares the effects of varying levels of porous chord for the H1 plate at three different flow speeds. Results indicate that the high frequency excess noise is reduced by reducing the amount of holes present. On average, reducing the extent of the holes from 100% to 5% of the chord length results in 4 dB less noise at frequencies $f > 2$ kHz. This comes at a cost as the noise reductions at low frequencies $f < 2$ kHz are also reduced. Interestingly, even with just a 5% porous chord (just one row of holes at the TE), there is a significant increase in high-frequency excess noise, and these trends are similar at all tested flow speeds.

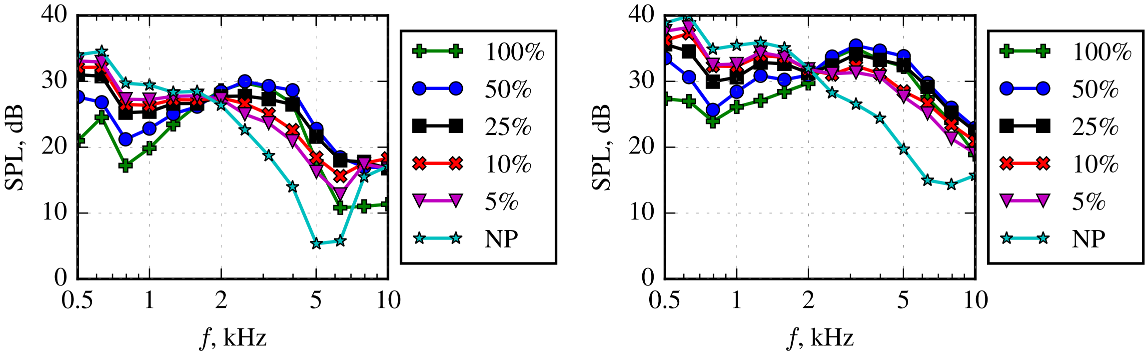

(a) $U = 18$ m/s **(b)** $U = 25$ m/s

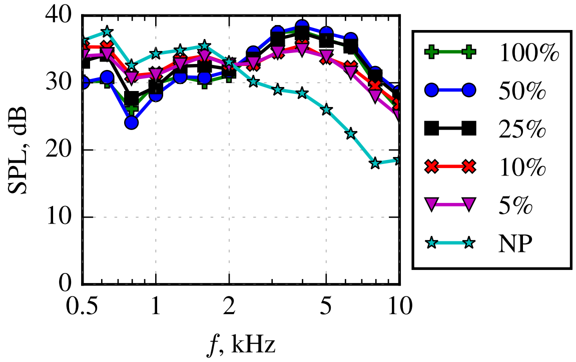

(c) $U = 30$ m/s

Figure 3.26: TE integrated SPL vs. f for the highly porous H1 plate at various levels of porous chord compared to nonporous plate.

Soundmaps are generated for the tests with varying levels of porous chord. As the high frequency excess noise is affected by changing the amount of porous chord, figure 3.27 shows soundmaps created using CLEAN-SC [75] with a grid resolution of 1 cm and a dynamic range of 20 dB at a select high frequency, $f = 8$ kHz for the H1 plate with a 25%, 50%, and 100% porous chord. For the case of the 100% porous chord the sound sources are located all across the plate, including the middle section, where the holes are thought to create noise at this frequency. By reducing the amount of porous chord, the location of the sound sources is reduced to a smaller area, namely the width of the section containing the uncovered holes.

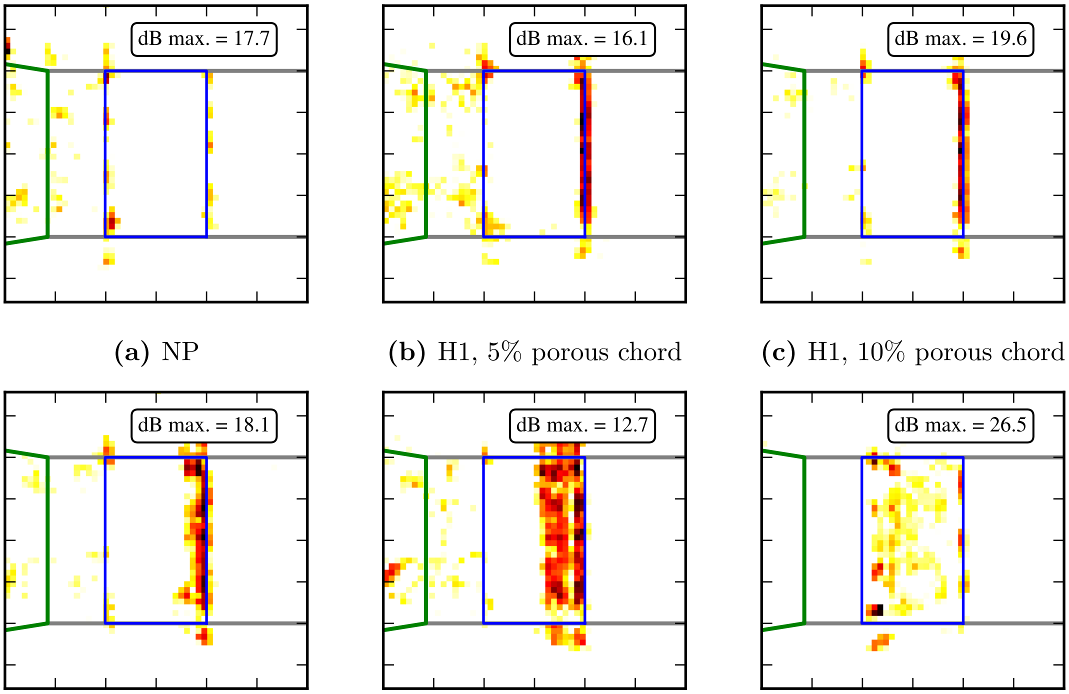

(a) NP **(b)** H1, 5% porous chord **(c)** H1, 10% porous chord

(d) H1, 25% porous chord **(e)** H1, 50% porous chord **(f)** H1, 100% porous chord

Figure 3.27: Beamforming soundmap at $f = 8$ kHz for nonporous and H1 porous plate with varying levels of porous chord to demonstrate effect on high-frequency noise generation.

3.3.1.3 Effect of changing angle of attack on the acoustic field

In this set of experiments, the angle of attack α of the plate in the tunnel was varied from to 4° and 11° to investigate its effect on the generation of flow noise by a nonporous and select set of porous plates. Testing at various angles of attack is relevant for real-world applications of porous edges and could shed light on the viability of applying porous edges to aerial vehicles and other engineering devices. Using the correction method of Brooks, Pope, and Marcolini [2], these angles correspond to a corrected angle of attack α_c of 1.5° and 4.1° respectively. Because open wind tunnels can cause flow curvature and downwash deflection of the incident flow which can reduce the angle of attack [2], α_c is calculated to represent the angle in free air required to give the same lift as α creates in the tunnel.

Figure 3.28 displays the SPL against f for noise integrated from the TE for the NP, L1, M1, and H1 plates at various angles of attack at $U = 30$ m/s. The H1 porous plate reduces noise by up to 3 dB and 7 dB at $f = 1$ kHz for $\alpha_c = 1.5°$ and $\alpha_c = 4.1°$. At this frequency at $\alpha_c = 0°$, no reduction is seen by the H1 plate. Lastly, increasing α_c increases the high-frequency excess noise. For example, at $\alpha_c = 4.1°$, the magnitude at $f = 8$ kHz for the H1 plate is 17 dB more than at than the $\alpha_c = 0°$, which is already a near 10 dB increase over the nonporous plate.

The good performance of the porous plates at reducing low-frequency noise at small α_c motivate a more detailed experimental study to investigate this behavior in depth.

3.3.1.4 Effect of hole fillet on the acoustic field

The holes on the porous plates may contribute to the high-frequency excess noise due to generating excess turbulence near the plate surface (see §4). For example, the sharp edges on the holes themselves may act as edges that the boundary layer interacts with, leading to a scattering mechanisms responsible for the excess high-frequency noise. To investigate this possible mechanism further, the three copies (H1a, H1b, and H1c) of the H1 porous plate are made with filleted through-holes of different fillet radii as described in §2.1.1. H1a has the smallest fillet radius (0.5 mm), and H1b and H1c have fillet radii of 1 mm and 1.5 mm, respectively. Figure 3.29 presents SPL integrated from the TE region against frequency at three different flow speeds for the nonporous plate compared to the baseline H1 plate and the H1 plates with filleted through-holes. It is immediately noticeable that the H1c plate,

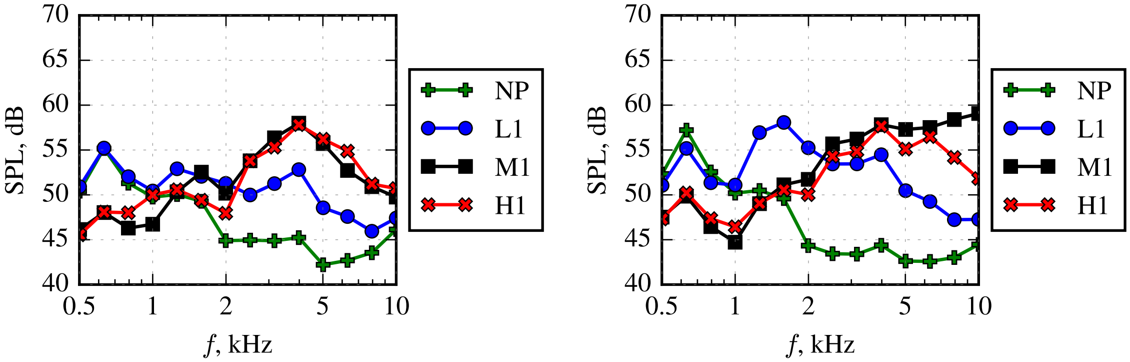

(a) $\alpha_c = 0°$ **(b)** $\alpha_c = 1.5°$

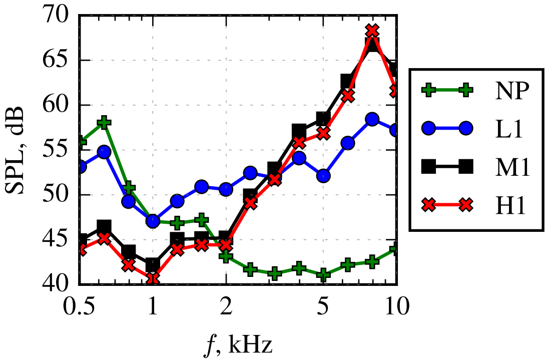

(c) $\alpha_c = 4.1°$

Figure 3.28: Effect of changing corrected angle of attack (α_c) on the NP, L1, M1, and H1 plates at $U = 30$ m/s.

or plate with the largest fillet radius, increases noise at all frequencies compared to the nonporous plate. This increase was noticed in the test facility, where a loud whistling tone was present during the testing of the H1c plate. The exact cause of this effect is unknown and was not revealed in the course of the dissertation research effort.

Interestingly, the H1a and H1b plate reduce low-frequency noise as well as the baseline H1 plate in the frequency range $f < 2$ kHz. At certain low frequencies, the H1a plate even reduces the SPL by 3 dB more than the baseline H1. As observed for the rest of the H1 plates, H1a and H1b increase noise at $f > 2$ kHz very similarly to that of H1; however, at select high frequencies, the H1a plate increases noise marginally less than the H1 plate. The acoustic good performance of plate H1a at low frequencies may suggest a more comprehensive future campaign to investigate the acoustic and flow effects of plates

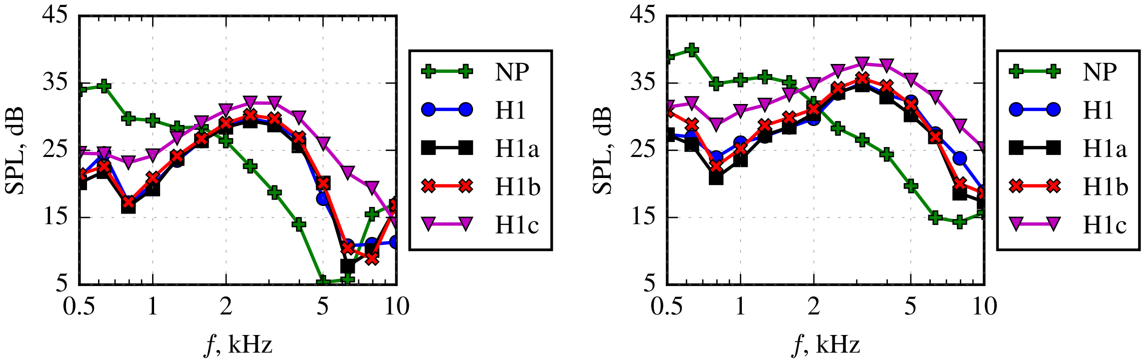

(a) $U = 18$ m/s **(b)** $U = 25$ m/s

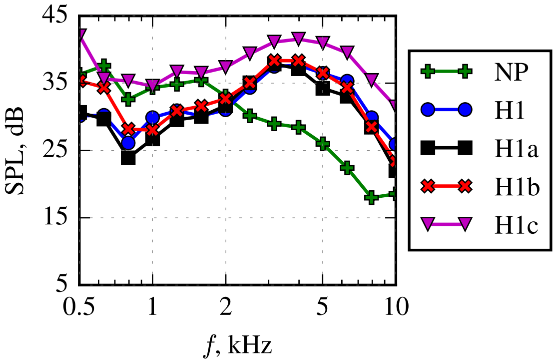

(c) $U = 30$ m/s

Figure 3.29: TE integrated SPL vs. f for the porous plates with filleted holes compared to nonporous plate.

with filleted through-holes in more detail.

3.3.1.5 Acoustic trends on the dimensionless porosity parameter

This section focuses on plotting the ΔSPL of the porous plates against the porosity parameter δ. The δ parameter controls the effect of porosity on the scaling of noise generated by a quiescent source at the TE. This parameter is extended to this use case of a turbulent boundary layer generating TE noise, and the porous plates are characterized by this parameter in §2.1.1. Recall from (1.1) that $\delta = 2\alpha_h c/\pi^2 fR$. The presence of f in the denominator of δ allows the sound pressure levels to be plotted against this parameter. Figure 3.30a presents the ΔSPL for the L1, M1, and H1 porous plates. The levels are calculated using delay-and-sum beamforming and should be used for inspection of the crossover-frequency

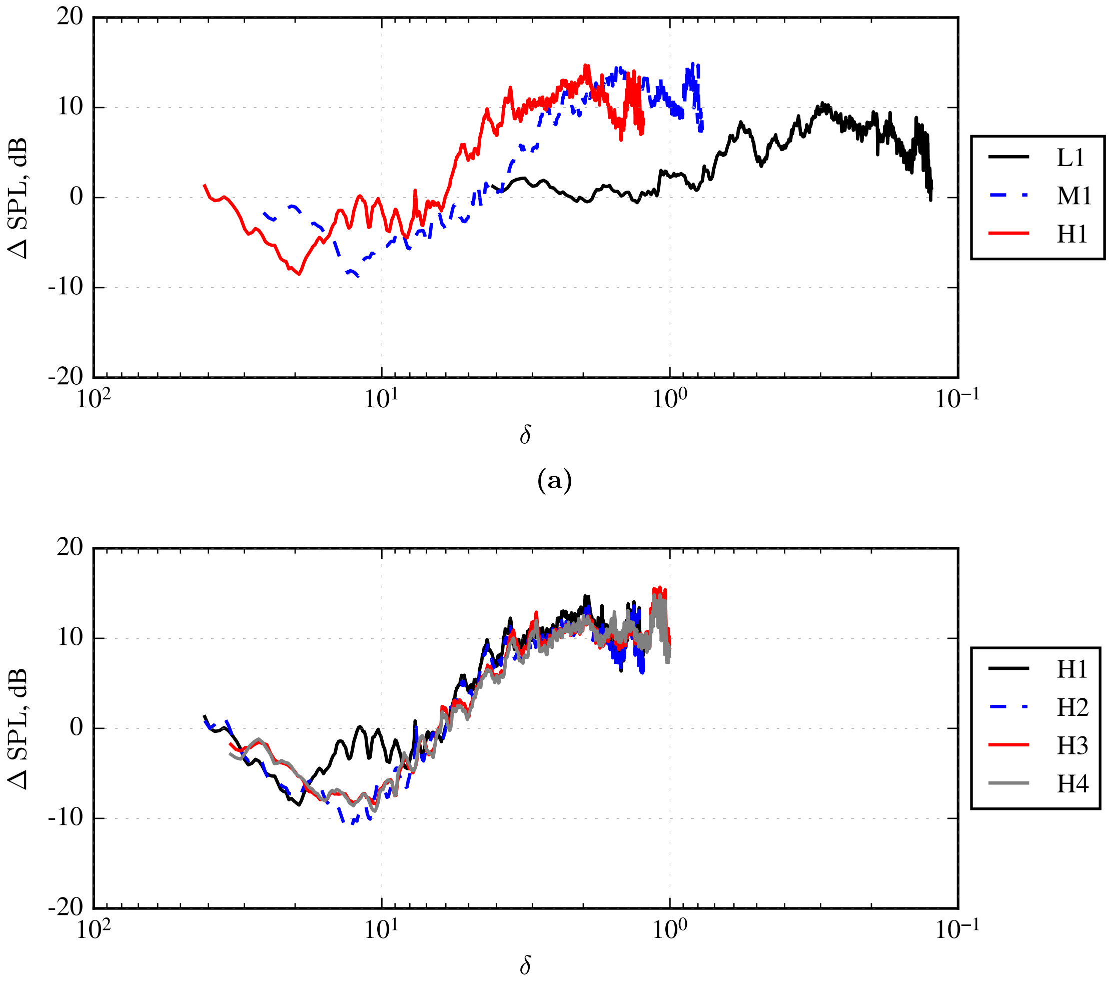

(a)

(b)

Figure 3.30: ΔSPL against δ at $U = 30$ m/s ($Re = 3.37 \times 10^5$) for (a) plates of varying δf and (b) plates of near-same δf.

only. As is standard in other figures with ΔSPLs, a negative value represents a reduction in noise and a positive value indicates an increase in noise by the porous plates. Interestingly, the δ range in which the cross-over from noise reduction to noise increase occurs in within $10^1 < \delta < 10^0$. This is the same relative range of δ where the scaling exponent (γ) of noise with velocity changes from U^5 to U^6 for a quiescent source generating TE noise [12, 15, 17]. In other words, noise reductions are expected to and do occur at approximately $\delta \geq 10$ in this extension of the δ parameter to the case of a turbulent boundary layer generating TE noise. We see that due to the low amount of porosity of the L1 plate, nearly the entire frequency range of interest (500 Hz $< f <$ 10 kHz), when transferred into the δ range, occurs at $\delta \gg 10^1$, and at nearly all δ, the L1 plate increases noise.

Figure 3.30b presents the ΔSPL against δ at $U = 30$ m/s ($Re = 3.37 \times 10^5$) for each of the H plates. The ranges of noise reduction and noise increase for each of the plates collapse together well when plotted against δ. The results presented in figure 3.30 once show promise in using δ to anticipate the effects of porosity on turbulent boundary layer trailing edge noise, despite the use of δ being extended past its original design.

3.3.2 Overall sound pressure levels and directivity

The overall sound pressure level (OSPL) is calculated using (2.9). Figure 3.31 presents the OSPL against Re for the (a) low-, (b) medium-, and (c) high-porosity plates. The low-porosity plates barely reduce the OSPL, and in general, like in the case of the plates with blunt TEs, with an increase in porosity and moving to the M and H plates comes an increase in the reduction of OSPL, which is up to 5 dB for the H plates. These reductions in OSPL taper off with an increase in flow speed. As discussed in the beginning of §3.3.1.1, the DAMAS beamforming incorrectly locates the source of the noise at $f = 500$ Hz to a region outside of the TE. Because this is the highest magnitude frequency for the nonporous plate, its absence from the TE region leads to an OSPL from the TE for the nonporous plates that is much lower than expected. The position of the high magnitude source at $f = 500$ Hz to outside of the plate integration area for the nonporous plate is what then leads to the porous plates having a much higher OSPL compared to the nonporous at high flow speeds. The exact cause of this incorrect location of the maximum sound pressure level at $U = 40$ m/s is unknown but could be related to increase sheared layer effects at high velocities. See §A.4 for further details on this discrepancy, including soundmaps showing the change over to the incorrect location of the $f = 500$ Hz noise source at $U = 40$ m/s.

The next set of plots in figure 3.32 shows the directivity of sound generated by the nonporous, L2, M2, and H2 plates at select frequencies at $U = 25$ m/s. The reduction in noise by the porous plates at low frequencies (here specifically $f = 750$ Hz) is shown in

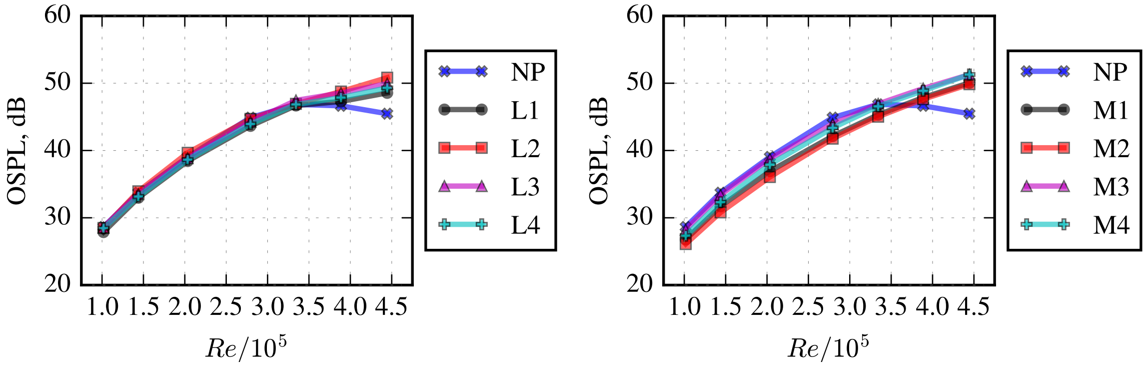

(a) Nonporous vs. low-porosity plates **(b)** Nonporous vs. medium-porosity plates

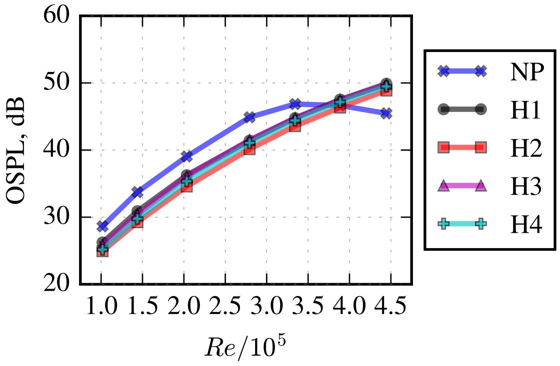

(c) Nonporous vs. high-porosity plates

Figure 3.31: Dependence of OSPL on *Re* from the TE sector for (a) low, (b) medium, and (c) high-porosity plates.

figure 3.32a where a reduction in noise, up to 20 dB, is seen at all microphone positions. The next plots shown in figure 3.32b and figure 3.32c shows the SPL generated at $f = 2$ kHz and $f = 4$ kHz respectively. The porous plates increase noise at all microphone locations at these frequencies. In general, there is no noticeable change in the shape of directivity which is likely due to the fact that these SPLs are measured directly from the individual microphones and the TE noise, which is anticipated to change directivity at certain frequencies, is could be covered up by noise from other sources on the plate and the setup. Lastly, figure 3.33 shows the directivity of the OSPL generated by the nonporous, L2, M2, and H2 plates at $U = 25$ m/s. Here, the porous plates increase the OSPL at almost all microphone locations at flow speeds, with the exception of plate H2 which reduces OSPL at a limited number of microphones. An increase in OSPL is seen here as the individual microphones capture the

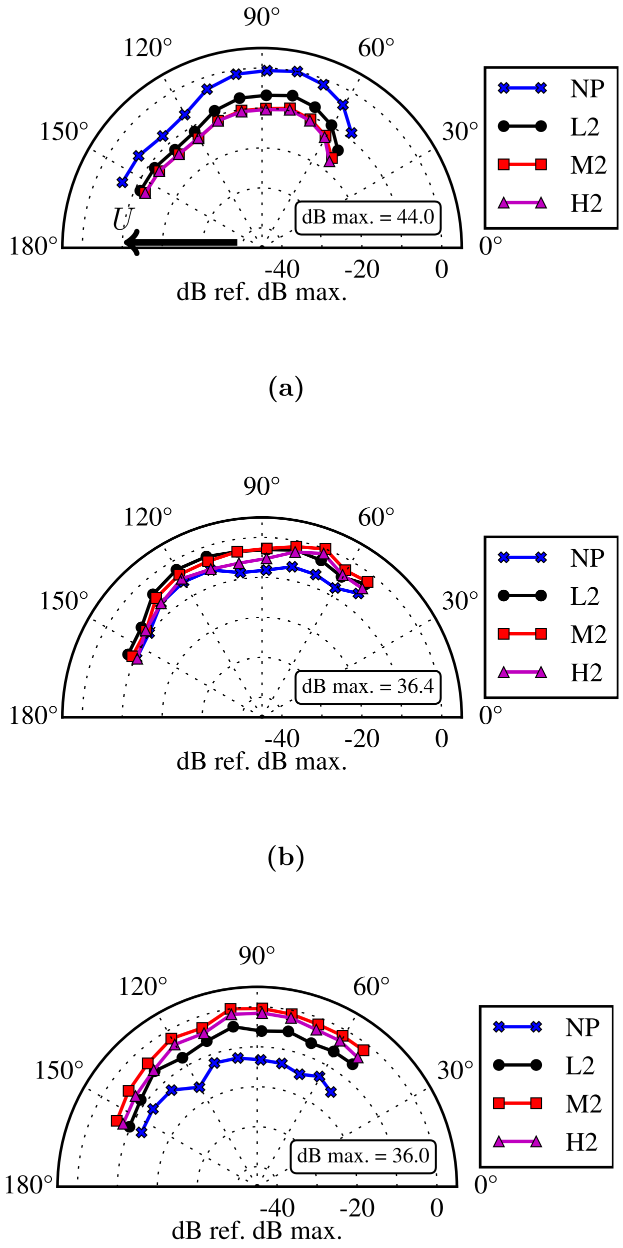

(a)

(b)

(c)

Figure 3.32: Directivity of sound generated by nonporous plates and select porous plates at (a) $f = 750$ Hz, (b) $f = 2$ kHz, and (c) $f = 4$ kHz at $U = 25$ m/s.

total of all the sound sources, and noise from the setup and other regions corrupt the TE noise (the type of sound expected to be reduced). Likely for the same reason, there is no

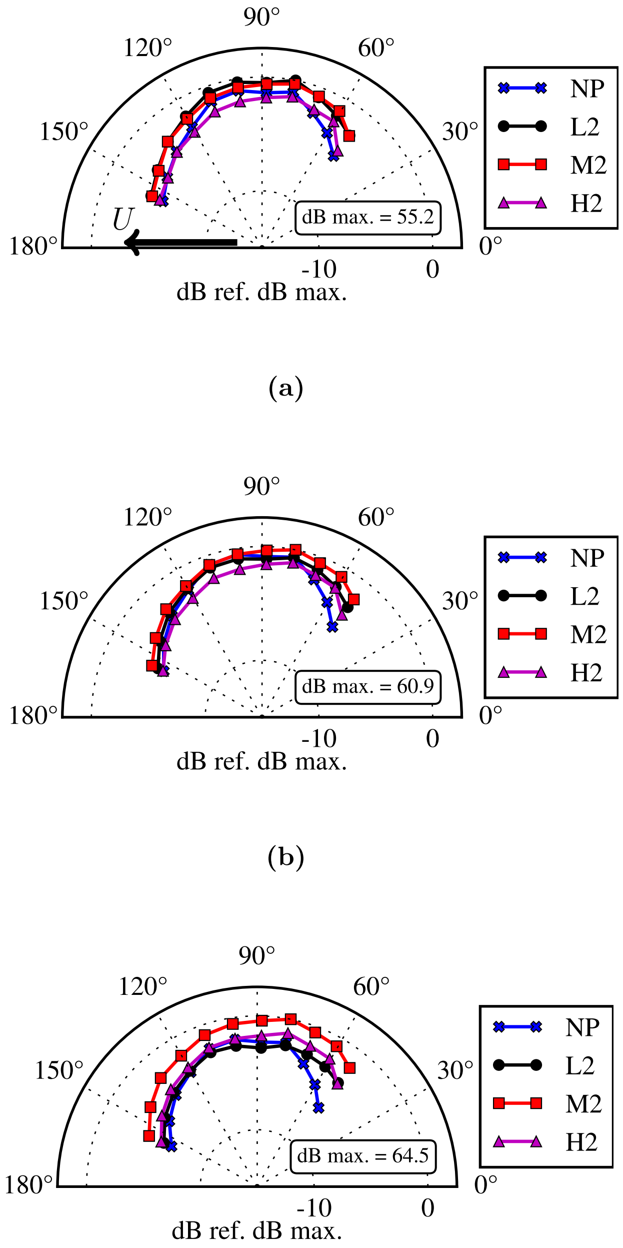

(a)

(b)

(c)

Figure 3.33: Directivity of OSPL calculated from 500 Hz to 10 kHz of the nonporous plates and select porous plates at (a) $U = 18$ m/s, (b) $U = 25$ m/s, and (c) $U = 30$ m/s.

noticeable change in the directivity of the OSPL.

3.3.3 Acoustic scaling on flow speed of nonporous and porous plates

The velocity scaling exponent is determined for select experiments using the methods described in §2.4. Figure 3.34 shows the log-log plot of the sound pressure integrated from the TE region against the flow speed in an attempt to calculate the velocity scaling exponent γ of the radiated acoustic intensity across three frequency ranges: 500 Hz to 10 kHz, 500 Hz to 2 kHz, and 2 kHz to 10 kHz. Compared to the anticipated $\gamma = 5$ and $\gamma = 6$ scaling for a nonporous and porous edge from literature [12, 15, 17], the exponent values are much lower.

In the largest frequency range (500 Hz to 10 kHz), the exponent values are $\gamma = 2.58$ and $\gamma = 3.74$ for the nonporous and H1 porous plate respectively, and these values are $\gamma = 2.32$ and $\gamma = 2.61$ in the 500 Hz to 2 kHz. These low exponent values for the nonporous plate are likely caused by the non-linear increase in OSPL for the nonporous plate at velocities $U \geq 30$ m/s, which is related to the incorrect locating of the low-frequency sound sources at these high velocities (see §A.4). In the high frequency range (2 kHz to 10 kHz), the exponents are higher at $\gamma = 3.67$ and $\gamma = 4.54$ for the nonporous and porous plates, respectively. These higher exponents could be due to the ability of beamforming algorithms to more accurately located higher frequencies than lower frequencies; thus, the noise in this frequency range is more confidently located at the TE.

While it is interesting that the scaling exponent for the porous plate is higher than that of the nonporous plate, it is still very far off from the theoretical value. The low exponent values in comparison to the anticipated $\gamma = 5$ and $\gamma = 6$ could be due to many factors in the measurement and calculation procedures. First, measurement uncertainties, which are quite low for i.e. SPL comparisons, might be the cause of the low exponent which is very sensitive to small changes in pressure or flow speed as found in previous works [63, 64, 94].

3.3.4 Summary

Acoustic spectra, beamforming soundmaps, overall sound pressure levels, and directivity patterns of porous flat plates with sharp TEs are presented from a set of measurements

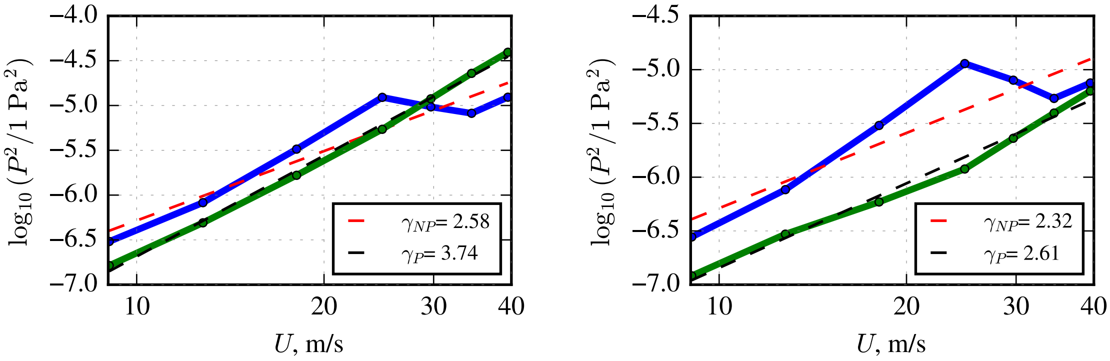

(a) 500 Hz to 10 kHz **(b)** 500 Hz to 2 kHz

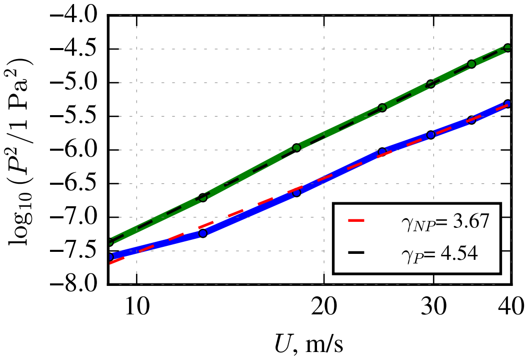

(c) 2 kHz to 10 kHz

Figure 3.34: Estimation of the flow speed exponent γ for the porous and nonporous edges. $\log - \log$ plot of power-spectral density acoustic pressure from the TE region against flow speed U for the nonporous and H1 plate with sharp TEs for various frequency ranges.

conducted in the BTU wind tunnel with flow speeds ranging from $9 < U < 40$ m/s. The porous plates are the same set of plates as used in §3.1, but with sharpened TEs. The dimensionless porosity parameter δ can be used to anticipate regions of noise reduction and noise increase. With an increase in the porosity of the plates in terms of δ comes an increase in noise reductions at low frequencies ($f < 2$ kHz). The sound pressure level of the trailing edge region can be reduced by up to 20 dB by the highly porous plates. While the plates decrease noise at low frequencies, they are known to increase noise at $f > 2$ kHz with increasing porosity. Like in the measurements of plates with blunt edges in WTC-1 and WTC-2, this increase could be due to the holes creating excess noise, in a similar way that other porous designs have lead to high-frequency noise, attributed to roughness noise

[14, 43, 44, 55]. Plates with the same δf perform similarly. Within each grouping of plates (low, medium, and high), the plates with circular holes slightly outperform plates with square holes at reducing low-frequency noise the most and increasing high-frequency noise the least. Aligning or staggering the spacings of holes in the flow direction is not seen to play a large role in effects of the porosity on the acoustic field.

Interestingly, the frequency range at which the porous plates reduce noise is approximately 0.5 kHz $< f <$ 2 kHz. The high-frequency excess noise onsets at approximately $f = 2$ kHz, which is close to the frequency for the WTC-1 plates where the plate becomes non-compact ($f > c/c_l$). This relationship appears to be coincidental, as the high-frequency noise onset frequency and frequency of acoustic non-compactness are not related in the measurements in WTC-2 and the remote-controlled glider measurements in §5.

In an attempt to mitigate this high-frequency excess noise, varying levels of the porous chord are covered up in a select set of experiments. With the reductions in the amount of holes present comes a decrease in the high-frequency excess noise; however, the low-frequency noise reductions are also limited with a smaller percentage of porous chord.

While the majority of the measurements are conducted at $\alpha_c = 0°$, a select set of measurements are made at angles $\alpha_c > 0$. At a single small angle-of-attack, low-frequency noise is reduced slightly more than in the case $\alpha_c = 0°$; however, a significant increase in the α_c brings about large increases in the high-frequency excess noise. Further attempts to understand and mitigate this noise are made by filleting the through holes with fillets of different radii. The plate with the largest fillet radii lead to an audible whistling sound and created excess noise at all frequencies. A moderate fillet radius was shown to reduce low-frequency noise slightly better than the non-filleted porous baseline suggesting a more detailed study into the acoustic effects of filleted through-holes.

Lastly, the porous plates are shown to reduce OSPLs from the TE region by up to 4 dB, and directivity, as measured by individual microphones on the arc-array, does not significantly with changes in porosity; this lack of significant change in directivity with changes in porosity could be due to other noise sources suppressing the TE noise.

Chapter 4

Flow measurements near porous and nonporous test plates

Hot-wire anemometry is used to interrogate the flow field of the plates with blunt and sharp trailing edges from WTC-1 in the BTU wind tunnel. Measurements are conducted at two locations on the nonporous and porous plates: 1 mm downstream from the trailing-edge in the near-wake of the plates, and 5 mm upstream of the trailing edge. In both cases, the hot-wire probe begins as close to the edge as possible, and the probe traversed away from the edge in the vertical (z) direction. Further details of the hot-wire anemometry setup are described in §2.2.1.2.

4.1 Blunt edges

First, hot-wire anemometry tests are conducted at a flow speed of $U = 30$ m/s ($Re = 3.37 \times 10^5$) in the near wake and upstream from the TE of the blunt-edged nonporous plate and a selected porous plate (H1) to further investigate the suspected source of the bluntness-vortex shedding and the associated tonal peaks. The H1 plate was chosen for its ability to best reduce the tonal peak noise among the plate specimens considered. The resulting velocity profiles from the near-wake and upstream measurements of the nonporous and porous plates are shown in figure 4.1. The theoretical boundary layer height is also shown in figure 4.1 as a yellow star. To aid in viewing, every other measurement location is plotted and represented by a marker, and all of the points are connected with a spline fit.

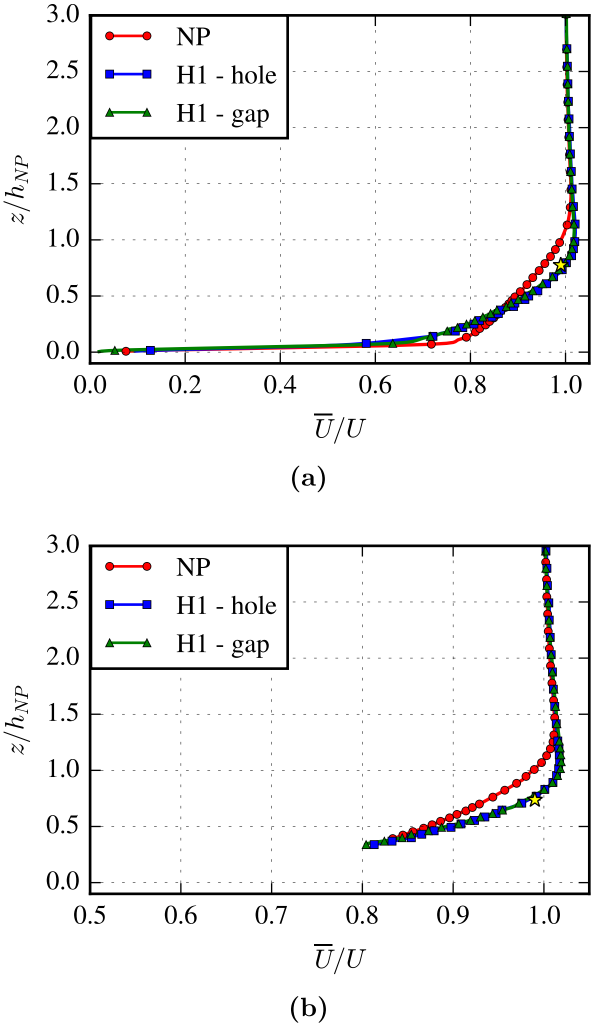

Figure 4.1: $\overline{U}/U$ profiles at $Re = 3.37 \times 10^5$ from nonporous plate (NP) and H1 plate measured in the (a) near-wake and (b) upstream of the TE.

Figure 4.1a shows the velocity profiles measured in the near wake of the nonporous and H1 porous plate, where the vertical axis, the distance from the test plate, is normalized by the nonporous boundary layer height, $h_{\text{NP}} = 6.4$ mm. The h measured behind a pore (labeled H1 - hole) on the porous plate, measured at point A in figure 2.7b, is 4.6 mm, and the h measured along the plate between pores (labeled H1 - gap), at point B is 4.8 mm. The boundary-layer thickness from the porous cases is smaller than that of the nonporous case. In addition to estimating the boundary layer height, other relevant boundary layer parameters are calculated.

Table 4.1 details this boundary-layer thickness h along with the displacement thickness, δ^*, momentum thickness, θ, and shape factor, H that are calculated from near-wake measurements of nonporous and porous H1 plates. In addition to the smaller boundary layer height, the porous plates also have smaller displacement and momentum thicknesses. The reduction in boundary-layer height and displacement thickness could help to explain reductions in broadband and tonal noise of the plates, as aeroacoustic theory says that the mean squared sound pressure generated at the trailing edge is proportional to the turbulence scales [11], and the turbulence scales are taken to be proportional to the boundary-layer height. In addition, the higher shape factor measured for the porous plates indicates a condition similar to the effect of a stronger adverse pressure gradient, which could lead to an earlier separation.

Table 4.1: Near-wake boundary layer measurement data for blunt TE nonporous and porous plate H1

Plate	Measurement location	h, mm	δ^*, mm	θ, mm	H
Nonporous	Near wake	6.4	0.79	0.54	1.47
H1 - hole	Near wake - point A	4.6	0.69	0.41	1.70
H1 - gap	Near wake - point B	4.8	0.73	0.43	1.69

Velocity profiles measured at 5 mm upstream from the TE and normalized by the nonporous boundary layer height h_{NP}, at this location, are shown in figure 4.1b. The probe began its measurements at a position 2.5 mm from the plate surface and moves away in the vertical direction. The boundary-layer height for porous plate measured at a hole (point C in figure 2.7b) is 4.9 mm and is 5.0 mm measured at a gap (point D). Finally, the boundary-layer height for the nonporous case is 6.5 mm. Compared to measurements in the near-wake region, the boundary-layer height is slightly larger when measured upstream. This increase in boundary layer height at the location of the pores could support the hypothesis that the pores create additional turbulence. The turbulence intensity profiles are subsequently analyzed to investigate this hypothesis further.

Figure 4.2 displays the turbulence intensity from the same set of measurements as shown in the velocity profile figures for the nonporous (NP) and H1 plate. For both test locations, the near-wake region and upstream of the TE, the turbulence intensity measured close to the porous plate is greater than that of the nonporous plate. In figure 4.2a, the turbulence intensity measured in the near wake behind a hole in the streamwise direction was the greatest. This trend is also seen in the turbulence intensity profiles measured upstream of the TE in figure 4.2b. The higher turbulence intensity near the porous plate surface could help to explain how pores may create excess turbulence, which could in turn explain the excess noise at high Strouhal numbers. Beyond a height of approximately $z/h_{\mathrm{NP}} \approx 0.6$ in both the near-wake and upstream measurement locations, the turbulence intensity of the nonporous becomes greater than that of the porous plate. This result is likely due to the fact that the porous plate BL is smaller, and, at this distance, the probe is starting to move out of the BL and into the freestream. Further information from the hot-wire measurements is gained by analyzing the spectra of the turbulent velocity fluctuations in the following figures.

Figure 4.3 shows contour maps of the spectra of the turbulent velocity fluctuations from the near wake measurements shown in figure 4.1a. These contour maps show $10\log_{10}(\Phi/\Phi_0)$, where Φ is the spectrum of the turbulent velocity fluctuations and $\Phi_0 = 1$ m^{2}s^{-1}. These data are presented in terms of the Strouhal number and measurement position. Within each subfigure, the boundary layer thickness is shown and labeled h_{NP} for the nonporous case and h_{h} and h_{g} for the porous hole and gap measurements, recorded at points (A) and (B) in figure 2.7b respectively. Figure 4.3a shows the results from the nonporous plate, where a significant peak in the turbulence is seen at $St = 0.19$ that is consistent with that of the acoustic peak due to bluntness. This peak is pronounced and dissipates at a distance of approximately $3w$ away from the edge. A resonance of this peak is also seen at $St = 0.38$. Results from the porous plate H1 are shown from measurements taken directly behind a perforation and directly behind a gap between two perforations in figure 4.3b and figure 4.3c, respectively. These measured spectra show a notable lack of a tonal peak at

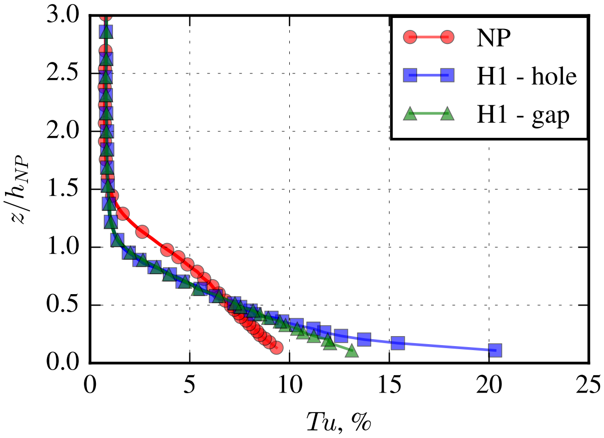

(a)

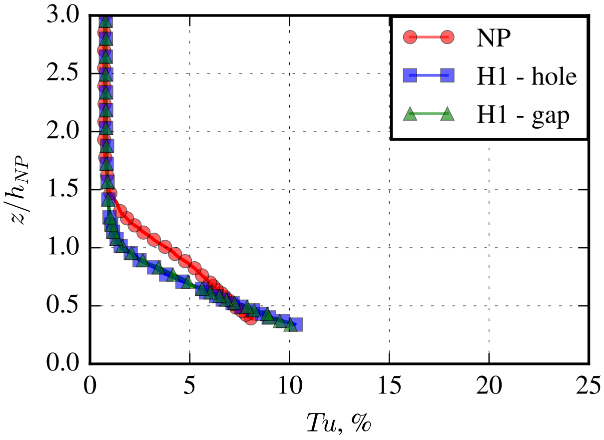

(b)

Figure 4.2: Turbulence intensity profiles at $Re = 3.37 \times 10^5$ from nonporous plate (NP) and H1 plate, measured in the (a) near-wake and (b) upstream of the TE.

$St = 0.19$ when compared to the nonporous plate. However, strong peaks reappear instead at $St = 0.17$ and a harmonic at $St = 0.34$ in both hole and gap measurements about the porous plate. Another interesting feature of the contour plots is a decrease in turbulence intensity at the middle of the plate, $z = -w/2$, which could be due to little or no flow circulation existing in this region directly downstream of the center of the TE.

The downward shift of tonal peaks from $St = 0.19$ (nonporous) to $St = 0.17$ (porous) is seen in the turbulence intensity measured in the wake of the plates and is observed in the acoustic spectra from the plates. However, the acoustic tonal peak is much less pronounced,

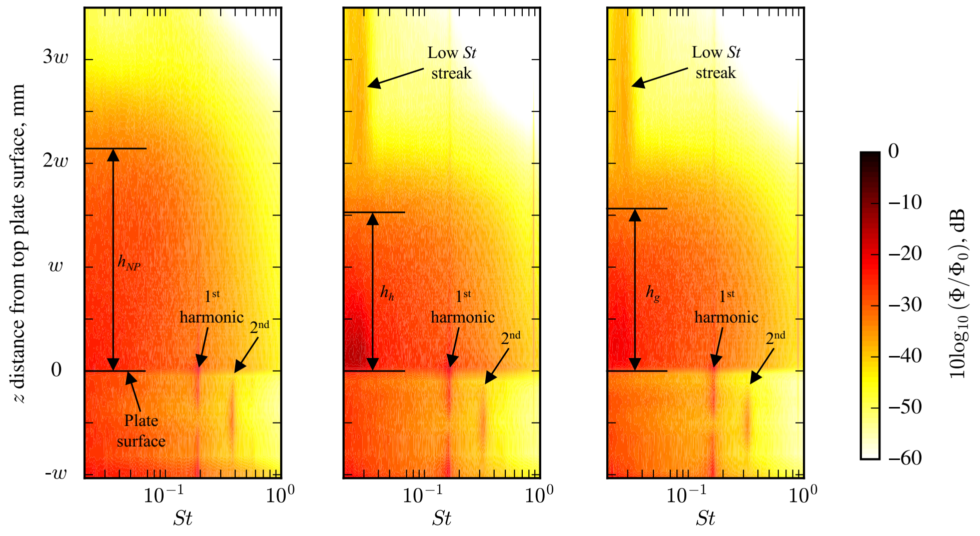

(a) **(b)** **(c)**

Figure 4.3: Spectra of near-wake turbulent velocity fluctuations, for the (a) nonporous plate and (b) porous plate H1 behind hole and (c) behind gap at $Re = 3.37 \times 10^5$.

as it is diminished by the presence of porosity. The measured downward shift could be due to the thinner boundary layer of the porous plate (see figure 4.1) creating and therefore the length scale of the largest turbulent structures being smaller, as well. These results also suggest that the tonal noise might not always scale with a geometric dimension of the plate, but instead the wake vortex shedding could scale on a fluid-dynamic dimension that is yet to be identified. This idea is similar to the findings of a previous experimental work on cylinders in a cross-flow [95], where the wake width was found to be an effective scaling factor. Additional measurements or simulations are necessary to further substantiate this claim.

Figure 4.4 displays contour maps of the turbulent velocity spectra measured upstream from the TE. These measurements began 2.5 mm from the plate surface in the z-direction, and for that reason, the vertical axis is changed from that in figure 4.3. The contour plots from the upstream hot-wire measurements are very similar to those from the near wake measurements. The nonporous plate has an overall larger region of increased turbulence, attributed to the larger boundary layer thickness. However, like in the near wake

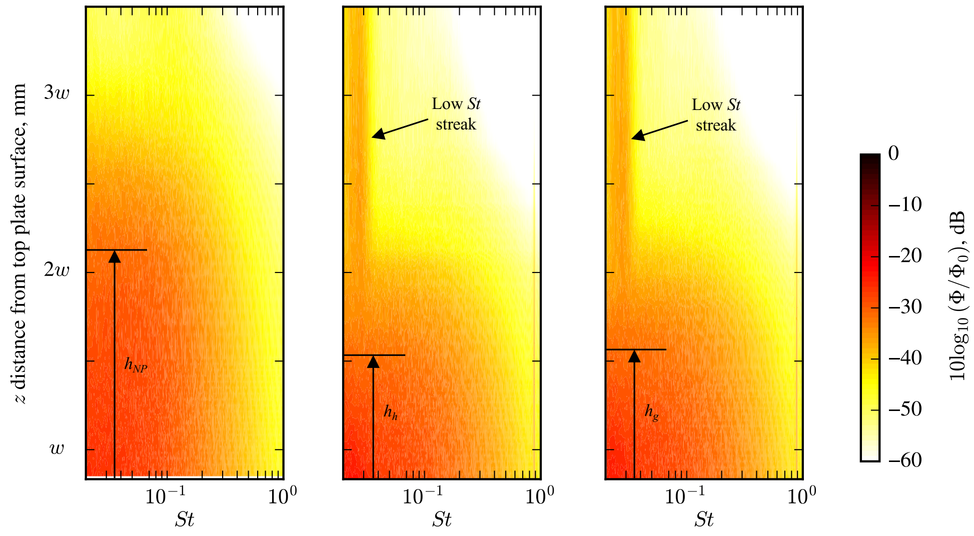

(a) **(b)** **(c)**

Figure 4.4: Spectra of upstream turbulent velocity fluctuations, for the (a) nonporous plate and (b) porous plate H1 behind hole and (c) behind gap at $Re = 3.37 \times 10^5$.

measurements, the porous plates have a region of higher turbulence seen in the range $0.03 < St < 0.04$ which is recorded at all z locations. This corresponds to a frequency of 300 Hz $< f <$ 400 Hz. Interestingly, the acoustic spectra of the porous plates do not contain increases at these frequencies. This excess turbulence could either be not scattered at the trailing edge, or it might not relate to far-field noise in the directivity we are considering. Additional work is necessary to identify the source of this low Strouhal number turbulence present in both the near wake and upstream velocity field of the porous plates. Lastly, the tonal peak due to bluntness vortex shedding at St_{b} seen between $w < z < 2w$ in the near wake measurements is not present in the upstream measurements. The absence of the St_{b} in the upstream velocity spectra helps to confirm that the St_{b} peak in both the acoustic spectra and near-wake velocity spectra is indeed due to vortex shedding occurring in the wake.

4.2 Sharp edges

Hot-wire anemometry tests are also conducted in the near wake and upstream of the TE of the sharp-edged nonporous plate and multiple porous plates at a flow speed of $U = 30$ m/s ($Re = 3.37 \times 10^5$) to investigate the effects of porosity on the flow field. Figure 4.5 presents the velocity profiles measured in the near-wake and upstream of the TE for the nonporous, L1, M1, and H1 plates. For the porous plates in figure 4.5a and figure 4.5b, these measurements are conducted at point A and point C in figure 2.7b, respectively. The plates with sharp TEs are oriented in the setup like in figure 2.2, where the hot-wire measurements are conducted on the side of the plate (left) that is not affected by the one-side sharpening of the TE. As in the velocity profile and turbulence intensity figures for the plates with blunt edges, every other test point is shown and the points are connected with a spline fit to aid in viewing; also, the vertical axis, or distance from the test plate, is normalized by the nonporous boundary layer height, $h_{\mathrm{NP}} = 8.6$ mm. Like the experiments with the blunt-edges plates, the boundary-layer height is largest on the nonporous plate and decreases with an increase in porosity, to $h = 7.8$ mm for the L1 plate, $h = 6.3$ mm for the M1 plate, and $h = 4.7$ mm for the H1 plate. In addition, the boundary-layer displacement thickness (δ^*) and boundary-layer momentum thickness (θ) also decrease with an increase in porosity. These changes, along with changes to the shape factor (H), are detailed in table 4.2.

Table 4.2: Near-wake boundary layer measurement data for sharp TE nonporous and porous plates L1, M1, and H1

Plate	Measurement location	h, mm	δ^*, mm	θ, mm	H
Nonporous	Near wake	8.6	1.55	1.03	1.50
L1 - hole	Near wake - point A	7.8	1.26	0.91	1.38
M1 - hole	Near wake - point A	6.3	0.99	0.70	1.41
H1 - hole	Near wake - point A	4.7	0.63	0.39	1.62

Figure 4.6 plots the turbulence intensity (Tu) against vertical distance for the same set of measurements as featured in figure 4.5. With an increase in porosity comes an increase in the Tu measured closest to the plate's surface in the near wake of the plate (see figure 4.6a). This value is approximately 47% for the nonporous plate and increases to 69% for the porous

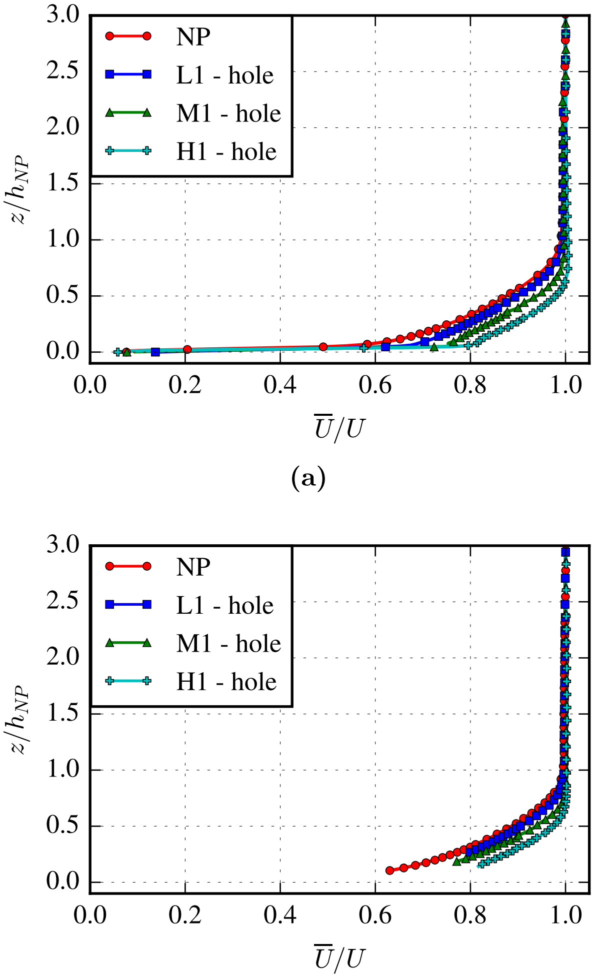

(a)

(b)

Figure 4.5: $\overline{U}/U$ profiles at $Re = 3.37 \times 10^5$ from nonporous plate (NP) and porous plates L1, M1, and H1 measured in the (a) near-wake and (b) upstream of the TE.

plate H1. For the measurements 5 mm upstream of the TE in figure 4.2b, the results are not so clear. It may appear that the Tu is greater for the nonporous case, but this is only because after post-processing of the velocity data, the probe was much closer to the surface than in the case of the porous plates. This is observed in the Tu profile of the nonporous case where the point nearest the $z/h_{\mathrm{NP}} = 0$ is much closer than respective points for the porous plate measurements. Like the hot-wire measurements on the plates with blunt edges, the high turbulence intensity measured on the porous plates supports the theory that the holes themselves increase turbulence and thus increase high-frequency excess noise.

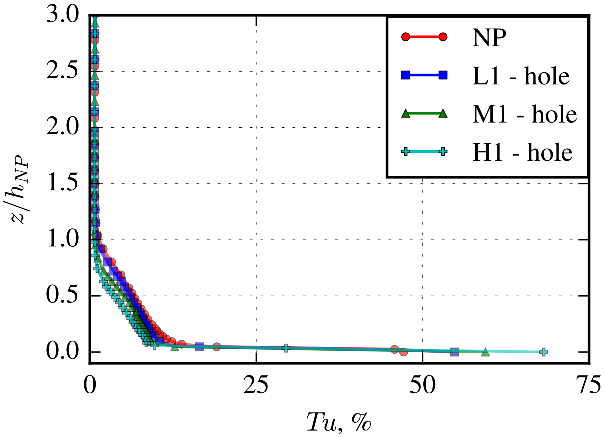

(a)

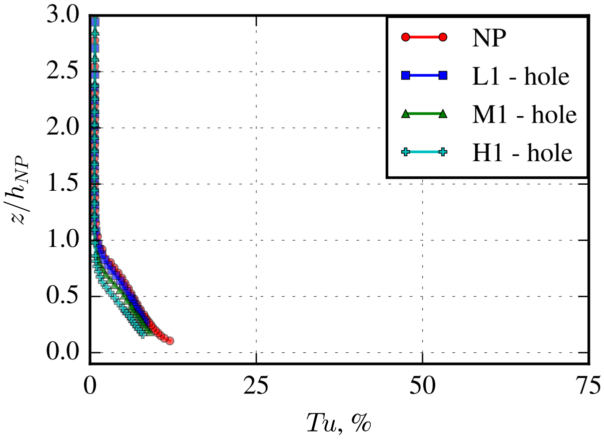

(b)

Figure 4.6: Tu profiles at $Re = 3.37 \times 10^5$ from nonporous plate (NP) and porous plates L1, M1, and H1 measured in the (a) near-wake and (b) upstream of the TE.

To further analyze the effects of the holes on the flow field, figure 4.7 compares the velocity and turbulence intensity profiles measured in the near-wake behind a hole (point A in figure 2.7b) and between a gap between holes (point B in figure 2.7b) for the H1 plate compared to the nonporous reference. For the case of the velocity profile in figure 4.7a, the H1-hole and H1-gap profiles are very similar to each other with like boundary layer heights ($h = 4.7$ mm). Figure 4.6b shows the Tu profiles, where the turbulence intensity measured nearest the plate for the H1-hole and H1-gap profiles are higher than that measured on the nonporous plate. Similar to the velocity profiles, the Tu profiles for the hole and gap loca-

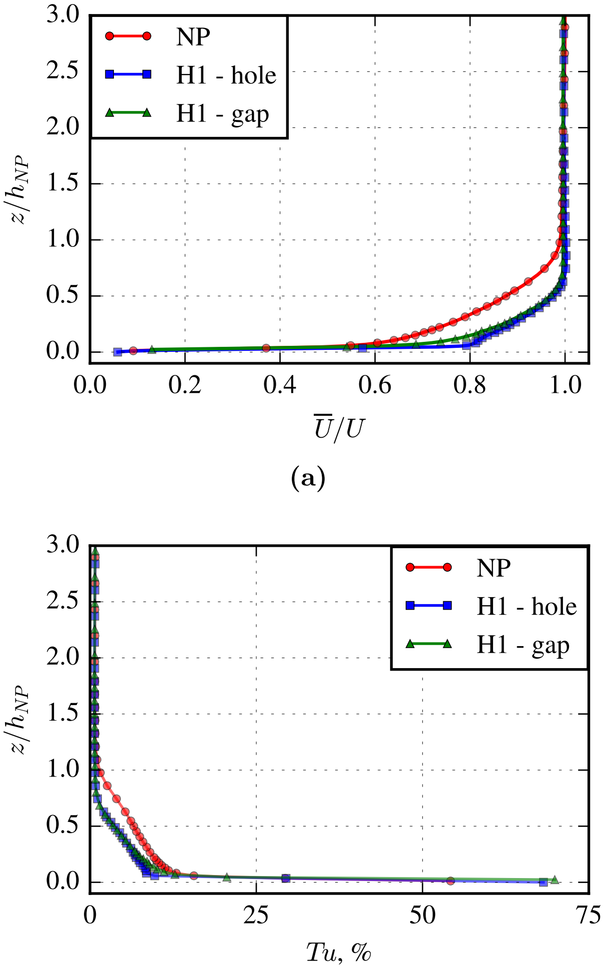

(a)

(b)

Figure 4.7: Comparison of (a) $\overline{U}/U$ and (b) Tu profiles at $Re = 3.37 \times 10^5$ measured in the near-wake for the nonporous plate (NP) and porous plate H1 measured behind a hole (point A in figure 2.7b) and between a gap between holes (point B in figure 2.7b).

tions are very similar to each other, and the maximum value only differs by approximately 2%. The similar velocity and Tu profiles measured in the near-wake of the H1 plate at various locations supports the idea that the boundary layer is uniform across the span of the porous trailing edges.

Lastly, figure 4.8 features contour maps of the spectra of the near-wake turbulent velocity fluctuations shown in figure 4.5a at $Re = 3.37 \times 10^5$ for the nonporous plate compared to the L1, M1, and H1 porous plates measured behind a hole. Like in the contour maps for the

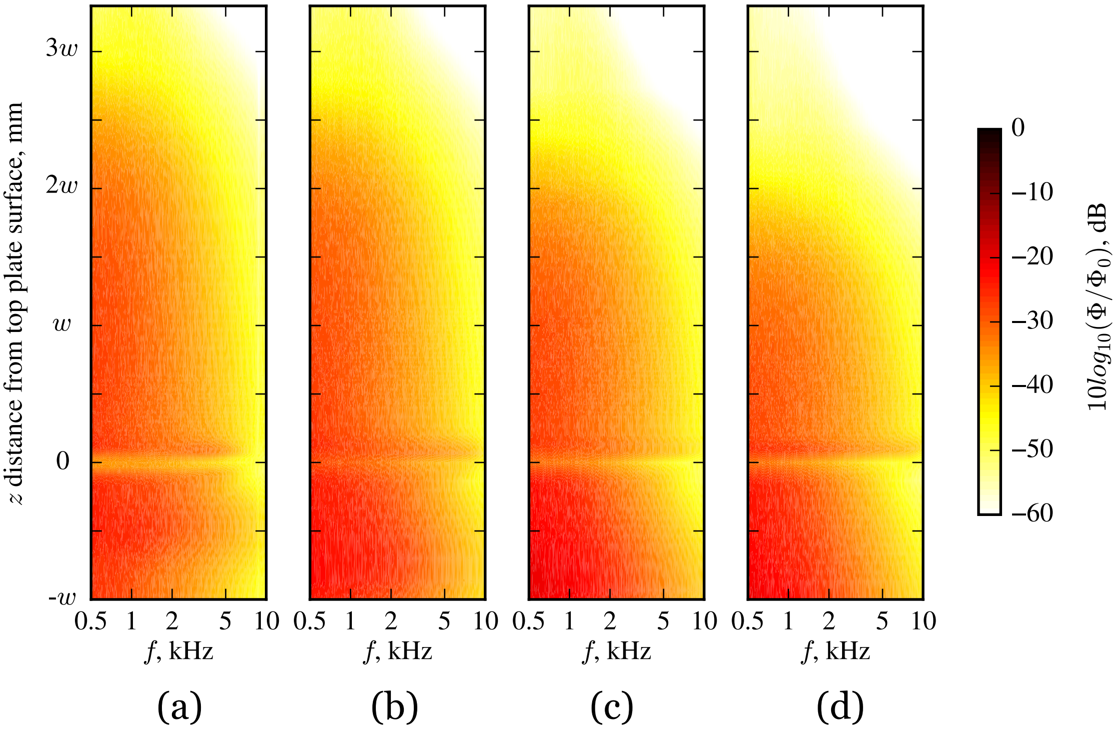

Figure 4.8: Spectra of near-wake turbulent velocity fluctuations at $Re = 3.37 \times 10^5$ for the (a) nonporous plate, (b) L1 porous plate behind hole, (c) M1 porous plate behind hole, and (d) H1 porous plate behind hole.

blunt TE plates, the maps show $10\log_{10}(\Phi/\Phi_0)$, where Φ is the spectrum of the turbulent velocity fluctuations and $\Phi_0 = 1$ m^{2}s^{-1}, and the dynamic range for each subfigure is 60 dB. In these subfigures, the horizontal axis is frequency and the vertical axis is z distance from the top of the plate surface, where w is the plate thickness, 3 mm. The location of $z = 0$ represents the location directly downstream from the top surface of the sharp TE plate. It is clear that at this location for all tested plates, the turbulence intensity is very low as there is little to no flow circulation directly downstream of the TE.

The area of increased magnitude of turbulence velocity fluctuations scales roughly with the boundary-layer height for each test case. Because of this, the nonporous plate has the largest region of increased turbulence intensity (in the range $0 < z < 3w$), and this region shrinks with increasing porosity. Interestingly, the magnitude of Φ within this range is very similar across porosity cases, where the greatest turbulence intensity is seen in the range of

500 Hz $< f <$ 5 kHz at all locations; however, the upper range increases with an increase in porosity. This is likely due to the holes themselves creating increased turbulence. On the side of the plate where the sharpening occurred ($0 < z < -w$), the porous plates have a region of increased magnitude of Φ. Lastly, in a stark contrast to the contour plots from the plates with blunt TEs (see figures 4.3 and 4.4), the contour maps from the plates with sharp TEs are devoid of any tonal content and are broadband in shape, as are the corresponding acoustic spectra (see §3.3). As measurements at the hole and gap are very similar, and the contour maps measured in the near-wake and upstream of the plates with blunt TEs are very similar (see figures 4.3 and 4.4), contour maps are not shown for the upstream measurements and measurements taken in the gap regions for the plates with sharp TEs.

4.2.1 Effects of hole fillet on the flow field

The effects of hole fillets on the flow field are investigated in an attempt to mitigate excess high-frequency noise created by the porous plates. The following figure 4.9 presents velocity and turbulence intensity profiles for the nonporous plate compared to the baseline H1 plate and H1a and H1c plates with filleted through-holes. The boundary layer height on the H1c plate is much greater than that of the H1 and H1a plates (which are smaller than that of the nonporous plate). In addition, the turbulence intensity of the H1c plate is much higher than all other plates at all locations. The elevated Tu and larger boundary layer could result in the overall higher magnitude of sound generated by the H1c plate at all frequencies in §3.3.1.4. The exact mechanism by which the plate with the largest hole fillet, H1c, creates a larger boundary layer and excess turbulence is unknown. Interestingly, the H1a plate has a lower turbulence intensity near $z/h_{\text{NP}} = 0$ in figure 4.9b, which could explain how the H1c plate creates less high-frequency excess noise compared to the baseline H1 plate.

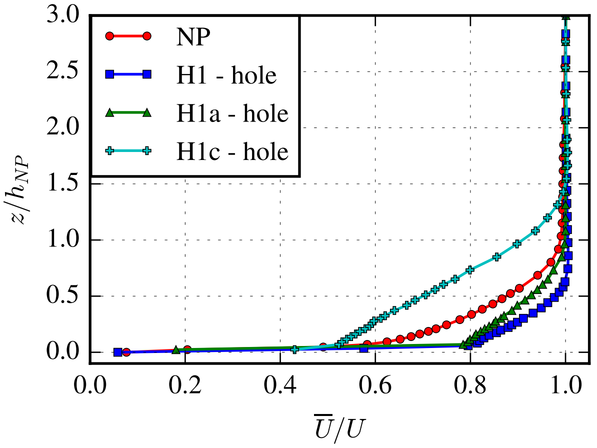

(a)

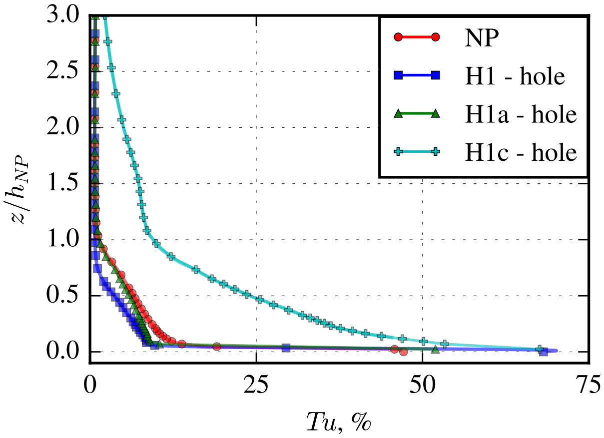

(b)

Figure 4.9: Effect of hole fillet on the (a) $\overline{U}/U$ and (b) Tu profiles at $U = 30$ m/s ($Re = 3.37 \times 10^5$) measured in the near-wake for the nonporous plate (NP) and porous plates H1, H1a, and H1c measured behind a hole (point A in figure 2.7b).

4.3 Summary

In summary, hot-wire measurements are conducted in the flow field of plates with blunt and sharp TEs from WTC-1 in the BTU wind tunnel. Measurements are taken 1 mm downstream (in the near-wake) and 5 mm upstream of the TE. Velocity profiles, turbulence intensity profiles, and contour maps of the spectra of turbulent velocity fluctuations at $U = 30$ m/s ($Re = 3.37 \times 10^5$) are presented.

In the measurements with both blunt and sharp TEs, the porous plates' boundary layer heights are smaller than those of the nonporous, similar to previous experimental investigations of a grazing flow over a permeable wall [96]. There is also an increase in turbulence intensity for the porous plates, especially close to the plate surface. The results are very similar for the measurements downstream of a hole and downstream of a solid surface (gap) between two holes of the porous plates, which suggest that the boundary layer is essentially uniform in the spanwise direction. While the measurements of the plates with sharp TEs show broadband frequency content in the spectra of turbulent velocity fluctuations, measurements from the flow fields of the nonporous plate with a blunt TE indicate tonal vortex shedding at the Strouhal number associated with bluntness-induced vortex shedding ($St_{\mathrm{b}} \approx 0.2$), which is the same Strouhal number of bluntness-induced vortex shedding from the acoustic measurements. Porous plates with blunt edges are shown to reduce the magnitude of the spectra at this St_{b}, even shifting it downwards. This downward shift is theorized to be related to the thinning of the boundary layer, as the length scales of the turbulent structures are decreased. These results also suggest that the tonal noise might scale with a wake dimension that is not yet identified. Also, the perforations on the plate act as a pressure release that leads to decreased turbulence intensity when moving farther away from the plate and to a shift of the tonal vortex shedding peak. These results motivate future investigations to resolve the mechanisms leading to the downward shift of the bluntness-induced vortex shedding peak in the turbulence spectra.

Lastly, the hot-wire measurements on the plates with sharp TE consisted of measurements on the L1, M1, and H1 porous plates. With an increase in porosity came a decrease in the boundary-layer height, displacement thickness, and momentum thickness. Additionally, with increasing porosity came increasing turbulence intensity near the plate surface, supporting the idea that the pores themselves create additional turbulence which could cause the high-frequency excess noise generated by the porous plates. The plate with the largest hole fillet created excess turbulence compared to the porous non-filleted baseline; however, a smaller hole fillet radius leads to less turbulence intensity at the plate surface compared to the baseline, which could result in the lesser high-frequency excess noise relative to the baseline porous plate in §3.3.1.4.

Chapter 5

Surface pressure level fluctuations on a glider with porous trailing edges

Velocity data and surface pressure level spectra from the glider measurements described in §2.2.3 are presented and discussed in this chapter. Surface pressure level spectra are measured using a flush-mounted microphone located on the fuselage and a microphone located at the trailing edge, and flight speed data of the glider is synchronously captured using a pitot-tube velocity sensor.

5.1 Flight speed measurement

Flight speed data are first examined to determine suitable time periods of relatively steady flight to analyze surface pressure spectra. Figure 5.1 presents flight speed history of a representative flight. The total time frame presented in figure 5.1a encompasses take-off, steady flight, and landing. Take-off occurs during 0 s $< t <$ 2.5 s and is characterized by a very noisy signal. This issue is discussed in §2.2.3 and results from the active propeller located upstream of the pitot tube. The steady flight period occurs at approximately

2.5 s $\leq t < 11$ s once the propeller is switched off. Figure 5.1b highlights the time period of steady flight which fluctuates around $U \approx 10$ m/s which is an example of a time period from which microphone data are processed. At $t \geq 11$ s, the velocity signal contains significant measurement noise during vehicle deceleration in all tests. This time period was cross-checked with hand-timers on the ground to confirm that it corresponds to the glider's descent and landing phase.

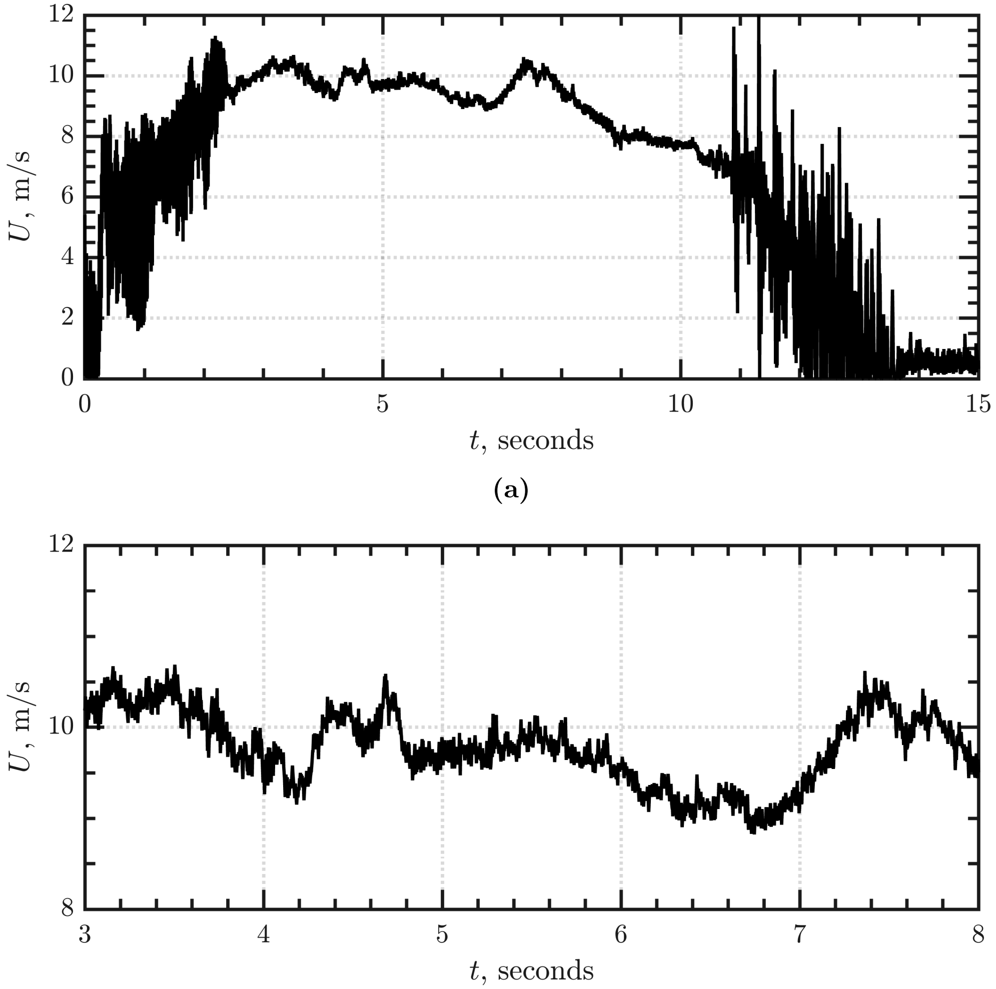

(a)

(b)

Figure 5.1: Glider flight history for (a) entire flight and (b) steady flight excerpt at $U \approx 10$ m/s for a representative flight.

5.2 Surface pressure dependence on porosity parameter

Surface pressure level spectra are presented and discussed for the microphone on the wing and fuselage of the glider. The glider is tested with a nonporous reference edge (NP) and three porous edge designs: circular holes (P1), rectangular slits (P2), and square holes (P3). The plates have porosity parameter values $\delta > 10$ at approximately $f \leq 1.6$ kHz, and further design details of these plates are discussed in §2.1.3. In this chapter, SPL refers to *surface* pressure level(s); in all other results chapters SPL refers to *sound* pressure level(s). Calculated in the same way as sound pressure level spectra (see §2.2.1.1), the magnitude of the surface pressure level spectra is significantly higher than sound pressure level spectra. This difference is because the flush mounted microphones in the glider setup measure changes in surface pressure which, by the presence of a boundary layer, is many orders of magnitudes stronger than that of acoustic pressure.

Figure 5.2 compares the average SPL against frequency for the four tested edges; here, the SPL for each edge condition comes from an average of all the SPLs from all flights (with that edge), where flight speeds ranged between 7 m/s $< \overline{U} <$ 12 m/s. The average velocity for each edge design of the many flights considered was approximately $U \approx 10$ m/s. The averaging procedure reduces the overall effect of flight speed fluctuations on the measured surface pressure levels.

Recall that P1, P2, and P3 have the same estimated porosity parameter value, yielding $\delta > 10$ at approximately $f > 1.6$ kHz. The P1 and P3 porous plates increase the magnitude of the SPL spectra (up 17 dB) measured on the wing at all frequencies (see figure 5.2a). The P2 behaves similarly to the NP plate but reduces the SPL spectra magnitude by up to 2.5 dB in the frequency range 1 kHz $< f <$ 3 kHz and only increases noise in the frequency range 3.5 kHz $< f <$ 6kHz by up to 2.5 dB. While these values are small, they are outside of the range of uncertainty of the power-spectral density calculation (±0.4 dB). Figure 5.2b presents the SPL spectra from the microphone on the fuselage. Here, the porous plates P1 and P3 have very little effect on the spectra with the exception of an increase in the P1 spectra at frequencies 3 kHz $< f <$ 6 kHz. However, the P2 plate has a much greater affect

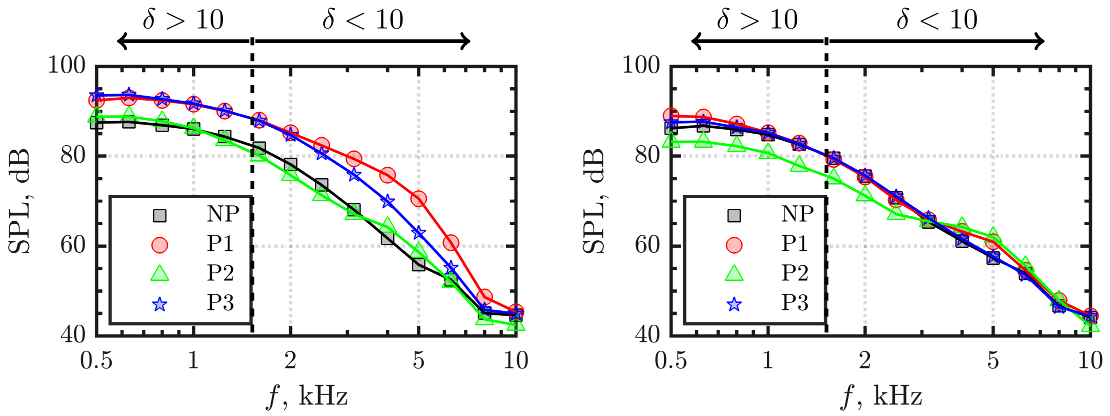

(a) Wing trailing edge

(b) Fuselage

Figure 5.2: Averaged SPL spectra for the nonporous (NP) and porous (P1, P2, and P3) flat plates from multiple runs, where $\overline{U} \approx 10$ m/s: (a) microphone on the wing trailing edge; (b) microphone on the glider fuselage. The highly-porous parametric limit is achieved for $\delta \gtrsim 10$.

on the spectra, where magnitudes in the frequency range 500 Hz $< f <$ 3 kHz are reduced by up to 5 dB with a small increase in noise at frequencies $f >$ 3 kHz (up to 3 dB).

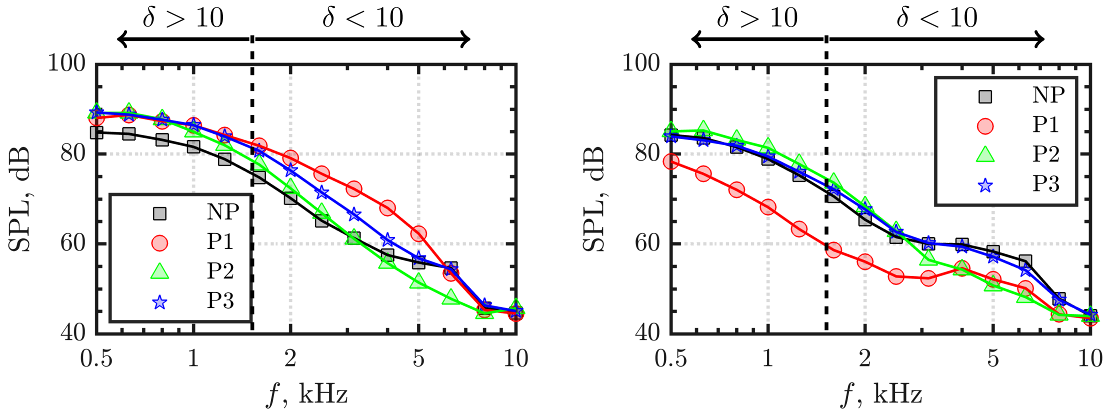

(a) Wing trailing edge

(b) Fuselage

Figure 5.3: SPL against frequency for the nonporous (NP) and porous (P1, P2, and P3) flat plates from single runs for each test plate, where $U \approx 7$ m/s: (a) microphone on the wing trailing edge; (b) microphone on the glider fuselage. The highly-porous parametric limit is achieved for $\delta \gtrsim 10$.

The results for individual flights at specified flight speeds are now presented in figure 5.3 and figure 5.4, which are compared and contrasted to the averaged results in figure 5.2.

Figure 5.3 shows SPL comparisons measured onboard the glider while flying at a low velocity of $U \approx 7$ m/s. Similarly to the results in the average SPLs (in figure 5.2) calculated from the wing microphone, the P1 and P3 plate increases levels (up to 10 dB and 5 dB, respectively) at all frequencies except for high frequencies ($f > 6$ kHz) where they are the same level as the nonporous edge. Interestingly, at this low flight speed, the P2 plate reduces levels on the wing in the frequency range $f > 3$ kHz (by up to 6 dB) and increases noise at low frequencies ($f < 3$ kHz) by up to 5 dB. The results from the microphone on the fuselage in figure 5.3b show SPLs are reduced by up to 20 dB and 10 dB across the entire frequency range by porous plates P1 and P2, respectively. The surface pressure levels recorded on the fuselage with the porous plate P3 installed show little change ($<$ 2 dB at all frequencies) compared to the nonporous edge.

A similar comparison of surface pressure levels recorded during individual flights at $U \approx 10$ m/s is shown in figure 5.4. At this higher speed, the microphone on the wing shows increases in SPLs (up to 20 dB) across the entire frequency range by the porous plates. The microphone on the fuselage tells a different story, where P2 plate reduces levels by up to 8 dB in the frequency range 500 Hz $< f <$ 5 kHz, and plates P1 and P3 increase levels up to 5 dB at all frequencies. The reductions in surface pressure levels by the P2 plate at this higher flight speed warrants future investigations into whether the pressure level decreases are also seen in the acoustic far field. The following section describes attempts to correlate pressure fluctuations on the wing to those measured on the fuselage.

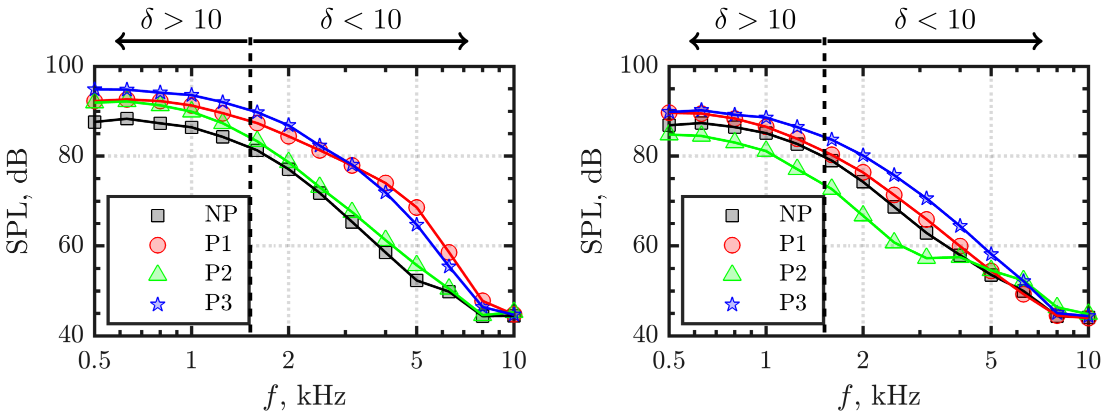

(a) Wing trailing edge

(b) Fuselage

Figure 5.4: SPL against frequency for the nonporous (NP) and porous (P1, P2, and P3) flat plates from single runs for each test plate, where $U \approx 10$ m/s: (a) microphone on the wing trailing edge; (b) microphone on the glider fuselage. The highly-porous parametric limit is achieved for $\delta \gtrsim 10$.

5.3 Coherence between wing and fuselage microphone signals

The magnitude-squared coherence of the microphone surface pressure signals measured on the wing and fuselage of the glider are calculated using (2.10) and is a measure of the accuracy of the assumed linear input/output model of two signals [76]. Figure 5.5 presents the magnitude-squared coherence estimated between the wing and fuselage microphone signals as recorded during the time frame presented in figure 5.1b. In general, the $\gamma_{ab}^2 < 0.5$ for most of the frequency range of interest (500 Hz$< f <$ 10 kHz), and in the frequency range 500 Hz $< f <$ 2 kHz, where some porous plates reduce surface pressure levels, it is near zero. The overall low coherence between the two microphone signals is likely due to the fact that the pressure fluctuations at each location due to the boundary layer are random and have a much higher magnitude that acoustic pressure fluctuations.

The overall low coherence of the onboard microphone signals in figure 5.5 is further support that future testing should include far field pressure measurements where the setup should be designed such that the boundary layer would not affect the microphone signals.

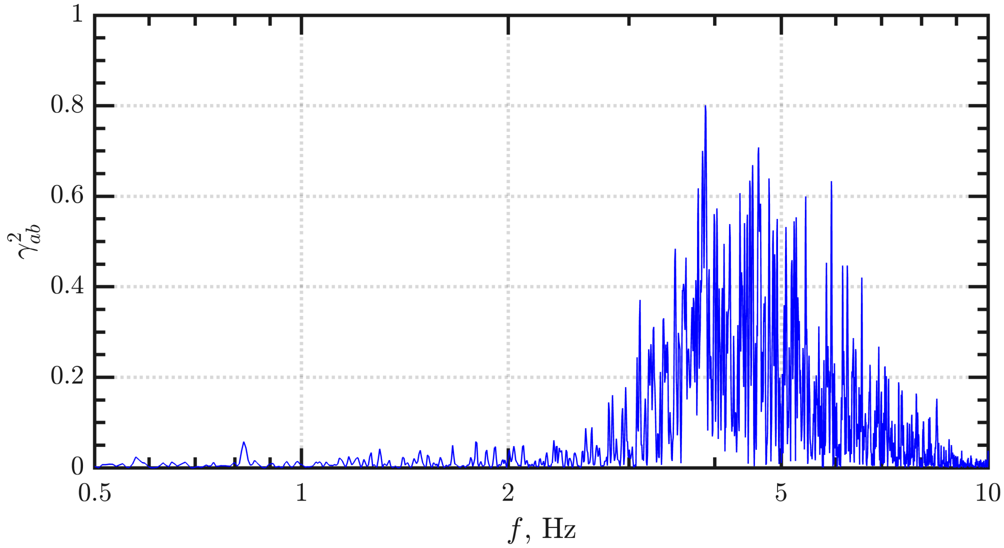

Figure 5.5: Magnitude-squared coherence of the microphones on-board the glider with the nonporous edge installed in a representative test at $U \approx 10$ m/s.

5.4 Summary

This chapter presented results from a remote-controlled glider outfitted with porous edges in an attempt to reduce flow noise by owl-inspired trailing-edge porosity. To the author's knowledge, this is the first time porous edges have been tested on a flight vehicle outfitted for onboard velocity and acoustic measurements. Sample velocity data show a noisy signal during take-off and landing phases of the glider, and the steady flight period between these two events is used as the time frame from which acoustic data are analyzed. Surface pressure level spectra are measured from microphones flush-mounted at the trailing edge of the wing and on the fuselage in line with the trailing edge in the spanwise direction. In the acoustic far-field measurements in §3, changing the shape of the holes did not have significant effects on the spectra; however, the changing the hole shape of the porous plates P1, P2, and P3 (all of the same porosity parameter value) on the remote-controlled glider did lead to significant changes in the measured surface pressure levels. Surface pressure levels (SPLs) are presented as either the average of many flights or representative individual flights at each porosity condition. For the average SPLs measured by the wing microphone, the P2 plate modestly reduces these levels by up to 2.5 dB; however, the other porous plates increase levels across all frequencies. For this same set of averaged results, the porous plates have a minor effect on the SPL measured on the fuselage, where only the P2 plate can reduce levels by up to 5 dB at frequencies $f < 3$ kHz. Results from the wing microphone from individual flights for each test edge at the low velocity ($U = 7$ m/s) indicate that the porous plate designs have a significant effect on the surface pressure fluctuations: the P2 plate reduces levels up to 6 dB, and the P1 and P3 plates behave similarly to the NP plate. To the contrary, porous plate P1 and greatly reduces individual surface pressure levels at all frequencies on the fuselage for this low flight speed (up to 20 dB). For the individual flights at the higher flight speed, $U = 10$ m/s, the porous plates increase SPLs recorded on the wing by up to 20 dB, and only the porous plate P2 can reduce levels on the fuselage by up to 8 dB. Lastly, the low magnitude-squared coherence measured between the microphone signals at the wing and fuselage suggests they are not closely related, a result which is likely due to the random nature of boundary layer pressures, the main contributor to the surface pressure levels.

Elevated surface pressure levels are seen at high frequencies, which could be due to the porous plates or unknowns of the measurement producer. It is likely that the holes/porosity itself is responsible for the increase in levels, as the presence of holes is likely generating excess turbulence (see §4), which leads to greater pressure fluctuations in the boundary layer. In addition to the holes/porosity creating excess "noise," it is likely that microphone placement greatly affects the measured sound pressure levels. It is further expected that there could be significant excess noise created due to flow through the porous trailing edge, as the pores are relatively large compared to those in the wind tunnel measurements, and the porous TE has a hollow area in between the porous plates, which could lead to flow circulation within this large gap. Also, while the pitot tube data allows for an estimation of the period of steady flight, controlled steady flight cannot be confirmed without an accelerometer on board. Therefore, in any test, the glider could be experiencing a non-zero angle-of-attack, which may incur changes to the surface pressure levels, even when at steady velocity levels seen in figure 5.1b. This challenge highlights the importance of using many averages when using this setup. Hence, the averaged results in figure 5.2 over many flights with the same edge conditions are conservative yet presented with greater confidence than the figures comparing SPLs from single flights, which are subject to greater flight-to-flight variation.

These measurements demonstrate surface pressure level reductions can be achieved by owl-inspired porous edges to affect self-noise perception on a flying vehicle, and motivate future work that could connect these changes to surface pressure levels to changes in the acoustic far field.

Chapter 6

Conclusions

This dissertation reports multiple experimental campaigns to investigate the effect of owl-inspired porous trailing edges to mitigate flow-borne noise. To this end, the acoustic and aerodynamic flow fields of various lifting surfaces are measured near porous flat plates and porous flat plate extensions to a NACA 0012 airfoil. These laboratory experiments motivate an exploratory study of the potential for owl-inspired porous trailing-edge noise reduction on a remote-controlled glider aircraft. The flow noise generation mechanisms of interest are trailing-edge bluntness noise and turbulent-boundary layer trailing edge noise. The presence of porosity is characterized by a dimensionless parameter δ that arises in the analysis of turbulence scattering by porous surfaces [17] and edges [12]. This parameter is adapted and examined in the present work as a common basis to inform the experimental design and interpret flow noise generated by a turbulent boundary layer over porous edge.

6.1 Research summary

Acoustic and flow measurement of porous plates with blunt trailing edges

- The effect of edge porosity on bluntness-induced vortex-shedding noise and turbulent boundary-layer trailing-edge noise is investigated using a series of perforated flat plates in the Brandenburg University of Technology's aeroacoustic wind tunnel (WTC-1).

Acoustic measurements are conducted using two microphone arrays, and flow measurements are conducted near the plates using hot-wire anemometry. Multiple plates with different hole shapes and spacings are tested, yielding different values of the dimensionless porosity parameter that span from the nonporous to highly porous range. At great values of this parameter achieved by increasing the open-area fraction low-frequency noise and the tonal bluntness-induced vortex-shedding noise are monotonically reduced by up to 10 dB and 16 dB, respectively. Plates operating in the highly-porous regime effectively remove the tonal peak from the acoustic spectra. Interrogation of the flow field near the plates with hot-wire anemometry reveals that the presence of porosity leads to a reduction in boundary-layer height but an increase in turbulence intensity near the plate surface, which is thought to lead to high-frequency excess noise in the far-field. Despite the excess noise created by the presence of the holes, the porous plates can reduce overall sound pressure levels by up to 4 dB. In general plates of the same grouping of porosity level (low, medium, and high) perform similarly; however, plates with circular holes reduce low-frequency noise more and increasing high-frequency less by marginal amounts than plates of the same porosity level with square holes.

- The effect of porosity on bluntness-induced vortex-shedding noise and trailing-edge turbulent boundary-layer noise is investigated using porous flat-plate extensions to a NACA 0012 airfoil in the anechoic wind tunnel at the University of New South Wales (WTC-2). Acoustic measurements are conducted using a 65-microphone array. Similar to the acoustic results in WTC-1, an increase in the dimensionless porosity parameter reduces the bluntness-induced vortex-shedding tonal peak by up to 13 dB. However, unlike in the measurements in WTC-1 where the holes span the entire chord, frequencies below this tonal peak are not affected by the presence of porosity. The lack of low-frequency noice reductions by the porous trailing-edge extensions suggests that the amount of porous chord greatly affects the noise reducing ability. The porous plates in WTC-2 also exhibit excess noise at high frequencies. Plates with spanwise-varying hole spacings reduce the tonal peak slightly better than plates with uniform hole spacings and increase the high-frequency excess noise the least.

Effect of the presence of porosity on plates with sharp trailing edges on the acoustic and flow field

- The effect of porosity on trailing-edge turbulent boundary-layer noise is investigated through perforated flat plates with sharp trailing edges in the Brandenburg University of Technology's aeroacoustic wind tunnel in WTC-1. These are the same set of plates as in the section with blunt trailing edges, but the trailing edges are sharpened to remove the bluntness-induced tonal vortex-shedding noise. DAMAS beamforming is used to integrated noise from specific regions of the plates. Broadband noise is reduced by up to 20 dB at frequencies $f < 2$ kHz in the trailing-edge and leading-edge regions. At frequencies $f > 2$ kHz, the porous plates increase noise by up to 20 dB. Beamforming also reveals that the middle region of the porous plates contribute to the high-frequency excess-noise, strengthening the hypothesis that the holes create this noise. As in the hot-wire measurements of the same set of plates but with blunt trailing edges, the presence of porosity significantly increases the turbulence intensity at the surface of the plates. This increase in turbulence intensity by the holes is thought to lead to the increased noise at high frequencies. Unlike the measurements of the plates with blunt edges, no tonal peaks are found in the acoustic and turbulent velocity fluctuation spectra. Modifications of the plate to have a smaller percentage chordwise porous extent lead to less high-frequency noise due to fewer holes acting as noise sources, but at the cost of less reductions at low frequencies. While most of the measurements are conducted at zero angle-of-attack, select acoustic measurement conducted at low angles of attack show greater reductions in low-frequency noise than at zero angle-of-attack, but at the cost of more high-frequency excess noise. Lastly, plates with small fillets of the holes may lead to greater reductions in noise at low frequencies.

Effect of the presence of porosity on local surface pressure level fluctuations on the control surfaces of a remote-controlled glider aircraft

- A remote-controlled glider is outfitted with an onboard pitot tube and microphones capture velocity and acoustic data synchronously. The microphones are mounted flush on the fuselage near the wing and on the trailing edge of the wing. A control surface of the glider is replaced with an interchangeable trailing edge, through which a nonporous and various porous plate designs are tested to measure their effect on surface pressure level fluctuations on-board the aircraft. The porous plates are designed to meet the high-porosity parameter limit of δ at frequencies approximately $f < 1.6$ kHz. Most of the tested porous designs lead to an increase in the surface pressure level fluctuations on the wing when averaged over multiple flights. The cause of this increase is likely due to surface porosity creating excess turbulence, as is seen in the WTC-1 measurements on the porous flat plates. Two of the porous designs lead to similar average surface pressure level fluctuations on the fuselage as compared to the nonporous edge, and the P2 edge is shown to marginally reduce average levels on the fuselage. Analysis of microphone data from individual flights with each edge condition at similar flight speeds indicate the porous edges can reduce surface pressure level fluctuations on the wing and fuselage; however, these measurements are less reliable due to fewer averages and shorter time periods of microphone data analysis.

6.1.1 Major results

Surface perforations affect the acoustic field by broadly reducing low-frequency and tonal bluntness-induced noise. Perforations are also shown to increase noise at high-frequencies which is hypothesized to be generated by the holes themselves, which is similar to other claims that porosity leads to high-frequency roughness noise [14, 42–44, 55]. The presence of perforations also leads to thinner boundary-layer heights, displacement thicknesses, momentum thicknesses, and to a larger shape factor.

The dimensionless porosity parameter δ is demonstrated to be an able metric to anticipate the behavior of sound generated by a turbulent boundary passing over a porous edge. In general, higher values of this parameter lead to reductions in at low-frequency flow noise, as well as to anticipate reductions in tonal bluntness vortex-shedding noise. While most reductions in flow noise are observed in the high-porosity asymptotic limit of δ, a negative consequence is the generation of excess noise, e.g. within 3 kHz $< f <$ 4 kHz or where the parameter is still in the high-porosity limit ($\delta \gtrsim 10$) for some test cases. This sound is thought to be due to the self-noise mechanisms of the holes occurring at these frequencies.

In general, changes to the pore shape or distribution do not have significant effects on the acoustic and hydrodynamic fields when the porosity parameter is held fixed and for wavelengths much larger than the characteristic size of the holes. For example, plates with circular holes in WTC-1 can reduce bluntness-induced and low-frequency noise by approximately just 2 dB more than their counterparts with square holes. The similar acoustic performance of plates of the same value of the group δf supports the idea that the porosity parameter (and not pore shape or distribution) is the determining metric to anticipate changes in flow noise generated by the turbulent boundary layer.

Lastly, porosity as a passive noise-control method is demonstrated on a remote-controlled glider. Surface pressure fluctuation levels averaged over several flights indicate that select porous designs can reduce these levels in low-frequency ranges on the wing and on the fuselage of the aircraft. However, results from individual flights indicate that the test environment could have significant effects on the measure surface pressure levels, where angle-of-attack and wind gusts may lead to unreliable measurements. These results suggest that the far-field noise may also be reduced in select frequency ranges when applied to aerial vehicles, and suggestions for future experiments to explore this research objective are discussed.

6.2 Future work

Continued research efforts could help to answer remaining and new questions revealed in this work to achieve the goal of the application of porosity to wind turbines, engine rotorfans, and airplanes for flow-noise reductions. A significant drawback of the use of porosity in this dissertation is the characteristic increase in high-frequency noise, which increases as the open-area fraction of the porous plates increases. While the present work found that changes to pore shape and spacings do not have significant changes ($>$ 2 dB for plates of the same porosity parameter value) effects on this high-frequency noise, the size of the holes was not varied in this study. In principle, the porosity parameter δ could be fixed and the hole size and spacing could be changed to test the effect of the size and therefore number of holes on the high-frequency excess noise. In addition, numerical simulations similar to in Jiang et al. [58] could be conducted to further investigate the mechanisms responsible for high-frequency excess noise seen on the flat plates. This work could lead to a model to gain a better understanding of the cross-over frequency at which porous plates create excess noise.

Additionally, all of the work conducted in this dissertation involves porous designs where the perforations are on flat plates or flat-plate extensions. Experimental measurements on airfoil models with similar holes and spacings could test the effect of a pressure and suction side on both the acoustic and flow field of perforated airfoils; these results could then be compared against the results from other campaigns which investigated the use of porous foams to reduce flow noise. A possible link between porosity with perforations and foam materials could then be investigated.

Lastly, a larger experimental campaign focused on demonstrating owl-inspired noise reductions on a flying vehicle should involve greater control of the experiment by implementing measures to maintain steady flight speeds and orientation of the aircraft, and future testing should include far-field acoustic measurements. This effort should be accomplished with onboard accelerometers and automated flight controls in addition to synchronous acoustic measurements in the form of a microphone array in the acoustic far field.

Bibliography

[1] W. K. Blake. *Mechanics of Flow-Induced Sound and Vibration, Volume 2: Complex Flow-structure Interactions*. Academic Press, 2017.

[2] T. F. Brooks, D. S. Pope, and M. A. Marcolini. Airfoil self-noise and prediction. Technical Report 1218, NASA Langley Research Center, 1989.

[3] W.K. Blake. *Mechanics of Flow-Induced Sound and Vibration, Volume 1: General Concepts and Elementary Sources*. Academic Press, 2017.

[4] J. W. Jaworski and N. Peake. Aeroacoustics of silent owl flight. *Annual Review of Fluid Mechanics*, 52(1):395–420, 2020.

[5] L. Leylekian, M. Lebrun, and P. Lempereur. An overview of aircraft noise reduction technologies. *Aerospace Lab*, 6:1–15, 2014.

[6] J. G. Schepers, A. P. W. M. Curvers, S. Oerlemans, K. Braun, T.H. Lutz, A. Herrig, W. Wuerz, A. Mantesanz, L. Garcillan, M. Fischer, et al. SIROCCO: Silent rotors by acoustic optimisation. In *Second International Meeting on Wind Turbine Noise*, 2007.

[7] D. Schreckenberg, M. Meis, C. Kahl, C. Peschel, and T. Eikmann. Aircraft noise and quality of life around Frankfurt Airport. *International Journal of Environmental Research and Public health*, 7(9):3382–3405, 2010.

[8] A. Bauranov and J. Rakas. Designing airspace for urban air mobility: A review of concepts and approaches. *Progress in Aerospace Sciences*, 125, 2021.

[9] E. Sarradj, C. Fritzsche, and T. F. Geyer. Silent owl flight: bird flyover noise measurements. *AIAA Journal*, 49(4):769–779, 2011.

[10] A. Powell. On the aerodynamic noise of a rigid flat plate moving at zero incidence. *Journal of the Acoustical Society of America*, 31(12):1649–1653, 1959.

[11] J. E. Ffowcs Williams and L. H. Hall. Aerodynamic sound generation by turbulent flow in the vicinity of a scattering half plane. *Journal of Fluid Mechanics*, 40(4):657–670, 1970.

[12] J. W. Jaworski and N. Peake. Aerodynamic noise from a poroelastic edge with implications for the silent flight of owls. *Journal of Fluid Mechanics*, 723:456–479, 2013.

[13] M. S. Howe. A review of the theory of trailing edge noise. *Journal of Sound and Vibration*, 61(3):437–465, 1978.

[14] T. F. Geyer and E. Sarradj. Trailing edge noise of partially porous airfoils. In *20th AIAA/CEAS Aeroacoustics Conference*, 2014. AIAA Paper 2014-3093.

[15] H. Chen, Z. W. Yoas, J. W. Jaworski, and M. H. Krane. Acoustic emission of a vortex ring near a porous edge. Part 1: theory. *Journal of Fluid Mechanics*, 941, 2022. A28.

[16] T. Kambe, T. Minota, and Y. Ikushima. Acoustic wave emitted by a vortex ring passing near the edge of a half-plane. *Journal of Fluid Mechanics*, 155:77–103, 1985.

[17] J. E. Ffowcs Williams. The acoustics of turbulence near sound-absorbent liners. *Journal of Fluid Mechanics*, 51(4):737–749, 1972.

[18] D. G. Crighton and F. G. Leppington. Scattering of aerodynamic noise by a semi-infinite compliant plate. *Journal of Fluid Mechanics*, 43(4):721–736, 1970.

[19] A. Vathylakis, T. P. Chong, and P. F. Joseph. Poro-serrated trailing-edge devices for airfoil self-noise reduction. *AIAA Journal*, 53(11):3379–3394, 2015.

[20] S. R. Koh, M. Meinke, and W. Schröder. Numerical analysis of the impact of permeability on trailing-edge noise. *Journal of Sound and Vibration*, 421:348–376, 2018.

[21] R. R. Graham. The silent flight of owls. *Aeronautical Journal*, 38(286):837–843, 1934.

[22] B. Lyu, L. J. Ayton, and P. Chaitanya. On the acoustic optimality of leading-edge serration profiles. *Journal of Sound and Vibration*, 462, 2019.

[23] S. Narayanan, P. Chaitanya, S. Haeri, P. Joseph, J. W. Kim, and C. Polacsek. Airfoil noise reductions through leading edge serrations. *Physics of Fluids*, 27(2):025109, 2015.

[24] P. Chaitanya, P. Joseph, S. Narayanan, C. Vanderwel, J. Turner, J. W. Kim, and B. Ganapathisubramani. Performance and mechanism of sinusoidal leading edge serrations for the reduction of turbulence–aerofoil interaction noise. *Journal of Fluid Mechanics*, 818:435–464, 2017.

[25] G. Bampanis, M. Roger, D. Ragni, F. Avallone, and C. Teruna. Airfoil-turbulence interaction noise source identification and its reduction by means of leading edge serrations. In *25th AIAA/CEAS Aeroacoustics Conference*, 2019. AIAA Paper 2019-2741.

[26] I. A. Clark, C. A. Daly, W. Devenport, W. N. Alexander, N. Peake, J. W. Jaworski, and S. Glegg. Bio-inspired canopies for the reduction of roughness noise. *Journal of Sound and Vibration*, 385:33–54, 2016.

[27] T. P. Chong and A. Vathylakis. On the aeroacoustic and flow structures developed on a flat plate with a serrated sawtooth trailing edge. *Journal of Sound and Vibration*, 354:65–90, 2015.

[28] T. Dassen, R. Parchen, J. Bruggeman, and F. Hagg. Results of a wind tunnel study on the reduction of airfoil self-noise by the application of serrated blade trailing edges. Technical Report NLR-TP-1996-350, National Aerospace Laboratory, 1996.

[29] M. Gruber. *Airfoil noise reduction by edge treatments*. PhD thesis, University of Southampton, 2012.

[30] C. A. León, R. Merino-Martínez, D. Ragni, F. Avallone, F. Scarano, S. Pröbsting,

M. Snellen, D. G. Simons, and J. Madsen. Effect of trailing edge serration-flow misalignment on airfoil noise emissions. *Journal of Sound and Vibration*, 405:19–33, 2017.

[31] D. J. Moreau and C. J. Doolan. Noise-reduction mechanism of a flat-plate serrated trailing edge. *AIAA Journal*, 51(10):2513–2522, 2013.

[32] A. Finez, M. Jacob, E. Jondeau, and M. Roger. Broadband noise reduction with trailing edge brushes. In *16th AIAA/CEAS Aeroacoustics Conference*, 2010. AIAA Paper 2010-3980.

[33] M. Herr. Design criteria for low-noise trailing-edges. In *13th AIAA/CEAS Aeroacoustics Conference*, 2007. AIAA Paper 2007-3470.

[34] I. A. Clark, W. N. Alexander, W. Devenport, S. Glegg, J. W. Jaworski, C. Daly, and N. Peake. Bioinspired trailing-edge noise control. *AIAA Journal*, 55(3):740–754, 2017.

[35] R. A. Kroeger, H. D. Grushka, and T. C. Helvey. Low speed aerodynamics for ultra-quiet flight. Technical report, Tennessee Univ Space Inst Tullahoma, 1972.

[36] W. Neuhaus, H. Bretting, and B. Schweizer. Morphologische und funktionelle Untersuchungen über den "lautlosen" Flug der Eulen (*Strix aluco*) im Vergleich zum Flug der Enten (*Anas platyrhynchos*). *Biologisches Zentralblatt*, 92:495–512, 1973.

[37] O. Lilienthal. *Der Vogelflug als Grundlage der Fliegekunst.* Walter de Gruyter GmbH & Co KG, 2019.

[38] A. R. Ennos, J. R. E. Hickson, and A. Roberts. Functional morphology of the vanes of the flight feathers of the pigeon *Columba livia*. *Journal of Experimental Biology*, 198 (5):1219–1228, 1995.

[39] T. Bachmann, S. Klän, W. Baumgartner, M. Klaas, W. Schröder, and H. Wagner. Morphometric characterisation of wing feathers of the barn owl *Tyto alba pratincola* and the pigeon *Columba livia*. *Frontiers in Zoology*, 4(1):1–15, 2007.

[40] T. F. Geyer, T. Windisch, C. Fritzsche, and E. Sarradj. Dataset on permeability of wings from owls and non-silently flying birds. *Data in Brief*, 52:109825, 2023.

[41] R. E. Hayden. Exploratory investigation of aeroacoustic optimization of the variable impedance edge concept applied to upper surface blown configurations. Technical Report CR-145072, NASA, 1976.

[42] T. F. Geyer, E. Sarradj, and C. Fritzsche. Measurement of the noise generation at the trailing edge of porous airfoils. *Experiments in Fluids*, 48(2):291–308, 2010.

[43] T. F. Geyer, E. Sarradj, J. Giesler, and M. Hobracht. Experimental assessment of the noise generated at the leading edge of porous airfoils using microphone array techniques. In *17th AIAA/CEAS Aeroacoustics Conference (32nd AIAA Aeroacoustics Conference)*, 2011. AIAA Paper 2011-2713.

[44] C. Jiang. *Noise generation by airfoils and rotors with porous and serrated trailing edges.* PhD thesis, University of New South Wales, 2020.

[45] M. S. Howe. On the added mass of a perforated shell, with application to the generation of aerodynamic sound by a perforated trailing edge. *Proceedings of the Royal Society of London A*, 365(1721):209–233, 1979.

[46] M. R. Khorrami and M. M. Choudhari. Application of passive porous treatment to slat trailing edge noise. Technical Report NASA/TM-2003-2 1241, NASA, 2003.

[47] R. Hajian and J. W. Jaworski. The steady aerodynamics of aerofoils with porosity gradients. *Proceedings of the Royal Society A*, 473(2205), 2017. 20170266.

[48] P. J. Baddoo, R. Hajian, and J. W. Jaworski. Unsteady aerodynamics of porous aerofoils. *Journal of Fluid Mechanics*, 913, 2021. A16.

[49] L. J. Ayton, M. J. Colbrook, T. F. Geyer, C. Paruchuri, and E. Sarradj. Reducing aerofoil–turbulence interaction noise through chordwise-varying porosity. *Journal of Fluid Mechanics*, 906, 2021.

[50] S. A. S. Ali, M. Azarpeyvand, and C. R. I. Da Silva. Trailing-edge flow and noise control using porous treatments. *Journal of Fluid Mechanics*, 850:83–119, 2018.

[51] C. Teruna, F. Manegar, F. Avallone, D. Ragni, D. Casalino, and T. Carolus. Noise reduction mechanisms of an open-cell metal-foam trailing edge. *Journal of Fluid Mechanics*, 898, 2020. A18.

[52] C. Teruna, F. Avallone, D. Ragni, and D. Casalino. On the noise reduction of a porous trailing edge applied to an airfoil at lifting condition. *Physics of Fluids*, 33(5), 2021.

[53] J. Y. Chung and D. A Blaser. Transfer function method of measuring in-duct acoustic properties. I. theory. *Journal of the Acoustical Society of America*, 68(3):907–913, 1980.

[54] J. Y. Chung and D. A. Blaser. Transfer function method of measuring in-duct acoustic properties. II. experiment. *Journal of the Acoustical Society of America*, 68(3):914–921, 1980.

[55] S. Tamaro, R. Zamponi, D. Ragni, C. Teruna, and C. Schram. Experimental investigation of turbulent coherent structures interacting with a porous airfoil. *Experiments in Fluids*, 62:1–18, 2021.

[56] E. J. G. Arcondoulis and Y. Liu. The effect of porosity on the porous coated cylinder diameter. In *Proceedings of ACOUSTICS*, volume 7, 2018.

[57] E. J. G. Arcondoulis, Y. Liu, Z. Li, Y. Yang, and Y. Wang. Structured porous material design for passive flow and noise control of cylinders in uniform flow. *Materials*, 12 (18):2905, 2019.

[58] C. Jiang, D. J. Moreau, C. de Silva, and C. J. Doolan. Noise generation mechanisms of a micro-tube porous trailing edge. *Journal of Sound and Vibration*, 571, 2024. 118085.

[59] S. A. S. Ali, S. Alihan, M. Azarpeyvand, and C. R. I. da Silva. Trailing edge bluntness noise reduction using porous treatments. *Journal of Sound and Vibration*, 474, 2020. 115257.

[60] H. Liu, Z. Hu, N. Chen, Y. Liu, and H. Fan. Structured porous blunt trailing edge with uniform and non-uniform parameters for vortex shedding noise reduction. *Applied Acoustics*, 206:109302, 2023.

[61] Elias J. G. Arcondoulis, Daniele Ragni, Daniele Fiscaletti, Roberto Merino-Martinez, and Yu Liu. Acoustic response of structured and randomized porous blunt trailing edges subject to turbulent boundary layers. *The Journal of the Acoustical Society of America*, 156(2):1029–1040, 08 2024.

[62] Y. Bae, Y. E. Jeong, and Y. Moon. Effect of porous surface on the flat plate self-noise. In *15th AIAA/CEAS Aeroacoustics Conference (30th AIAA Aeroacoustics Conference)*, 2009. AIAA Paper 2009-3311.

[63] M. J. Swann, A. S. Nickels, M. H. Krane, and J. R. Harris. Aeroacoustic source separation of non-stationary signals in time domain with RPCA. In *30th AIAA/CEAS Aeroacoustics Conference (2024)*, 2024. AIAA Paper 2024-3138.

[64] Z. Yoas. Passive trailing edge noise attenuation with porosity, inspired by owl plumage. Master's thesis, The Pennsylvania State University, 2021.

[65] M. J. Swann, Z. W. Yoas, P. Trzcinski, A. Nickels, and M. H. Krane. Array processing of porous trailing edge aeroacoustics. *Bulletin of the American Physical Society*, 2022. U11.00005.

[66] C. J. Doolan, D. J. Moreau, and A. O. Wills. *Flinovia–Flow Induced Noise and Vibration Issues and Aspects-IV*. Springer Nature, 2024.

[67] L. J. Ayton, O. Karapiperis, M. Awasthi, D. J. Moreau, and C. J. Doolan. Spanwise varying porosity for the enhancement of leading-edge noise reduction. In *AIAA Aviation 2021 Forum*, 2021. AIAA Paper 2021-2191.

[68] L. J. Ayton and J. W. Kim. An analytic solution for the noise generated by gust–aerofoil interaction for plates with serrated leading edges. *Journal of Fluid Mechanics*, 853:515–536, 2018.

[69] L. J. Ayton, M. Szoke, C. Paruchuri, W. J. Devenport, and W. N. Alexander. Trailing-edge serrations: improving theoretical noise reduction models. In *AIAA AVIATION 2021 Forum*, 2021. AIAA Paper 2021-2111.

[70] E. Sarradj, C. Fritzsche, T. F. Geyer, and J. Giesler. Acoustic and aerodynamic design and characterization of a small-scale aeroacoustic wind tunnel. *Applied Acoustics*, 70 (8):1073–1080, 2009.

[71] T. F. Geyer and L. Enghardt. Noise generation by two staggered circular cylinders of equal diameter in cross-flow. In *28th AIAA/CEAS Aeroacoustics Conference*, 2022. AIAA Paper 2022-3093.

[72] E. Sarradj and G. Herold. A Python framework for microphone array data processing. *Applied Acoustics*, 116:50–58, 2017.

[73] P. Welch. The use of fast Fourier transform for the estimation of power spectra: a method based on time averaging over short, modified periodograms. *IEEE Transactions on Audio and Electroacoustics*, 15(2):70–73, 1967.

[74] F. M. White and J. Majdalani. *Viscous Fluid Flow*, volume 3. McGraw-Hill New York, 2006.

[75] P. Sijtsma. CLEAN based on spatial source coherence. *International Journal of Aeroacoustics*, 6(4):357–374, 2007.

[76] J. S. Bendat and G. Piersol. *Random Data: Analysis and Measurement Procedures.* John Wiley & Sons, 1986.

[77] T. F. Geyer. *Trailing edge noise generation of porous airfoils.* PhD thesis, BTU Cottbus-Senftenberg, 2011.

[78] A. O. Wills, M. Awasthi, C. de Silva, D. J. Moreau, and C. J. Doolan. Design and characterisation of a 3-D microphone array for windtunnel measurements. *The Journal of the Acoustical Society of America*, 154(4_supplement), 2023.

[79] P. Chiariotti, M. Martarelli, and P. Castellini. Acoustic beamforming for noise source localization–reviews, methodology and applications. *Mechanical Systems and Signal Processing*, 120:422–448, 2019.

[80] R. P. Dougherty. Functional beamforming. In *5th Berlin Beamforming Conference*, pages 19–20. Society for the Advancement of Applied Computer Science, 2014.

[81] R. Merino-Martinez, M. Snellen, and D. G. Simons. Functional beamforming applied to full scale landing aircraft. In *6th Berlin Beamforming Conference, February*, 2016. BeBeC-2016-D12.

[82] R. Merino-Martínez, M. Snellen, and D. G. Simons. Functional beamforming applied to imaging of flyover noise on landing aircraft. *Journal of Aircraft*, 53(6):1830–1843, 2016.

[83] E. Sarradj, C. Schulze, and A. Zeibig. Identification of noise source mechanisms using orthogonal beamforming. *Noise and vibration: emerging methods*, 2005.

[84] E. Sarradj. A fast signal subspace approach for the determination of absolute levels from phased microphone array measurements. *Journal of Sound and Vibration*, 329 (9):1553–1569, 2010.

[85] T. F. Brooks and W. M. Humphreys. A deconvolution approach for the mapping of acoustic sources (DAMAS) determined from phased microphone arrays. *Journal of sound and vibration*, 294(4-5):856–879, 2006.

[86] G. Herold and E. Sarradj. Performance analysis of microphone array methods. *Journal of Sound and Vibration*, 401:152–168, 2017.

[87] S. Glegg and W. Devenport. *Aeroacoustics of low Mach number flows: fundamentals, analysis, and measurement.* Academic Press, 2023.

[88] V. B. Ananthan, R. A. D. Akkermans, T. Hu, P. Q. Liu, and N. Rathje. Trailing-edge

noise reduction potential of a locally applied shallow dimpled surface. *Journal of Sound and Vibration*, 525, 2022. 116745.

[89] S. McTavish, D. Feszty, and F. Nitzsche. Evaluating Reynolds number effects in small-scale wind turbine experiments. *Journal of Wind Engineering and Industrial Aerodynamics*, 120:81–90, 2013.

[90] S. Lee and S. Lee. Numerical and experimental study of aerodynamic noise by a small wind turbine. *Renewable Energy*, 65:108–112, 2014.

[91] J. R. Kershner, J. W. Jaworski, and T. F. Geyer. Experimental study of trailing-edge bluntness noise reduction by porous plates. In *AIAA AVIATION 2023 Forum*, 2023. AIAA Paper 2023-4284.

[92] J. R. Kershner, J. W. Jaworski, and T. F. Geyer. Experimental study of trailing-edge bluntness noise reduction by porous plates. *AIAA Journal*, 0(0):1–12, 2024.

[93] S. Lee, L. J. Ayton, F. Bertagnolio, S. Moreau, T. P. Chong, and P. Joseph. Turbulent boundary layer trailing-edge noise: Theory, computation, experiment, and application. *Progress in Aerospace Sciences*, 126:100737, 2021.

[94] Z. W. Yoas, M. Swann, M. H. Krane, H. Chen, and J. W. Jaworski. Acoustic emission of a vortex ring near a porous edge. Part 2: experimental. In preparation, 2024.

[95] E. M. Gennaro, A. K. Colaciti, and M. A. F. Medeiros. On the controversy regarding the effect of flow shear on the strouhal number of cylinder vortex shedding. *Aerospace Science and Technology*, 29(1):313–320, 2013.

[96] Z. Feng and Q. Ye. Turbulent boundary layer over porous media with wall-normal permeability. *Physics of Fluids*, 35(9), 2023. 095111.

Appendix A

Additional acoustic wind tunnel measurement details

A.1 Microphone array coordinates

A.1.1 BTU aeroacoustic wind tunnel

The coordinates for the microphone positions from Wind Tunnel Campaign 1 conducted in the BTU aeroacoustic wind tunnel are presented in table A.1. Microphones 1 to 56 are located on the planar array, and microphones 57 to 67 are located on the arc array.

A.1.2 UNSW Anechoic Wind Tunnel

The coordinates for the microphone positions from Wind Tunnel Campaign 2 conducted in the UNSW Anechoic Wind Tunnel are presented in table A.2. All microphones are located in the plane $z = 0$.

Table A.1: BTU microphone array coordinates

Number	x, m	y, m	z, m	Number	x, m	y, m	z, m
1	-0.146	0.634	0	35	0.641	-0.108	0
2	-0.067	0.237	0	36	0.244	-0.029	0
3	-0.377	0.530	0	37	0.030	-0.463	0
4	-0.152	0.193	0	38	0.139	-0.242	0
5	-0.551	0.345	0	39	0.029	-0.088	0
6	-0.215	0.120	0	40	0.349	-0.307	0
7	-0.641	0.108	0	41	0.269	-0.073	0
8	-0.244	0.029	0	42	0.083	-0.042	0
9	-0.030	0.463	0	43	0.634	0.146	0
10	-0.139	0.242	0	44	0.237	0.067	0
11	-0.029	0.088	0	45	0.530	0.377	0
12	-0.349	0.307	0	46	0.193	0.152	0
13	-0.269	0.073	0	47	0.345	0.551	0
14	-0.083	0.042	0	48	0.120	0.215	0
15	-0.634	-0.146	0	49	0.108	0.641	0
16	-0.237	-0.067	0	50	0.029	0.244	0
17	-0.530	-0.377	0	51	0.463	0.030	0
18	-0.193	-0.152	0	52	0.242	0.139	0
19	-0.345	-0.551	0	53	0.088	0.029	0
20	-0.120	-0.215	0	54	0.307	0.349	0
21	-0.108	-0.641	0	55	0.073	0.269	0
22	-0.029	-0.244	0	56	0.042	0.083	0
23	-0.463	-0.030	0	57	0.740	0	1.454
24	-0.242	-0.139	0	58	0.666	0	1.503
25	-0.088	-0.029	0	59	0.581	0	1.543
26	-0.307	-0.349	0	60	0.489	0	1.570
27	-0.073	-0.269	0	61	0.367	0	1.582
28	-0.042	-0.083	0	62	0.277	0	1.575
29	0.146	-0.634	0	63	0.168	0	1.549
30	0.067	-0.237	0	64	0.062	0	1.500
31	0.377	-0.530	0	65	-0.036	0	1.429
32	0.152	-0.193	0	66	-0.120	0	1.338
33	0.551	-0.345	0	67	-0.183	0	1.233
34	0.215	-0.120	0				

Table A.2: UNSW microphone array coordinates

Number	x, m	y, m	Number	x, m	y, m
1	0.080	0.000	34	-0.137	0.020
2	0.137	-0.020	35	-0.231	0.067
3	0.231	-0.067	36	-0.310	-0.005
4	0.310	0.005	37	-0.359	-0.077
5	0.359	0.077	38	-0.389	-0.146
6	0.389	0.146	39	-0.409	-0.211
7	0.409	0.211	40	-0.420	-0.272
8	0.420	0.272	41	-0.057	-0.057
9	0.057	0.057	42	-0.111	-0.083
10	0.111	0.083	43	-0.211	-0.116
11	0.211	0.116	44	-0.216	-0.223
12	0.216	0.223	45	-0.199	-0.308
13	0.199	0.308	46	-0.172	-0.379
14	0.172	0.379	47	-0.140	-0.438
15	0.140	0.438	48	-0.104	-0.489
16	0.104	0.489	49	0.000	-0.080
17	0.000	0.080	50	-0.020	-0.137
18	0.020	0.137	51	-0.067	-0.231
19	0.067	0.231	52	0.005	-0.310
20	-0.005	0.310	53	0.077	-0.359
21	-0.077	0.359	54	0.146	-0.389
22	-0.146	0.389	55	0.211	-0.409
23	-0.211	0.409	56	0.272	-0.420
24	-0.272	0.420	57	0.057	-0.057
25	-0.057	0.057	58	0.083	-0.111
26	-0.083	0.111	59	0.116	-0.211
27	-0.116	0.211	60	0.223	-0.216
28	-0.223	0.216	61	0.308	-0.199
29	-0.308	0.199	62	0.379	-0.172
30	-0.379	0.172	63	0.438	-0.140
31	-0.438	0.140	64	0.489	-0.104
32	-0.489	0.104	65	0.000	0.000
33	-0.080	0.000			

A.2 Effect of reflections from the planar array in WTC-1

To test whether or not the planar array in WTC-1 caused significant reflections, tests were conducted with and without the array covered up by a sound absorptive blanket. Figure A.1 displays sound pressure levels as recorded by a microphone on the arc-array located 90° from the TE of the test plate. The sound pressure levels show no significant difference with the array left covered or uncovered by a blanket.

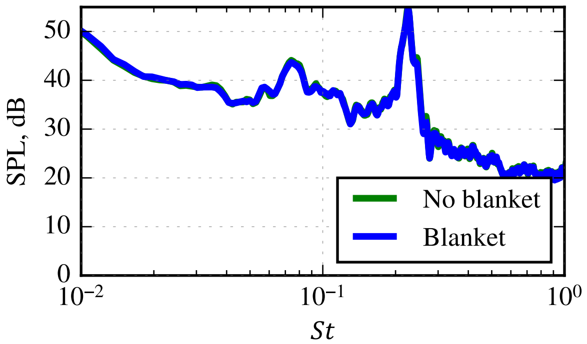

Figure A.1: SPL of the nonporous plate at $U = 30$ m/s as recorded by a single mic on the arc-array with the planar array covered and uncovered by a sound absorptive blanket.

A.3 Point spread function of the WTC-1 array

The directivity pattern generated by the point spread function of the WTC-1 array is displayed in figure A.2. This figure displays the main lobe at the center ($x = 0,\ y = 0$), and the number of lobes increase with an increase in frequency.

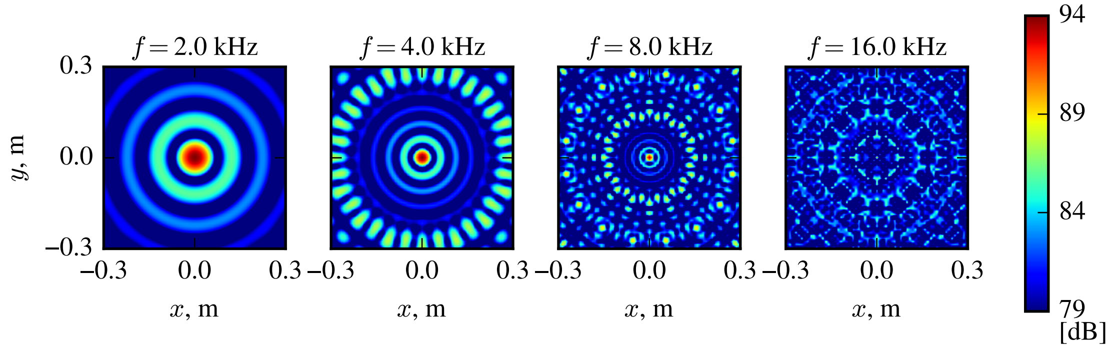

Figure A.2: Directivity pattern (or the beam pattern) of the microphone array at selected frequencies.

A.4 Location of low-frequency sound sources by DAMAS beamforming at high flow speeds in WTC-1

Figure A.3 presents soundmaps at $f = 500$ Hz for the nonporous plates at three flow speeds. The dynamic range for all of the plots is 5 dB. This figure is included to highlight the change in location of low frequency noise as calculated by DAMAS when increasing flow speed. At the highest flow speed, the maximum noise level is located outside of the integration area at the top right edge of the plot, and the cause for this incorrect location of the sound source is unknown. As a result, the spectra integrated within the sectors defined in figure 2.13 are much lower than anticipated for the nonporous plate at this high flow speed case.

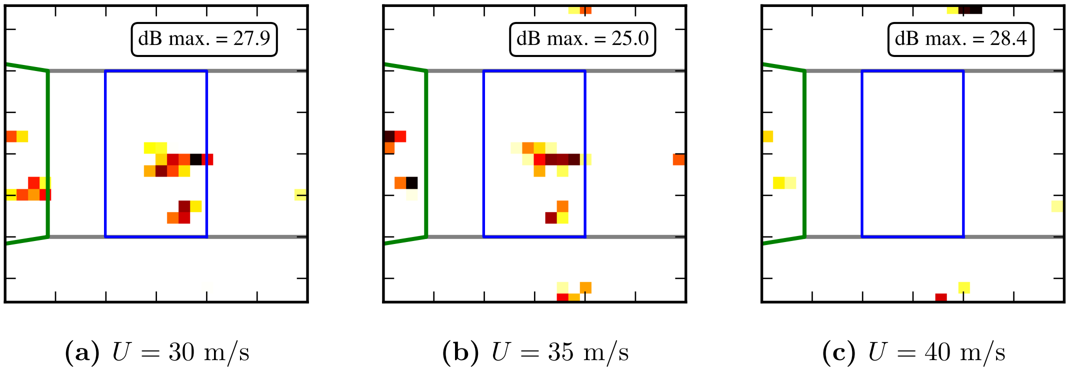

(a) $U = 30$ m/s **(b)** $U = 35$ m/s **(c)** $U = 40$ m/s

Figure A.3: Soundmaps at three different flow speeds created using DAMAS with a third-octave band centered on $f = 500$ Hz.

Biography

John R. Kershner was born on October 12, 1997 in Reading, Pennsylvania. In 2020, John received his Bachelor of Science in Mechanical Engineering from York College of Pennsylvania. In the summer of 2020, John began his Ph.D. program at Lehigh University within the Department of Mechanical Engineering and Mechanics. During his time at Lehigh, John completed an NSF INTERN internship at the Applied Research Laboratory at Penn State University and later received a Fulbright Scholarship to continue his experimental aeroacoustics research at the Brandenburg University of Technology in Cottbus, Germany. During this time, he also traveled to the University of New South Wales to participate in experiments with the Flow Noise Group. He has presented research at conferences in the U.S., Germany, Australia, and Italy. Outside of the lab, John enjoys traveling, skiing, cooking, and spending time with his pets.